



THÈSE de DOCTORAT DE L'UNIVERSITÉ DE LYON

Opérée au sein de

L'Institut National des Sciences Appliquées de Lyon

ÉCOLE DOCTORALE N° ED 162

Mécanique - Energétique - Génie Civil - Acoustique

Spécialité : Acoustique

Soutenue publiquement le 05 Avril 2017, par

Mohammad Azizian Kalkhoran

---

Design and development of a universal  
handheld probe for optoacoustic-ultrasonic  
3D imaging

---

Devant le jury composé de :

**Georg Schmitz**

**Anabela Da Silva**

**Sylvain Gigan**

**Alessandro Stuart Savoia**

**François Varray**

**Didier Vray**

Professeur, Ruhr-Universität Bochum

Chargée de Recherche CNRS, Institut FRESNEL

Professeur, Université Pierre et Marie Curie, Paris

Maître de Conférences, Università degli Studi Roma Tre

Maître de Conférences, Université Claude Bernard Lyon 1

Professeur, INSA de Lyon

Rapporteur

Rapporteur

Examineur

Examineur

Examineur

Directeur de thèse

**Département FEDORA – INSA Lyon - Ecoles Doctorales – Quinquennal 2016-2020**

<b>SIGLE</b>	<b>ECOLE DOCTORALE</b>	<b>NOM ET COORDONNEES DU RESPONSABLE</b>
<b>CHIMIE</b>	<p><b>CHIMIE DE LYON</b>  <a href="http://www.edchimie-lyon.fr">http://www.edchimie-lyon.fr</a></p> <p>Sec : Renée EL MELHEM            Bat Blaise Pascal 3<sup>e</sup> etage  <a href="mailto:secretariat@edchimie-lyon.fr">secretariat@edchimie-lyon.fr</a>            Insa : R. GOURDON</p>	<p><b>M. Stéphane DANIELE</b>            Institut de Recherches sur la Catalyse et l'Environnement de Lyon            IRCELYON-UMR 5256            Equipe CDFA            2 avenue Albert Einstein            69626 Villeurbanne cedex  <a href="mailto:directeur@edchimie-lyon.fr">directeur@edchimie-lyon.fr</a></p>
<b>E.E.A.</b>	<p><b>ELECTRONIQUE, ELECTROTECHNIQUE, AUTOMATIQUE</b>  <a href="http://edeea.ec-lyon.fr">http://edeea.ec-lyon.fr</a></p> <p>Sec : M.C. HAVGOUDOUKIAN  <a href="mailto:Ecole-Doctorale.eea@ec-lyon.fr">Ecole-Doctorale.eea@ec-lyon.fr</a></p>	<p><b>M. Gérard SCORLETTI</b>            Ecole Centrale de Lyon            36 avenue Guy de Collongue            69134 ECULLY            Tél : 04.72.18 60.97 Fax : 04 78 43 37 17  <a href="mailto:Gerard.scorletti@ec-lyon.fr">Gerard.scorletti@ec-lyon.fr</a></p>
<b>E2M2</b>	<p><b>EVOLUTION, ECOSYSTEME, MICROBIOLOGIE, MODELISATION</b>  <a href="http://e2m2.universite-lyon.fr">http://e2m2.universite-lyon.fr</a></p> <p>Sec : Safia AIT CHALAL            Bat Darwin - UCB Lyon 1            04.72.43.28.91            Insa : H. CHARLES  <a href="mailto:Safia.ait-chalal@univ-lyon1.fr">Safia.ait-chalal@univ-lyon1.fr</a></p>	<p><b>Mme Gudrun BORNETTE</b>            CNRS UMR 5023 LEHNA            Université Claude Bernard Lyon 1            Bât Forel            43 bd du 11 novembre 1918            69622 VILLEURBANNE Cédex            Tél : 06.07.53.89.13  <a href="mailto:e2m2@univ-lyon1.fr">e2m2@univ-lyon1.fr</a></p>
<b>EDISS</b>	<p><b>INTERDISCIPLINAIRE SCIENCES-SANTE</b>  <a href="http://www.ediss-lyon.fr">http://www.ediss-lyon.fr</a></p> <p>Sec : Safia AIT CHALAL            Hôpital Louis Pradel - Bron            04 72 68 49 09            Insa : M. LAGARDE  <a href="mailto:Safia.ait-chalal@univ-lyon1.fr">Safia.ait-chalal@univ-lyon1.fr</a></p>	<p><b>Mme Emmanuelle CANET-SOULAS</b>            INSERM U1060, CarMeN lab, Univ. Lyon 1            Bâtiment IMBL            11 avenue Jean Capelle INSA de Lyon            696621 Villeurbanne            Tél : 04.72.68.49.09 Fax :04 72 68 49 16  <a href="mailto:Emmanuelle.canet@univ-lyon1.fr">Emmanuelle.canet@univ-lyon1.fr</a></p>
<b>INFOMATHS</b>	<p><b>INFORMATIQUE ET MATHEMATIQUES</b>  <a href="http://infomaths.univ-lyon1.fr">http://infomaths.univ-lyon1.fr</a></p> <p>Sec :Renée EL MELHEM            Bat Blaise Pascal            3<sup>e</sup> etage  <a href="mailto:infomaths@univ-lyon1.fr">infomaths@univ-lyon1.fr</a></p>	<p><b>Mme Sylvie CALABRETTO</b>            LIRIS – INSA de Lyon            Bat Blaise Pascal            7 avenue Jean Capelle            69622 VILLEURBANNE Cedex            Tél : 04.72. 43. 80. 46 Fax 04 72 43 16 87  <a href="mailto:Sylvie.calabretto@insa-lyon.fr">Sylvie.calabretto@insa-lyon.fr</a></p>
<b>Matériaux</b>	<p><b>MATERIAUX DE LYON</b>  <a href="http://ed34.universite-lyon.fr">http://ed34.universite-lyon.fr</a></p> <p>Sec : M. LABOUNE            PM : 71.70 –Fax : 87.12            Bat. Saint Exupéry  <a href="mailto:Ed.materiaux@insa-lyon.fr">Ed.materiaux@insa-lyon.fr</a></p>	<p><b>M. Jean-Yves BUFFIERE</b>            INSA de Lyon            MATEIS            Bâtiment Saint Exupéry            7 avenue Jean Capelle            69621 VILLEURBANNE Cedex            Tél : 04.72.43 71.70 Fax 04 72 43 85 28  <a href="mailto:Ed.materiaux@insa-lyon.fr">Ed.materiaux@insa-lyon.fr</a></p>
<b>MEGA</b>	<p><b>MECANIQUE, ENERGETIQUE, GENIE CIVIL, ACOUSTIQUE</b>  <a href="http://mega.universite-lyon.fr">http://mega.universite-lyon.fr</a></p> <p>Sec : M. LABOUNE            PM : 71.70 –Fax : 87.12            Bat. Saint Exupéry  <a href="mailto:mega@insa-lyon.fr">mega@insa-lyon.fr</a></p>	<p><b>M. Philippe BOISSE</b>            INSA de Lyon            Laboratoire LAMCOS            Bâtiment Jacquard            25 bis avenue Jean Capelle            69621 VILLEURBANNE Cedex            Tél : 04.72 .43.71.70 Fax : 04 72 43 72 37  <a href="mailto:Philippe.boisse@insa-lyon.fr">Philippe.boisse@insa-lyon.fr</a></p>
<b>ScSo</b>	<p><b>ScSo*</b>  <a href="http://recherche.univ-lyon2.fr/scso/">http://recherche.univ-lyon2.fr/scso/</a></p> <p>Sec : Viviane POLSINELLI            Brigitte DUBOIS            Insa : J.Y. TOUSSAINT  <a href="mailto:viviane.polsinelli@univ-lyon2.fr">viviane.polsinelli@univ-lyon2.fr</a></p>	<p><b>Mme Isabelle VON BUELTZINGLOEWEN</b>            Université Lyon 2            86 rue Pasteur            69365 LYON Cedex 07            Tél : 04.78.77.23.86 Fax : 04.37.28.04.48</p>

\*ScSo : Histoire, Géographie, Aménagement, Urbanisme, Archéologie, Science politique, Sociologie, Anthropologie

*To my mom Shahin Sane; ;  
Harmonic source of life's music,*

*To my dad Mohammadreza Azizian Kalkhoran ;  
Perpetual coherence in the turbid world,*

*To Lin Cheng ;  
Continuous spectra of sun laugh, hope and hymn.*

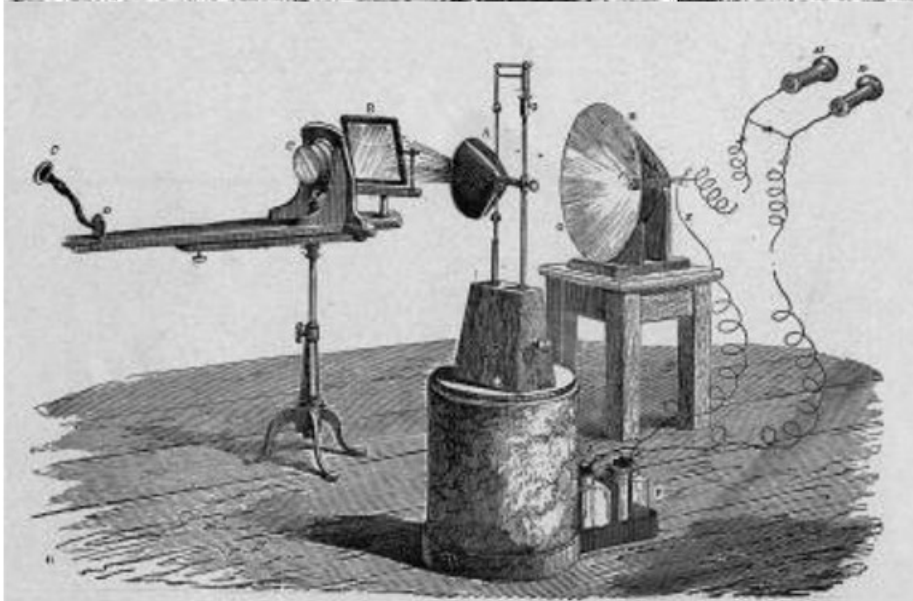




*I have heard articulate speech produced by sunlight, I have heard a ray of the sun laugh and cough and sing!*

...  
*I have been able to hear a shadow, and I have even perceived by ear the passage of a cloud across the sun's disk.*

*Alexander G. Bell*





## Abstract

When the interest is in multiscale and multipurpose imaging, there exists such a will in integrating multi-modalities into a synergistic paradigm in order to leverage the diagnostic values of the interrogating agents. Employing multiple wavelengths radiation, optoacoustic imaging benefits from the optical contrast to specifically resolve molecular structure of tissue in a non-invasive manner. Hybridizing optoacoustic and ultrasound imaging comes with the promises of delivering the complementary morphological, functional and metabolic information of the tissue. This dissertation is mainly devoted to the design and characterization of a hybridized universal handheld probe for optoacoustic ultrasound volumetric imaging and developing adaptive reconstruction algorithms toward the physical requirements of the designed system.

The distinguishing features of this dissertation are the introduction of a new geometry for optoacoustic ultrasonic handheld probe and systematic assessments based on pre and post reconstruction methods. To avoid the biased interpretation, a *de facto* performance assessment being capable of evaluating the potentials of the designed probe in an unbiased manner must be practiced. The aforementioned features establish a framework for characterization of the imaging system performance in an accurate manner. Moreover, it allows further task performance optimization as well.

Correspondingly, two advanced reconstruction algorithms have been elaborated towards the requirement of the designed optoacoustic-ultrasound (OPUS) imaging system in order to maximize its ability to produce images with homogeneous contrast and resolution over the entire volume of interest. This interest is mainly due to the fact that the medical data analysis pipeline is often carried out in challenging conditions, since one has to deal with noise, low contrast, limited projections and undesirable transformations operated by the acquisition system. The presented thesis shows how reconstruction artifacts can be reduced by compensating for the detecting aperture properties and alleviate artifacts due to sparse angular sampling.

In pursuit of transferring this methodology to clinic and validating the theoretical results, a synthetic imaging platform was developed. Using the measurement system, the evolution of a novel sparse annular geometry and its dynamics has been investigated and a proof of concept was demonstrated via experimental measurement with the intention of benchmarking progress.

**Keywords :** optoacoustic imaging, ultrasound imaging, synthetic aperture focusing technique, sparse 2D array, volumetric imaging, bimodality, 3D reconstruction.





## Résumé en français

Lorsqu'on s'intéresse à l'imagerie multi-échelle et multi-fonction, on a souvent envie d'utiliser un système d'imagerie multi-modal et faire en sorte que ce dernier crée un effet synergique permettant d'exploiter les diagnostics fournis par chacune des modalités. Basée sur des rayonnements de longueurs d'onde multiples, l'imagerie optoacoustique utilise le contraste optique pour imager, spécifiquement, la structure moléculaire des tissus d'une manière non-invasive. Ainsi, l'hybridation de l'imagerie optoacoustique et de l'imagerie ultrasonore pourrait fournir en plus, des informations morphologiques, fonctionnelles et métaboliques des tissus. La présente thèse est principalement consacrée à la conception et à la caractérisation d'une sonde universelle pour l'imagerie volumétrique ultrasons-optoacoustique et le développement d'un algorithme de reconstruction adapté aux exigences physiques pour la conception du système.

Les traits distinctifs de cette thèse sont l'introduction d'une nouvelle géométrie pour les sondes manuelles ultrasons-optoacoustique et des évaluations systématiques basées sur des méthodes de pré-reconstruction et post-reconstruction. Pour éviter l'interprétation biaisée, une évaluation capable d'évaluer le potentiel de la sonde doit être faite. Les caractéristiques mentionnées établissent un cadre pour l'évaluation des performances du système d'imagerie d'une manière précise. En outre, elle permet d'optimiser les performances suivant l'objectif fixé.

Ainsi, deux algorithmes de reconstruction ont été élaborés pour la conception du système OPUS (optoacoustique ultrasons) capables de produire des images avec un contraste et une résolution homogènes sur tout le volume d'intérêt. L'intérêt d'avoir de tels algorithmes est principalement dû au fait que l'analyse des données médicales est souvent faite dans des conditions difficiles, car on est face au bruit, au faible contraste, aux projections limités et à des transformations indésirables opérées par les systèmes d'acquisition. Cette thèse montre, aussi, comment les artefacts de reconstruction peuvent être réduits en compensant les propriétés d'ouverture et en atténuant les artefacts dus à l'échantillonnage angulaire parcimonieux.

Afin de transférer cette méthodologie à la clinique et de valider les résultats théoriques, une plate-forme d'imagerie expérimentale a été développée. En utilisant le système de mesure développé, l'évolution d'une nouvelle géométrie annulaire parcimonieuse et sa dynamique ont été étudiées et une preuve de concept a été démontrée à travers des mesures expérimentales dans le but d'évaluer les progrès réalisés.

**Mots clés :** Imagerie optoacoustique, échographie, capteurs 2D parcimonieux, synthèse d'ouverture focalisée, imagerie volumétrique, bimodalité, reconstruction 3D.



---

## Table des matières

---

<b>1</b>	<b>Introduction</b>	<b>1</b>
1.1	Incentive of the work . . . . .	1
1.2	Current OPUS systems, applications and limitations . . . . .	3
1.3	Questions to be addressed in this dissertation (contributions) . . . . .	4
1.4	Overview of the dissertation . . . . .	4
<b>2</b>	<b>The Basic Principles of OPUS</b>	<b>7</b>
2.1	Introduction . . . . .	7
2.2	Basic of Ultrasound imaging . . . . .	9
2.2.1	Ultrasonic wave interaction with the tissue . . . . .	9
	Attenuation . . . . .	9
	Speckle . . . . .	11
2.2.2	Ultrasonic transducers . . . . .	11
	Piezoelectric transducer . . . . .	11
	Micromachined Ultrasonic Transducers . . . . .	12
	CMUT . . . . .	13
	PMUT . . . . .	13
	Laser ultrasound and optical detectors . . . . .	14
2.2.3	Array imaging . . . . .	15
	Image formation . . . . .	16
2.3	Basic of Optoacoustic imaging . . . . .	17
2.3.1	Light propagation in tissue . . . . .	17
2.3.2	Photon to phonon translation, origin of optical contrast . . . . .	19
	Time domain . . . . .	19
	Boundary build-up effect . . . . .	20
2.3.3	Optoacoustic image formation . . . . .	21
2.4	Conclusion . . . . .	23
<b>3</b>	<b>A Discrete Imaging Model For OPUS</b>	<b>25</b>
3.1	Introduction . . . . .	25
3.2	Green's functions and acoustic wave equation . . . . .	26
3.3	Numerical solutions for transducers impulse response . . . . .	28
3.3.1	Numerical solution for subdiced planar aperture . . . . .	28
3.4	Discrete-domain model based on Impulse Response . . . . .	31
3.5	IR model matrix otherwise interpretation . . . . .	33
3.5.1	Transient field . . . . .	33
3.5.2	Weighting factor . . . . .	34
3.5.3	The aperture limited view . . . . .	35
3.6	Conclusion . . . . .	37

<b>4</b>	<b>Design and Characterization of OPUS</b>	<b>39</b>
4.1	Introduction . . . . .	39
4.2	Pre-reconstruction generic assessment . . . . .	42
4.2.1	Voxel Crosstalk matrix . . . . .	42
	Signal fidelity metric . . . . .	43
4.2.2	Eigenanalysis . . . . .	44
	Singular value decomposition . . . . .	44
	Rank of matrix . . . . .	45
	Eigenspectrum . . . . .	46
	Singular vector analysis . . . . .	46
4.3	Array design . . . . .	48
4.3.1	Frequency response . . . . .	49
4.3.2	Light delivery system . . . . .	49
4.3.3	Design strategy . . . . .	51
	Inter-element spacing . . . . .	51
	The aspect ratio . . . . .	56
	Geometrical distribution . . . . .	61
4.4	Conclusion . . . . .	67
4.4.1	Perspective . . . . .	67
<b>5</b>	<b>Post processing evaluation</b>	<b>69</b>
5.1	Introduction . . . . .	69
5.2	Deconvolution of acousto-electric impulse response . . . . .	70
	Simulation test data . . . . .	72
5.3	Method based on the Delay and Sum Back Projection . . . . .	74
5.3.1	Weighted Synthetic Aperture . . . . .	77
	Coherence factors . . . . .	77
	Spatial impulse response . . . . .	79
5.3.2	Comparison of weighting factors and their effect in DSBP . . . . .	79
5.3.3	Virtual element . . . . .	82
5.3.4	Matrix representation of DSBP . . . . .	84
5.3.5	Matched filter interpretation . . . . .	84
5.4	Focusing as an inverse problem . . . . .	85
5.5	Post-reconstruction evaluation . . . . .	88
5.5.1	Optoacoustic . . . . .	88
5.5.2	Ultrasound . . . . .	90
5.6	Conclusion . . . . .	93
<b>6</b>	<b>Experimental validation of OPUS</b>	<b>95</b>
6.1	Introduction . . . . .	95
6.2	Experimental setup . . . . .	96
6.2.1	Illumination system . . . . .	96
6.2.2	Acquisition system . . . . .	97
6.2.3	Scanning system . . . . .	97
6.3	Measurement . . . . .	98
6.3.1	Transducer characterization . . . . .	98
6.3.2	Acquisition . . . . .	99
6.3.3	Phantom . . . . .	99
6.4	Results . . . . .	100
6.5	Conclusion . . . . .	101
<b>7</b>	<b>Conclusion and Perspective</b>	<b>103</b>
7.1	Summary and concluding remarks . . . . .	104
7.2	Future work . . . . .	106

# CHAPITRE 1

---

## Introduction

---

After a certain high level of technical skill is achieved, science and art tend to coalesce in aesthetics, plasticity and form. The greatest scientists are always artist as well.

---

Albert Einstein

### 1.1 Incentive of the work

**I**N the past decades, the continuous development in medical imaging systems paved the way for variety of applications and opportunities in clinical and preclinical research and studies. The significant diagnostic value and the level of confidence in the efficacy and safety of some of these agents make them a reliable tool for routine clinical trials. Others, while still advancing, have been shown to hold great promises of transition from bench to bed side and going beyond principle to practice. In fact, when the interest is in multiscale and multipurpose imaging, there exists such a will in integrating multi-modalities into a synergistic paradigm in order to leverage the diagnostic values of the interrogating agents. Additionally, hybridizing prompts the clinical translation of the new approach and further, opens a new door for the currently established device and augments their functionality. For instance, if the clinically routine system is targeting only the structural deformation, integration with an imaging system that aims at the functional information may assist the early stage diagnosis, to track the disease development progress and improve the treatment monitoring.

Throughout the years, ultrasound has shown great potentials and impacts as a diagnostic agent. It's safety records, portability, rich and non-ionizing interaction with the anatomy of the tissue and capability for real time display of the tissue dynamics in 2D and 3D, makes ultrasound a viable tool in diagnostic imaging. The recent endeavors to improve US 3D dynamic acquisition is particularly important where the temporal information of the entire volume is critical for accurate measurement in multiple planes, as is the case for neurosonography and echocardiography. The aforementioned competence and some of ultrasonic wave characteristics including the acoustic speed and attenuation are still being investigated for the tissue characterization. However, ultrasound has limited capacity in providing sensitivity to molecular and functional contrast and chemical specificity, as often the mechanical contrast in neighboring tissues are not high enough for pathological purposes. Therefore, despite promises [2], the accurately delineation of the tissue integrity using ultrasound with no additional contrast enhancing is left to be exploited.

It is a well known fact that the electromagnetic radiation interaction with biological tissue is highly selective with respect to the electronic structure and chemical bonding of tissue itself.

This is specially true for the visible and infrared spectrum of the light, thereby making light an ideal technological ally for further physiological interrogation of the tissue. Yet, high resolution pure optical imaging deeper than one transport mean free path remains challenging. The so called optoacoustic imaging technique has been practiced over the last few years with promises in extending the depth of optical imaging by pairing the ultrasonic wave properties with the merits of optical imaging. In this technique, the optical absorption properties of the tissue are encoded into the broadband ultrasonic pulse which is a function of shape, photoacoustic efficiency and optical absorption coefficient of the chromophore and the fluence of the light. Detecting these induced acoustic waves on the surface of the medium can reveal information associated with the structure of the absorbers, and in multispectral systems, physiological properties such as angiogenesis and blood oxygenation that helps in early stage diagnosis as major indication for cancer.

Since the detection is taking place with the same ultrasonic sensors, and due to the conceptual similarities between optoacoustic (OA) and ultrasound (US), hybridizing these imaging modalities into one compound measurement system is intrinsic and only requires the integration of the light delivery system to the ultrasonic probe. Such a combination allows to realize the potential benefits of optoacoustic-ultrasound (OPUS) as a promising multimodality approach in obtaining the highly complementary diagnostic information. This would thereby enables the concurrent measurement, co-registration and assimilation of distinct features of the investigating tissue. Consequently the limitation of individual modality can be surmounted for example via mapping the volumetric functional and anatomical information of the targeted tissue.

Yet, until the beginning of this work at 2014, OPUS integration has not been fully evolved to address the physical requirements of both imaging systems. The existing implementations presented in the literature are either based on ultrasound probe or systematically optimized for optoacoustic acquisition. The detection array, even though take place by the ultrasonic transducers, demands different set of characterizations for either of modalities which might not be consistent.

Indeed, designing an imaging system is a matter of mutual concession among the transmission of the interrogating waves and detection qualities of the measurement system in terms of sensitivity and geometry. In other words, the utmost determinant of imaging performance is the overall properties of the aperture, the interplay between the transmission and detection capability. Withal, the reconstruction algorithm remains fairly an important indication of the system performance and plays a major role in accurate estimation of the investigating object properties.

The main goal of the present dissertation therefore is to address the current challenges and limitations exist in hybridizing the optoacoustic (OA) and ultrasound (US) imaging system. To do so, the optimal properties for designing a bimodal 2D handheld probe has been investigated in details in order to offer an integrated solution. Correspondingly an advance reconstruction algorithm has been elaborated toward the requirement of designed OPUS imaging system. Considering the ill-posed nature of the reconstruction [6], characterization of the design system solely based on the quality of final image accompanies with considerable level of uncertainty. To avoid the biased interpretation, a *de facto* performance assessment being capable of evaluating the potentials of the designed OPUS probe in an unbiased manner must be practiced.

The distinguishing features of this dissertation are introducing a new geometry for OPUS handheld probe and a systematic assessments based on pre and post reconstruction methods. The majority of our investigation is taking place over the aperture model matrix which is developed in the context of wave propagation in volume, emanated and sensed by the active surface of the aperture. The aforementioned features establish a framework for characterization of the performance of imaging system in an accurate manner. Moreover, it allows further task performance optimization.

## 1.2 Current OPUS systems, applications and limitations

Today US is recognized as a mature technology yet remaining as a developing imaging method. The amount of effort devoted to advance the approach whether improving the technological side or expanding its medical and biological applications corroborates the impact. Yet to further push the boundaries and relax the imposed restrictions of purely acoustic systems, other allied technologies are being explored. Among them, optoacoustic imaging has been of particular interest, owing to its merits of employing the optical contrast in an ultrasonic manner. Unlike US imaging, majority of the OA systems, including the commercially available ones are single purpose instruments designed for a particular task. Nevertheless, handheld probes tend to be exempt from this principle, along facilitating the dual modality combination of OA and US for clinical studies. This trend has been practiced over a decade by tagging the optical delivery system, to the linear handheld ultrasonic probe. Variety of applications have been proposed and developed with respect to the frequency response of the transducers and the wavelength of the utilized laser light. The range is not limited to diagnosis and may extend to staging, guiding therapy or even drug delivery [9] and theranostics [183, 67]. One particular target with high diagnostic value is angiography, which is a hallmark for cancer. Zemp *et al.* [182] examined the capability of high frequency transducer (30 MHz) in visualization of superficial microvascular networks to the depth of 3 mm. To visualize deeper vessels such as human legs, forearms vessel [111, 83] and carotid artery [86], lower frequency response linear array transducer (7.5 MHz) have been employed. Moreover, targeting specific chromophore by tuning the laser spectrum, whether endogenous or exogenous, allows to investigate the functionality and molecular composition of the underlying tissue. Multispectral acquisition of the vessel's wall [72, 28] with the purpose of staging atherosclerosis or plaque composition, monitoring the blood oxygenation which is related to oncology [88] or contrast agent [110, 167] for a better detection of tumor is of this kind. Additionally, 3D acquisition is also possible by mechanically translating the probe over the surface of the sample [47] or using a 1.75D [3] and 2D matrix array US probe [167] with application in oncology. The 3D acquisition allows to widen the limited view angle of the detection aperture and have a better estimation of the three dimensional structure of the targeted tissue. However, these probes are essentially optimized for ultrasound imaging. They are only able to ensure high resolution morphological data for US images by employing a proper beam forming technique [73, 160, 107], basically through increasing the number of projection in transmission. If utilized for optoacoustic acquisition, images may suffer from lack of accuracy in localization and imposed reconstruction artifact, because of lesser number of achievable projection and limited angle of view. Furthermore, the integration of light delivery system is another challenge for OPUS systems. The associate problems are optically induced clutters and reflection of the light at the irradiation side and are closely related to the skin pigmentation and the diameter and angle of the incident beam. For example the perpendicular illumination maximize the fluence [23] which is not achievable by utilizing the classical US probes. Albeit, clutters induced at superficial layers [128] can be dealt with either by adjusting the distance between irradiation side and US probe [61] or sophisticated post processing techniques [141, 71].

Recently, Dean Ben [29] reported the design of an universal handheld probe for multispectral real time volumetric OA imaging. Shortly, the probe houses a bundle fiber for illumination purpose in the center of the hemispherical shell where the staring passive transducers are situated in a multi-ring structure. While the perpendicular illumination is reserved, the spherical detection geometry provides allegedly enough tomographic view required for OA imaging. The potency of the probe have been evaluated in number of applications including angiography and monitoring therapy. In an effort, Fehm *et al.* [43] examined the efficiency of the probe for US pulse echo imaging, in a fashion similar to the laser ultrasound. Nevertheless, the results were not compelling compare with conventional ultrasonography in terms of contrast and resolution. On that account a perfect hybridization remains challenging and is left for a more adaptive design if favor of both imaging systems.

### 1.3 Questions to be addressed in this dissertation (contributions)

This dissertation is mainly devoted to the design and characterization of a hybridized universal handheld probe for OPUS imaging and developing an adaptive reconstruction algorithm toward the physical requirement of the designed system. Therefore the questions to be addressed in this thesis are in the following context :

- With respect to the handheld probe design
  - What is the optimum compromise between number and size of transceivers required for the successful OPUS handheld probe.
  - What would be the appropriate array geometry to enable dual modality acquisition.
  - What are the necessary parameters in order to characterize the performance of the designed system.
- With respect to the reconstruction algorithm
  - What is the optimal reconstruction algorithm in order to mitigate the artifacts arose from the nonideality in the designed system.
  - How far the adaptive weighting factors are relaxing the impose constraints by FBP/DAS algorithms.
  - How accurate the performance of model based reconstruction algorithm can be, by incorporating the transceiver response.
  - How responsive the handheld probe is to the acoustic source within the medium as a function of spatial location.

### 1.4 Overview of the dissertation

The organization of this work is as follow. Chapter 2 opens with the discussion on the basic physics of both imaging systems individually, by providing a brief background and the theory behind the image formation. It also reviews the postulated ideal instrumentation for both imaging systems and the consequences of non-idealized parameters. The purpose of this chapter is to underpin the building-block necessary for the upcoming chapters.

In Chapter 3, the development of imaging system forward model and its implementation for both OA and US is described. The models are based on acoustic wave propagation and the behavior of the transceivers in transmitting or sensing the emanated/reflected acoustic waves from the medium. The models will be employed for further evaluation and characterization of the imaging system performance and further, as imaging operator for model based image reconstruction in the subsequent chapters.

Chapter 4 proposes a framework for performance characterization of the imaging system based on the model explained in Chapter 3. It outlines the steps required for the pre-reconstruction evaluation of the imaging system. The performance assessment takes place mainly by two sets of analysis in quantitative and qualitative manner, namely voxel crosstalk matrix [136, 130, 13] and eigen-based analysis. The implementation of voxel crosstalk matrix for photoacoustic tomography are developed by Wong *et al.* [171] and is adapted for OPUS system. Necessarily it addresses the following concerns, spatial sensitivity and spatial aliasing. On the other hand eigen-based analysis reflects the overall performance of the imaging system in achievable amount of the resolvable data. Based up on these analysis, the ideal geometry for integration of OA and US will be discussed in details.

Chapter 5 is allocated to the volumetric image reconstruction algorithms and is divided into three sections. The first is an attempt to explore the optimum DAS based algorithm for US and extend the approach to OA. It aims to address the restrictions imposed by DAS based approaches and the possibility of relaxing them to the favor of integration purpose. The second part, deals



with the model based reconstruction approach based on the model generated in Chapter 3 that is incorporating the shape, geometry and the characterization of ultrasonic transducers. As the crucial step in the reconstruction approach is inverting the forward model, the focus will be on the regularization to deal with the ill-posed nature of this inverse problem. Last but not least the third part is devoted to the post-reconstruction evaluation of the design imaging system based on the final image.

As the proof of concepts, the experimental results are highlighted in Chapter 6. A single element has been scanned in the same fashion as the array to mimic the acquisition performance of the proposed geometry in chapter 5. The imaging performance of the proposed geometry for handheld probe, i.e segmented annular array, is evaluated and the feasibility of developing the array is discussed.

Finally chapter 7 provides a summary of the dissertation and prospective outlooks for the future works are suggested.



# CHAPITRE 2

---

## The Basic Principles of Optoacoustic Ultrasound Imaging

---

It is my inner conviction that the development of science seeks in the main to satisfy the longing pure knowledge.

---

Albert Einstein

### Abstract

The underpinning step in designing a bimodal system is to genuinely understand and gain insight about the physical principles of both parties, the optical and acoustic wave interaction with tissue and image formation. The similarities and differences between the modalities and the key-factors that affect the performance of each system must be realized in an etiological manner. As Alexander Graham Bell once puts it « before anything else, preparation is the key to success ». Thus the goal of this chapter is to provide a fundamental background with respect to the principle of two imaging systems and their inherent similarities and differences.

## 2.1 Introduction



ACOUSTIC imaging in general consists of revealing the underlying information about the investigating tissue, encoded in the form of acoustic pulses, hence seeing the sound. Although these information are initially in the form of acoustic waves, but later are being transformed to the electrical signals for further recording and post processing purposes. Acoustic imaging to many respects is obeying the same physical phenomenon that are ruling optical (wave) domain, which leads to developing elements with the similar functionality (*e.g. refractive or reflective*) such as acoustic lens and mirror ; or developing same techniques such as holography which is obeying the interference, diffraction and phase conjugation phenomena. However, it would be naive to postulate that the paradigm in acoustic imaging is always following optics. Generally, there are three phases of acoustic imaging namely, inducing, collecting and processing. The last two phases are taking place in a similar manner among all of the acoustic imaging devices. Acoustic transducers are collecting the encrypted acoustic waves emanated from the induced sources within the medium, followed by translation to the electrical signals. Normally, this is followed by further post processing actions with deciphering purposes, for example the localization of the sources based on time of flight, also known as *image formation*. The fundamental differences, however is stemmed from the mechanism of acoustic source generation inside the medium in order to study the features and characterize the objects of interest.

Following the same scenario, two modes of acoustic imaging<sup>1</sup> that can be mentioned with medical and biological applications are medical ultrasound (US) and its younger half-brother optoacoustic (OA) imaging. Ultrasonic pulse-echo (PE) is arguably one of the most efficient diagnostic tools in order to estimate the anatomical abnormalities and localization of the lesions. Just like its forefather, the supersonic reflectoscope [45], it is based on the idea of echo-locationing that estimates the depth of reflecting objects from the transducer by calculating the round trip time of flight  $t_{rt}$ . The desired pulse of sound can be generated by deriving the ultrasonic transducer as the transmitter and detecting the partially back-reflected energy (echoed wave) with the same (or neighboring) transducer functioning in receive mode. Echo-locationing is a straightforward process as the speed of sound found to be similar in majority of soft tissues and that is close to the speed of sound in water, due to their high water content. However, the reflection in biological tissue is happening due to the acoustic impedance ( $Z$ ) mismatches at the boundaries of soft tissues. The acoustic impedance is defined as  $Z = \rho\nu$ , with  $\nu$  denoting speed of sound and  $\rho$  the density of the medium. The speed of sound is a complex value itself. The real part is related to the elasticity  $K$  and density  $\rho$  by the following equation  $\nu = \sqrt{\frac{K}{\rho}}$ . The imaginary part explains the dispersion and frequency dependent attenuation via Kramers-Kronig relationship [115]<sup>2</sup>. Subsequently, the reflectivity of the reflecting surface for the incident wave at the angle of  $\theta_i$  can be calculated from the following formula :

$$R = \frac{Z_2 \cos \theta_i - Z_1 \cos \theta_t}{Z_2 \cos \theta_i + Z_1 \cos \theta_t}, \quad (2.1)$$

where  $\theta_t$  is the angle of refraction and that the following relationship " $\sin(\theta_i)/\sin(\theta_t) = \nu_1/\nu_2$ " holds at the boundary. Given the conservation of energy, the transmitted and most probably refracted (bent), energy can be found by  $T = 1 - R$ .

Therefore in PE technique, object localization and characterization is fundamentally subjected to the mechanical contrasts. The array of transceivers facilitates the aforementioned tasks by providing extra rooms for diversifying the transmitting energy and direction for generated wave and extra view angles for receiving the echoed energy, thus improving the estimation about the original object. The properties of generated wave is, to many extend, defined by the physical properties of the ultrasonic transducer. These features are including the bandwidth and wave field propagation *w.r.t.* the transducer size. By further considering the backscattering (or reflecting) objects as the source of emanating wave from the medium, the characteristics of the incoming wave in US-PE is foretold.

In essence, optoacoustic imaging is an extended variety of ultrasonic technique in which the acoustic waves are induced inside the investigating sample upon the deposition of optical energy. The transition of photons to broadband acoustic pulses is a complex interplay of several physical phenomena. Yet, the contrast in OA is inherent to the optical wavelength selectivity of the absorbents in the tissue rather than mechanical contrast. Unlike US, the acoustic properties of the generated wave, such as the amplitude and frequency spectrum, are highly dependent to the optical properties of absorbents (sources). Withal, the image formation is following the same time of flight concept and theretofore same algorithm can be employed for both, with minimal adaptation.

The presented thesis is concerned with designing a high throughput array for acoustic 3D imaging to address the physical requirement of both parties, OA and US techniques. Our interest is in hybridizing the two modalities in order to pursue the promises of delivering the complementary morphological, functional, anatomical and metabolic information of the tissue. To do so, we start with providing theoretical background on the physical phenomena associated with both modalities and their requirements, in a separate manner.

---

1. To our concerns, the definitions of acoustic wave are limited to longitudinal waves.  
2. The speed dispersion is often ignored as the effect is as insignificant as 0.01%MHz<sup>2</sup>

## 2.2 Basic of Ultrasound imaging

### 2.2.1 Ultrasonic wave interaction with the tissue

In the first glance, the concept of US pulse echo (PE) technique seems fairly easy, a set of ultrasonic short pulses generated by the transducers are eliciting the mechanical discontinuities (reflector) of the soft tissues, along their path. The reflected or backscattered echos are collected by the same or neighboring transducers (in-case of array imaging) and discontinuities are located in the formed image by the stated echo-locationing concept. Depending on the relative size of reflector ( $\Psi$ ) to the wavelength ( $\lambda_{emit}$ ) of the transmitted wave and also angle of incidence, the nature of reflected wave would differ. Therefore the reflector can be considered as an acoustic source itself, with acoustic properties to be found by the imaging system. For example, the so called Rayleigh scattering is taking place when  $\lambda_{emit} \gg \Psi$ , as is the case for red blood cells ( $\varnothing \approx 7\mu m$ ), which causes uniform and concentric reflection of the energy in all directions. This type of backscattering is strongly depending on the frequency such that the scattering cross section  $S = \kappa^4 \Psi^6$ , and  $\kappa = 2\pi/\lambda_{emit}$  is the wave number. For the object of the similar size as the wavelength  $\Psi \simeq \lambda_{emit}$ , diffuse reflection with redirected wavelets is the dominant effect. Even though the backscattered wave is of the shape of spherical wave, the energy of the wave is more concentrated toward the angle of incidence. The reflected energy is getting more directional with increase in  $\Psi$ . This type of backscattering is responsible for the visible texture of the soft tissue in the ultrasound image. The properties of the reflected waves are analogous to the generation of acoustic wave using the  $\lambda/2$  and  $\lambda$  size transducer, being used in phased and linear arrays respectively. Such an analogy allows to treat each reflectors as an acoustic source. The third case is when  $\Psi \gg \lambda_{emit}$ , then the so called specular reflection will take place, an effect that explains the bright appearance of boundaries, for example between tendons, fat and muscles, bones etc. The intensity of the reflected waves are conveying information about the compressibility and density gradient at the interface of the two tissues and can be found from the equation 2.1. However if the angle of incident violates  $90^\circ$ , it can affect the shape and amplitude of the received wave, or the echoed wave might not meet the aperture at all, depending on the aperture covering angle of view, thus the encoded information about the medium would be partially or totally lost.

### Attenuation

In the US imaging, the resolution is subjected to the so called resolution cell associated with the wavelength of the transmitted and consequently reflected wave. The wavelength and frequency ( $f$ ) of the acoustic waves are related by the speed of sound such that  $f = \nu/\lambda$ . The choice of ultrasound frequency for transducer is however, a trade off between the resolution and penetration (attenuation). The high frequency ultrasonic wave is encountering relatively more diffusion events, more rarefaction and compression over the course of propagation, thence smaller resolution cell can be provided at the cost of higher attenuation. The main phenomena associated with attenuation are absorption, refraction, reflection, scattering and diffraction. The first one is attributed to the viscoelastic forces between neighboring particles, relaxation mechanism of protein [12]<sup>3</sup> and temperature gradient within or between soft tissues [122]. The associated absorption with the viscosity is following a square law dependence relation, in contrast to the linear frequency dependence via relaxation process. Refraction and reflection are caused by the variation in density of the medium and depend on the angle of incidence taking place at the tissue interface, which in general are obeying the equation 2.1. However, their impact on the energy of traveling wave in soft tissues is low, in compare with the backscattering. Last but not least, the diffraction describes the divergence of the wave as it migrates away from the source, but also the convergence of the wave behind the reflecting (specular and diffusive) object and further the shape of the reflected wavefront. Diffraction and refraction are both detouring the wavelets of the wavefront, but unlike

---

3. The attenuation of acoustic wave is phenomenally a different concept in porous structure such as bone. Depending on the bone structure multiple effect such as viscous friction, scattering due to heterogeneity and mode conversion are playing major roles of which none may happen in soft tissues.

refraction, diffraction is a bending wave phenomenon that does not associated with the change in speed of sound of the medium <sup>4</sup>.

The diffraction, refraction and interference can be explained by Huygen's wavelets which later augmented employed by Fresnel and further work of Kirchhoff [50], yet widely recognized as Huygens-Fresnel principle. Huygen's wavelets are imaginary sources of spherical waves populating the entire surface of primary wavefront. At every time instance, the interference between these secondary wavelets define the direction of propagation and the ensemble wavefront. The Kirchhoff rectifies this postulation by adding obliquity factor  $K(\theta)$  to explain the direction dependent behavior of wavelet which originally was assumed to be uniformly spherical.

$$K(\theta) = \frac{1}{2}(1 + \cos(\theta)) \quad (2.2)$$

If the  $\Psi$  (size of the obstruction, or reflector) be smaller than  $\lambda$ , all wavelets are in-phase by default, thus the interference would be coherent and constructive. Therefore the wave will spread out at large angle, or even can be considered as fully spherical in case of  $\lambda/2$  or smaller. This is similar to the Fourier analysis perspective, the infinitesimal source can produce an infinitely rich in spatial frequency [60]. However, when the reflector size is  $\Psi \gg \lambda$ , the region where the wavelets are constructively interfering would be limited to the region extending in front of the reflector, with the same diameter. Outside the region, the destructive interference between wavelets is dominant. Therefore, diffraction effect can explain the backscattering and reflection. Not to mention that Huygen's principle can be used to derive the Snell's low in order to explain the reflection and refraction [60].

The diffraction is attributed to the fluctuation between the acoustic particles in the vicinity of the source and consequently set of wavelets constructive and destructive interference appears. This behavior can be explained by Fresnel diffraction. The robust behavior begins where the coherence movement between the particles causes a relatively uniform yet spreading out wavefront, known as the far field and governed by Fraunhofer diffraction. Depending on the geometrical appearance of the source relative to the wavelength of propagating wave, the pattern of divergence would differ accordingly. A practical rule of thumb is separating near field from far field, given by :

$$z > \psi^2/\lambda \quad (2.3)$$

According to the Babinet's principle [143], diffraction can explain the convergence of the wave beyond the opaque (reflecting) object, in a similar fashion. For example the disturbance introduced by an object smaller than  $\lambda$  to the migrating wave is negligible and the traveling wavefront remains unaffected, as if the thin object is transparent. Meanwhile for the  $\Psi \gg \lambda$ , convergence of the edge diffracted waves happens at "*Poisson spot*" in the transition zone between near field and far field. This effect is similar to the flat transducer natural focus, which happens in the transition stage between near field and far field and has the maximum intensity value.

$$z_{natural\ focus} = \frac{4\psi^2 - \lambda^2}{4\lambda} \quad (2.4)$$

given  $\psi$  as the size of transducer, or reflecting object. Also, for the disturbed wave by the obstruction, it can estimate the post obstruction behavior of traveling wavefront and in particular, the distance the wavefront needs to converge such that the obstruction never happened.

Over the course of propagation, if the incident wave is not canceled due to the reflection, it would further weakened due to absorption and diffraction, until the energy ultimately transfers to the medium. The reciprocal relationship between the size of the source and the angle of divergence causes faster attenuation of the wave energy. The rule of thumb is the 6 dB loss per doubling migration distance.

Last but not least, if the acoustic wave is broadband, due to the frequency selectivity of attenuation, the shape of the wave would change as well. Additionally it can be shown that when

---

4. The literal meaning of diffraction can be extracted from the Latin word *diffringere*, "*breaking up into different direction*".

the attenuation is related to the frequency of the wave, the acoustic velocity is also frequency dependent [115]. Soft tissues have their own attenuation and scattering properties and those properties are distributed randomly in inhomogeneous samples. Additionally, orientation of the object is another consideration factor. Muscle as an example, has illustrated lower attenuation for the wave passing along the fiber than across the fibers, almost as half the value[168]. Therefore, the selection of frequency components for the transmitting wave in PE imaging is of-course biased in the favor of application.

## Speckle

The insonified objects by a highly coherent wave are observed to acquire a peculiar granular structure. These ubiquitous structure are called speckle, are mainly considered undesirable, stemmed from the individual scatterer varying in strength and position *w.r.t.* the aperture and the wavelength of ultrasonic wave. The complex pattern bears relationship to the microscopic properties of the insonified parenchymal tissue. Rather it appears chaotic and unordered and is best described quantitatively by the methods of probability and statistics. Despite their random appearance, the pattern remains the same for the relative stationary geometry between aperture and object, an indication of their coherent level. Yet, slight change in the conditions will result to a new pattern, to the extent that the strength for the same point can be totally different, suggesting a dubious link to the tissue structure.

Speckles can be explained by the interference between wavelets of multiple scatterers with particular phase angle, occupying one resolution cell. Depending on the nature of interference, whether constructive or destructive, the gray value (strength) of the resolution cell is set. Overall speckle is not desirable in many conditions and is considered as artifact adversely affecting the quality of image, detectability of the small targets and deteriorating the resolution and contrast. As a matter of fact, there are various approaches to reduce the speckle level, such as compounding multiple acquisition varying in frequency, pulse length or scanning geometry [152] or applying adaptive coherent factors [21, 63]. However, their level must be kept, even in lower scale, in order to realize the boundaries of anechoic regions. Additionally, the appearance of speckle pattern is not limited to the Rayleigh scatterers, leaving some room for tissue stratification [142] based on their texture and adding further diagnostic value.

## 2.2.2 Ultrasonic transducers

The core of any acoustic imaging system is the transducer, a key element that allows the ultrasonic wave being applied on the sample and record the interacted wave containing information. Ultrasonic transducers perform the conversion of electrical energy to mechanical (ultrasound) and vice versa, therefore are widely used as transmitters, receivers or transceivers (both) of ultrasonic waves, ultimately defining the image quality. Although, the frontier of ultrasonic imaging has been expanded owing to the advances in the ultrasonic transducer, yet paradoxically it remains as a bottleneck for further advancing the application. For instance, the frequency of which the US transducers are working effectively is limited to a certain range. Before broadband transducers, non-linear and harmonic imaging were quite challenging. Also, the broad bandwidth comes with lesser distortion and higher resolution for the final image.

Since 1927 that ultrasound has been introduced to the medical field [172], variety of forms, size, materials and approaches are being practiced in order to optimize the generation or detection of acoustic wave with desired properties. Among them, three major techniques are piezoelectric transducers (PZT), micromachined ultrasound technique (MUT) and all-optical transducer, using photoacoustic effect.

### Piezoelectric transducer

As of today, the dominant technology for ultrasonic transducer is by the help of piezoelectric materials. These include piezoelectric crystals (*e.g* quartz, LiNbO<sub>3</sub>), ceramics (*e.g* PbZrTiO<sub>3</sub>) and

polymer films like polyvinylidene fluoride (PVDF). Indeed the preference is altering with application, and that requires technical compromise. Taking ceramics PVDF, the acoustic impedance of similar to human tissues allows a better mechanical coupling and more signal to noise ratio (SNR), at the cost of low electromechanical coupling efficiency of polymer material. Meanwhile, ceramic may not suffer from low electromechanical coupling but high dielectric constant and inflexible surface are the draw backs.

A typical PZT transducer is composed of five layers, respectively a backing block, active piezoelectric material, matching layer, lens and protective layer (wear plate). The characteristic of PZT transducers namely, resonant frequency, electromechanical coupling coefficient, quality factor, impedance, beam profile are controlled by the properties of aforementioned composition. The piezoelectric material is sandwiched by two electrodes and the combination allows the acousto-electric translation. There exists a rule of thumb associating the first resonant frequency ( $f_{resonant}$ ) of the material to its thickness ( $d$ ) via speed of sound ( $\nu$ ) such that :  $f_{resonant} = \nu/2d$ . At this frequency the material has the maximum deformation, leading to strong ultrasonic wave. While resonating, the material produces range of frequencies in adjacent to resonating frequency dropping in amplitude as it changes from  $f_{resonant}$ . This range with amplitude of at least half of the  $f_{resonant}$  is called bandwidth (BW). The quality factor ( $Q$ ) of the resonating system is related to the generated bandwidth via following equation :

$$Q = \frac{f_{resonant}}{BW} \quad (2.5)$$

demonstrating the reciprocal relationship between BW and high  $Q$  system. High  $Q$  system is a well isolated system from external forces inducing damping effect. Such a system is efficient in terms of required energy for keep resonating at  $f_{resonant}$ .

The backing block is made of a high attenuating material in order to damp the ringing of the housing that causes extra vibration, therefore shortens the acousto-electric impulse, increasing the bandwidth of the transducer. Alternatively, the bandwidth is shown to be increased by improving the electromechanical coupling efficiency using multiple matching layers. In fact, the electromechanical coupling efficiency is a measure of energy conversion efficiency and can be interpreted as a measure of sensitivity as well. Thus the advantage of multiple matching layers is two fold. A good example is  $\text{PbZrTiO}_3$  which is conventionally used in ceramic PZT, for its high piezoelectric efficiency. Yet, its high acoustic impedance is associated with high reflection at the two ends, leading to ringing effect and spurious reverberated echoes in the tissue and lower sensitivity. As a remedy, the low acoustic impedance materials is added to ameliorate the mismatches effects and increase the bandwidth as the matching layer operates at different frequencies [66].

The nature of protective layer is determined by the either of two modes of transducer, immersion or contact. To maximize the transfer of acoustic wave, the quarter of wavelength thickness is considered but sometimes deliberately thickened for wedging purposes. The lens is used to diffract the generated acoustic wave, with focusing or defocusing purpose. However if the PZT materials are flexible, the same effect might be achieved with no loss by bending the surface of transducer. Yet, this bending is limited to certain degree.

## Micromachined Ultrasonic Transducers

Micromachined ultrasonic transducers (MUTs) are moderately a new family of transducer based on microelectromechanical systems (MEMS) technology. The technology is attractive from the processing perspective where the micrometer precision is effectively improving the performance of transducer, compact form factor and in case of array imaging, the consistency among the elements behavior. There are two types of MUT transducers, capacitive MUT (CMUT) and piezoelectric MUT (PMUT) being widely developed with great promises for medical ultrasound.



## CMUT

Since the invention in mid 90s [54], CMUT technology grabbed a lot of attentions specifically in the medical ultrasound, owing to its moderately easier and more precise fabrication and broad bandwidth response. As the name suggests, the transduction of energy is taking place by Coulomb force between the capacitor plates. Suppose that only one plate is mobile, the basic principle can be simplified as follows. The two plates are charged by a DC voltage (*aka.* bias voltage), creating an electrostatic attraction force in between, which is being opposed by the stiffness of the mobile plate resisting the attraction. Applying the electrical signal (AC) induces vibration over the surface of mobile plate hence ultrasonic wave is being generated. Similarly, when the mobile plate is subjected to the acoustic wave, the capacitance is being modulated relative to the frequency of incident acoustic wave and that, an electronic signals will be generated knowing the relationship between the capacitance ( $C$ ), voltage ( $V$ ) and charge ( $q$ ) hold as such  $C = q/V$ . The generated current is a function of three variables, the bias voltage (DC voltage), the capacitance and characteristic of incident wave.

The idea of using capacitive transducers<sup>5</sup> is dated back to 19<sup>th</sup>. The hurdle, however was the required high electric field for a thin gap of capacitor in order to obtain the large coupling coefficient in the same range as of PZTs. As it has been foreseen by Paul Langevin [68], it must be in order of MV/m. According to the Paschen's law, in such a condition the spark voltage can be avoided by a very thin gap. This is achieved thanks to MEMs technologies which has allowed this centennial idea to develop and being practiced. CMUT's building blocks are cells made of micron size metal plate (or membrane, top electrode) suspended over the vacuum gap of sub micros size and a fixed plate (substrate, bottom electrode) normally made of silicon, together acting as a capacitor. For the safety aspect, in medical application the transducer is being electrically insulated by coating a layer of polymer on top of the metallic membrane [95].

The operating frequency of the system is a function of geometrical and mechanical properties of the membrane. Analogously, actuation of CMUT is following the same principle as PZT, except for the DC bias voltage that regulates the operation of CMUT, according to the aforementioned formula. On transmit, the deriving current is inducing the attraction force on the electrodes, deflecting the mobile electrode to the fixed one and upon release the membrane vibrates, creating the acoustic wave. Since the cell size is very small, the desired acoustic wave is a result of multiple cells populated and connected in parallel, operating in a synchronized manner. It is worthy to mention that the generated acoustic frequency is corresponding to the frequency of the applied current multiply by two. This is due to the unipolar property of the induced attraction force [39]. On reception, upon the incidence of the acoustic wave, a harmonic vibration of membrane changes the  $C$  and as a result  $q$ , transducing acoustic energy into the electric signal.

In compare to the PZT, CMUTs are miniaturized capacitors that demonstrated a superior performance *w.r.t.* the acoustic matching, size reduction, broader bandwidth, front-end electronics and more flexibility for complex geometries. However, there are some challenging areas left to be addressed such as transmit/receive sensitivity, acoustic crosstalk, high electrical impedance and high bias voltage around 200 V [134].

## PMUT

To many aspects, PMUTs are performing in the similar fashion as the CMUTs, except for the fact that in PMUT fabrication piezoelectric material of micron size is being employed, instead of the vacuum gap. The piezoelectric effect induces electric fields across the layers, which in turn causes the actuation. Therefore, the bias voltage and small capacitance gap is no more required for their operation [77]. They do this by offering higher capacitance and lower electrical impedance, leading to lower parasitic capacitance and consecutively higher sensitivity and SNR [65]. The thickness of piezoelectric film is between nanometer to 3 microns. It can be said that the resonant frequency of PMUTs is not a function of piezoelectric layer thickness, but similar to CMUT,

---

5. Electrostatically actuated transducer by Edison and Dolbear [69].

geometrical and mechanical properties of the membrane such as stiffness and intrinsic stress. The challenge is placing a well defined thin yet piezoelectric materials, and that requires significant effort and cost. For example, one particular challenge could be the fact that resonant frequency is highly subjected to the membrane residual stress [53]. Therefore the applied stress  $T$  during fabrication will dramatically alters the resonant frequency :

$$f_{resonant} \propto \frac{1}{2\pi r^2} \sqrt{\frac{D_E}{\rho h}} \quad (2.6)$$

where  $r$  is the radius of membrane,  $D_E$  is the flexural rigidity,  $\rho$  is the effective density and  $h$  is the membrane thickness.  $T$  can dominate  $D_E$  and alters the resonant frequency. As of today many research groups are investigating the optimum fabrication techniques and materials for PMUTs. Nonetheless, in compare to CMUT, PMUT is a younger technology and requires more development.

### Laser ultrasound and optical detectors

An attractive alternative to the MUT techniques is the all optical transducers in which photoacoustic effect has been employed for transmission of broadband signal and interferometric detectors in reception. Instead of electronic signals, normally two laser are being input as a set of input and output.

Over the years, variety of methodologies have been explored in order to ameliorate the transduction of optical energy to tone-burst-like acoustic waves (*i.e.* laser ultrasound), among them thermoelastic expansion [52] is recognized as a reliable mechanism. This transduction normally happens by photo-exciting metals with ultra-short laser pulses [153] that is followed by photon absorption, heat conversion and thermoacoustic relaxation, leading to generation of coherent phonons. Typically the irradiating light is focused with a focal spot size affecting the characteristic of the generated wave. Despite the fact that metal sheets are alleviating difficulties associated with fabrication, they are suffering from the low transduction efficiency, turn them to improper choice for medical ultrasound. For this very reason, a mixture of polydimethylsiloxane (PDMS) (high transduction efficiency) with black carbon (absorbent) is of favorite choices, obtaining over 20 dB in transduction efficiency [19]. The thickness of material is yet another parameter affecting the properties of generated acoustic wave. The aforementioned composite is acoustically attenuating thus thinner material is of interest which in turn tailors the frequency properties of the generated wave. However, the major determining factor for frequency content of the acoustic generated wave is the laser pulse duration, the shorter the duration of laser pulse, the higher frequencies components will be induced. Normally, for ultrasonic imaging where the desired frequency is not violating the range of 10 MHz, laser pulse in the order of 10 *nsec* is seemingly enough [84].

On the other side, for detection of an incoming acoustic wave, a common paradigm is the so called active optical detection employing a thin polymer Fabry P erot etalon [106]. The concept is fairly easy, a pair of optically reflecting facing each other sandwiching the polymer is used as the interface between the optical field and ultrasonic wave. The incident light from a continuous wave (CW) laser goes through multiple reflection, producing interference pattern that depends on the laser wavelength and optical path length. Upon incidence, the strain associated with ultrasonic wave induces vibration on one of the mirrors, alters the thickness, changes the optical path, modulate the optical pattern and finally the resonance condition, proportional to the amount of displacement. The key to the sensitive system is the optical wavelength *w.r.t.* the surface displacement, such that the altered phase can be measured. The resonance in the cavity happens when the optical path length is equal to the integer multiple of wavelength. Etalon based detectors are promising broader bandwidth of detection [10], omni-directional response and competitively more sensitive response, much more compact. In fact the array of transmit/receive can be minimized to micron size. As both measurement and excitation occurs optically, electronic errors are alleviated as well. The limiting drawback of these system, are their laser dependent high cost.

### 2.2.3 Array imaging

Otherwise focused transducers are normally used in macroscopic imaging, such as US-PE. While the behavior of transmitted wave is solely determined by the geometrical shape of the transmitting aperture (*i.e.* element/array), single element transducer is not able to sweep the beam. Earlier in this chapter, it has been stated that array imaging is facilitating the volume interrogation of the sample toward real time, by electronic steering the transmitted beam in the desired location. The steering is possible by phase adjusting the array toward the specific location or direction, such that the constructive interference only occurs at particular angle, destined for the traveling wavefront. The dynamic directivity and steerability of the array in return, imposes certain limit in the geometric positioning of the array "*the  $\lambda/2$  interelement spacing*"<sup>6</sup>. If the transceivers are small enough to allow this happens, they act as a point source and the individual near field would be too short that propagating wave are by their nature spherical. The interference between the generated spherical waves allows only the ensemble wavefront survives in the focused (or angled) direction. The rest of energy is going through the destructive interference, leading to interferometric nulling, except for the wave from marginal elements (diffraction rays). In the far field of the aperture (or at the focusing plane) the residual energy forms the diffraction lobes, also known as side lobes. This can be rectified by apodization, a weighting technique that tailors the amplitudes of generated wave source (elements) *w.r.t.* their location from the center of aperture, at the expense of directivity and perhaps the achievable resolution.

From Fraunhofer approximation, far field pattern can be approximated by Fourier Transform of the aperture. Intuitively it can be interpreted that interelement spacing larger than  $\lambda/2$  violates the Nyquist sampling criterion, and that yields spatial aliasing in the constructive interference of the wavefront, The consequence is out of scope energy formations, known as grating lobe (1st diffraction order). This has been discussed in detail by Johnson and Dudgeon [76]. If the desired steering angle is not too aggressive,  $\lambda$  interelement spacing is a good compromise between the generated energy, number of element and steerability. Considering a rectangle function for each direction of rectangular element showcasing a uniform behavior over the entire surface,  $\Pi(x)\Pi(y)$  represents one element behavior. This follows that the far field pattern of the element can be approximated by  $\text{sinc}(u)\text{sinc}(v)$ . Conceptually for transmission, it represents the beam patterns while for receive, the spatial/angular sensitivity. A convolution by the comb function (III) can extend this way of representation to an array with uniform interelement spacing. It is shown that the periodicity in the array, introduces the periodicity in the beam pattern, creating off-axis replica (grating lobe) of on-axis energy with lower amplitude. In polar coordinate, the grating lobes occurs at  $90^\circ$  for array with  $\lambda$  interelement spacing and almost non for  $\lambda/2$ .

The array that contains the  $\lambda/2$  characteristic is called phased array and can be classified into three categories, linear, planar and annular. Linear array is composed of small elements arranged equidistantly in a simple line assembly<sup>7</sup>. Thus steering/focusing is only take place in two dimensions. Planar array is extending the properties of linear array into three dimension by repeating the element positioning in the second dimension, a matrix structure over the surface of aperture. Annular array is categorized into two geometries. The first consist of a set of concentric rings enabling the spherical focusing but the steerability remains fruitless. Other is called sectorial (or segmented) annular [4], which is basically a set of elements distributed around one or multiple rings, has a higher capability of steering and focusing yet remained theoretical due to the complexity in manufacturing.

Conventional linear arrays are mainly composed of 128 (also 192 and 256) elements along their length, which is a reasonable compromise between aperture size, achievable resolution and number of channel required to actively and individually control the elements. Planar arrays however, might not benefit such an agreement as manufacturing a probe containing  $128 \times 128 = 16384$  elements is a formidable challenge in many regards, including electromechanical hinders, amount of data to be processed and acquisition time. What commercial probes are offering does not violate 2880

---

6. This can be also attributed to the Huygens principle

7. if the wide angle of view is of interest, such as abdominal examination, the curvilinear arrays are more suitable.

elements<sup>8</sup> and that, not all the elements are accessible simultaneously, mainly due to the limitation in the available digital acquisition systems (DAQ) with limited accessible channel. At best, the customized 1024 channels systems allow to derive  $32 \times 32$  elements of a matrix array<sup>9</sup>.

The volume acquisition is possible synthetically, by mechanically rotating/tilting scan the 1D linear array such that the pyramid-like volume can be reconstructed out of set of 2D images. The offered resolution is generally higher than what is achievable with the 2D matrix probes due to the number of elements for the synthetic aperture and aperture size. Nonetheless, such a technique costs the real time acquisition and is limited to 40 volumes per second [33]. Therefore pursuing dynamic acquisition for extracting functional information such as the brain functional imaging [32], Doppler cardiography, cardiac electrophysiology and tumor mechanical properties is left to 2D probes. The so called beamforming techniques allow to scan the volume by electronic steering the beam over the volume via adjusting the time between the transmitting elements. Beamforming can be used at both the transmitting and receiving ends in order to achieve spatial selectivity, by selecting certain elements in a random fashion. The selection or sub-sampling of the elements aims to avoid or minimize the periodicity in the position of elements [64]. In US PE, this is done by monitoring or calculating the transmit-receive radiation pattern [144] and that must null the cross-talk between the grating lobes in transmit energy and main lobe in receive and vice versa. This rule is also followed for sparse arrays in order to find the optimum location for the elements. The reciprocal relationship between the lateral resolution and aperture size and on top of that avoiding the grating lobes might be met by random configuration of elements over the surface of aperture. Often mentioned as *sparse arrays* [11], such an arrangement promises the utilization of lesser but larger elements, achieving reasonable level of signal to noise ratio (SNR), decrease computation load and mitigate the front-end complexity. Withal, the development of a sparse 2D probe for 3D ultrasonic imaging remains as an attractive challenge and the optimum configurations are still being investigated [131, 137] in order to achieve uniform insonification and sensitivity pattern over the desired field of view and keeping the dynamic range between main lobe to side lobe in a reasonable level.

## Image formation

The image formation in US PE is basically performs by scanning the ultrasonic beam generated by set of elements over the volume of interest, and recording the backscattered wave. The volume can be reconstructed by relating the position of transmitting and receiving elements to the echoed wave via time of flight. The spatial resolution in ultrasonic imaging is subjected to the quality of the trains of produced beams, sequentially insonifying the sample. Evidently, the optimum resolution provided by the aperture is achievable when the collected data by all transmit-receive combinations are available, *i.e.* full matrix capture (FMC) synthetic aperture, enabling the total focusing method (TFM). In this way, the investigating object is being insonified at all the available angles provided by the elements of the aperture in a synthetic manner (hence, synthetic aperture). The image reconstructed for every transmit-receive events is referred to as a projection. Therefore, coherent compounding of the back projections will allow to reconstruct the final image<sup>10</sup>.

The FMC or synthetic aperture focusing technique (SAFT) allows for focusing at every single points inside the volume of interest in a simultaneous manner. For an aperture composed of  $N$  elements, the FMC provides  $N \times N$  projections to be processed. Therefore the calculation time is increased with the increase in the number of elements, thus frame-rate is decreased. Another drawbacks is the acoustic power transmitted by single element, degrading the SNR. To cope with, sparse matrix capture (SMC) might be beneficial approach in a sense that the multiple employed elements in the transmission, would increase the SNR yet reduce the acquisition time. In each transmission, the employed elements are phase adjusted in a way to mimic the wave transmitted from a virtual source behind the transducers.

---

8. Philips

9. Vermon

10. This would be further discussed in chapter 5.

If the frame rate is of priority, then the plane wave imaging (PWI) might offer a good compromise between the spatial resolution, SNR and acquisition time. Basically, at every transmission, the delays are set such that the transmitted wave is a plane wave with a particular angular direction. The focusing is happening dynamically in receive, by spatial compounding the projection acquired from each angle. However, in order to provide a flawless wavefront, the periodic sampling with  $\sim \lambda$  spacing is indeed necessary. The utilization of all elements in every transmission event makes this approach less prone to noise and attenuation, what affects the TFM. Therefore, TFM is more practical for the array with larger elements yet lower in number, alias the sparse array.

## 2.3 Basic of Optoacoustic imaging

The optoacoustic imaging, also known as photoacoustic imaging is a unique methodology that reconcile the merits of optical imaging with ultrasonic resolution. It is based on the photoacoustic or more precisely photo-thermo-acoustic effect in which, the photons energy are translated to broadband acoustic pulses, hence laser generated ultrasound. The rich and selective interaction (specifically absorption) of the biological tissue with optical spectrum specifically within the visible and therapeutic window, enables optical imaging technique as a potent tool to probe the tissue specificity. Unlike the pure optical imaging that mainly rely on the ballistic photons, in optoacoustic imaging light scattering does not compromise the resolution, as long as the scattered photons are contributing to the generated acoustic pulse. In general, over the course of propagation in biological tissue, ultrasonic wave experience much less scattering than optics and that is up to three order of magnitude for soft tissues [37]. The advantage is furnishing the localization of optical absorbents deeper than one transport mean free path [114], upto few centimeters in the tissue at ultrasonic diffraction limit, of which the reconstruction is grounded. Thus this *light in sound out* technique is composed of several phenomena involving with coupling of optics and acoustics physics.

### 2.3.1 Light propagation in tissue

Light propagation in biological tissue is stemmed from the nature of photon tissue interactions susceptibility with tissue. Much like the ultrasonic wave, the electromagnetic waves are following the same governing equations along the undisturbed path. Yet, for the medium as turbid as biological tissue, where the scattering due to optical nonuniformity (refractive index) is highly dominant events over the course of photons migration, the wave coherency would be lost beyond certain regime, known as ballistic regime. Generally, light transport in turbid medium undergoes two regimes, ballistic and diffusion, the length of each defined by the wavelength based optical properties of the medium [114]. The ballistic is where the optical absorption is dominant while in diffusion regime the scattering overtake while photons undergo random walk. The border can be realized by so called mean free path (MFP), defined as  $1/\mu_t$  in which  $\mu_t$  denotes the transport coefficient and that is the sum of absorption coefficient  $\mu_a$  and scattering coefficient  $\mu_s$ . For propagation distances  $<$  MFP, ballistic regime rules where  $\mu_a \geq \mu_s$  and that can be followed by geometrical optics.

Further, when multiple scattering events takes place, the photons are about diffused with a random walk of step size  $1/\mu'_s$  related to the reduced scattering coefficient  $\mu'_s = \mu_s(1-g)$  in which  $g$  denotes the anisotropic factor<sup>11</sup>. The larger value for  $g$  is accompanied with more penetration due to the more forward scattering and larger penetration depth [114]. To further classify regions, the transport mean free path (TMFP) can be defined as  $1/\mu'_s$  and that, for  $>$  TMFP where  $\mu'_s \gg \mu_a$ , which is the case for most of biological soft tissues, light is already diffused.

Therefore a more delineate formulation might be needed to approximate the multiple scattering events. Generally, the radiative transfer equation (RTE) is more favorable due to its ability in providing the explicit solution for majority of the cases. For a medium, the RTE is articulating the optical properties in reference to the measurable quantities and that models the energy loss

<sup>11</sup>. Represents the mean cosine of scattering angle of all photons after single scattering with a value between 0.8-0.95 for biological tissue.

by extinction (total attenuation) and divergence, over the course of migration. The space time dependent equation for RTE is given by [59] :

$$\frac{1}{c} \frac{\partial L(\vec{r}, \hat{s}, t)}{\partial t} - \nabla L(\vec{r}, \hat{s}, t) \hat{s} + \mu_t L(\vec{r}, \hat{s}, t) = \frac{\mu_t}{4\pi} \int_{4\pi} L(\vec{r}, \hat{s}, t) p(\hat{s}, \hat{s}') d\hat{s}' + Q(\vec{r}, \hat{s}, t) \quad (2.7)$$

where  $c$  is the speed of light in the medium,  $Q$  is the source function and  $p(\hat{s}, \hat{s}')$  normalized differential scattering cross section, declaring the probability that photon scatters from direction original direction  $\hat{s}$  to  $\hat{s}'$ . This equation is not trivial to be analytically solved for complex geometries. One approach is employing numerical method to find the solution for RTE but at the cost of time. The governing equation for propagating optical wave in the medium can be culled from the solution to the RTE, of which the diffusion approximation takes over the hypothesis of isotropic distribution of energy radiance ( $L$ ) within the turbid medium. The diffusion approximation which considers the biological tissue as accordant lattice, endeavors to solve RTE with a random walk model [48]. The approach is popular owing to its mathematical tractability, is only valid in the diffusion regime, hence the name diffuse photon density waves (DPDW). The first assumption to derive the solution, is that the energy radiance  $L$  is only linearly anisotropic, thus

$$L(\vec{r}, \hat{s}, t) \hat{s} = \frac{1}{4\pi} \phi(\vec{r}, t) + \frac{1}{3\pi} J(r, t) \cdot \hat{s} \quad (2.8)$$

where

$$\phi(\vec{r}, t) = \int_{4\pi} L(\vec{r}, \hat{s}, t) d\hat{s}$$

By substituting the above equation into the equation 2.7, DPDW equation is given by [16] :

$$\frac{\partial \phi(r, t)}{c \partial t} + \mu_a \phi(\vec{r}, t) - D \nabla^2 \phi(\vec{r}, t) = Q(\vec{r}, t) \quad (2.9)$$

where  $D = 1/3(\mu_a + \mu_s')$  is the diffusion coefficient. The DPDW can be related to the Helmholtz wave equation in frequency domain such that :

$$(\nabla^2 + k^2) \Psi(\vec{r}, \omega) = -\frac{Q(\vec{r}, \omega)}{D} \quad (2.10)$$

where  $k^2 = -\mu_a D$  and  $\Psi(\vec{r}, \omega) = F\{\phi(\vec{r}, t); t \rightarrow \omega\}$  is the Fourier transform of  $\phi$ . The analytical time dependent solution to the equation 2.10, for homogeneous medium exist and that can be found in the job of Patterson [121] as such :

$$\phi_q = \frac{e^{-(r^2/4Dct + \mu_a ct)}}{(4\pi Dct)^{3/2}} \quad (2.11)$$

The analytical solution for the spherical and cylindrical homogeneity, can be found in the job of D. Boas *et al.* [16] which is further augmented by S. Li *et.al* [93] for the optoacoustic sources embedded in the otherwise homogeneous turbid medium. Alternatively, Monte Carlo stochastically simulates the single photon migration in tissue and through this way approximates the energy radiance [162]. This method is also computationally expensive but considered as a gold standard technique. Therefore, the light propagation is playing an important role in optoacoustic imaging, specifically if the quantitative amount of chromophores based on the energy deposition is of interest [94].

### 2.3.2 Photon to phonon translation, origin of optical contrast

The propagating light in tissue encounters series of scattering and absorption effects of which the second one is taken place by chemical structure of molecules known as chromophore. The chromophore are recognized by the spectrum, the range of optical wavelength that they partially absorb the energy and happens to be selective to the amount that delivers the high optical contrast between the biological tissue with different ingredient of chromophores.

The photoacoustic effect is a series of energy conversion initiated by energy deposition of the modulated light in time (or amplitude and frequency (chirp) [150]). The absorption gives rise to slight temperature rise ( $< 0.1K$ ) which is followed by thermo-elastic volume expansion and further elastic relaxation. The vibration generates a broadband acoustic wave, encoding information about the geometrical and perhaps chemical (spectroscopy) properties of the light absorbing structures. The induction of acoustic wave can be taken place by either of optically short pulse laser (nano second) of respectively high peak power or frequency modulation of respectively low mean power continuous wave lasers [52]. In this section, we only touch the physics of the time domain approach in photon to phonon conversion for biological imaging.

#### Time domain

The irradiation of the tissue by a short pulse laser leads to the energy deposition of photons in the form of heat. The pulse length must be shorter than the thermal confinement to avoid thermal diffusion as well stress confinement. The latter, also known as acoustic confinement is to ensure that the energy would not dissipate in the form of acoustic wave, before its complete deposition. The stress confined pulse length must be shorter than  $\tau$ , given by :

$$\tau = \frac{l}{\nu} \quad (2.12)$$

where  $l = 1/\mu_t$  denotes the length of absorbent. In another word  $\tau\nu/l$  must be less than unity otherwise the quality of the induced wave deteriorates. This condition allows the rapid transition of adiabatic thermo-elastic effect in which the volume change ( $dV$ ) due to the heat deposition can be expressed as :

$$dV = V(\beta\Delta T - \kappa p_0), \quad (2.13)$$

where  $\beta$  is the volume expansion thermal coefficient,  $\Delta T$  is the change in the temperature,  $\kappa$  is the isotherm compressibility and  $p_0$  is the induced pressure. When the change in volume is much smaller than the volume itself, *i.e.*  $\frac{dV}{V} = \epsilon$ , the relation ship between the induced generated pressure due to the deposited heat is given by [126] :

$$p_0 = \frac{\beta H(\vec{r}, t)}{\kappa \rho C_p} \quad (2.14)$$

knowing that  $\Delta T = \frac{H(\vec{r}, t)}{\rho C_p}$  with  $C_p$  denoting the heat capacity at constant pressure (volume),  $\rho$  is the density and  $H$  is the rate of optical energy deposited per unit volume per unit time ( $J.m^{-3}.s^{-1}$ ), in the form of heat and is commensurate with the intensity of the laser. In fact, it can be defined as the product of fluence of laser light and absorption coefficient of the chromophore  $\mu_a$ ,  $H(\vec{r}, t) = \mu_a \phi$ . Moreover, since the pulse is short, the time dependency of the heat can be approximated by Dirac delta function such that  $H(\vec{r}, t) = A(\vec{r})\delta(t)$ , with  $A(\vec{r})$  denoting the spatial distribution of absorbed energy. Reforming above equation 2.14, one can simplifies the above equation further, by introducing the Grüneisen parameter  $\Gamma = \beta/\kappa\rho C_p$ <sup>12</sup>. Therefore, the initial induced pressure  $p_0$  is :

$$p_0(r) = \Gamma A(\vec{r}). \quad (2.15)$$

12. The Grüneisen parameter is a unitless parameter that relates the initial pressure to the absorbed energy and can be interpreted as a measure of translatability of the photon to phonon, by the chromophore.

The thermal confinement assumption for short pulse laser makes light of heat conduction thus by detecting the pressure wave at the surface of tissue ( $p$ ), one can approximate the location and perhaps the amount of the chromophore containing structure (by calculating for the  $\mu_a$ ). Hence, the acoustic response is encoded information about optical properties of the tissue. This is given by the Green's function approximation to the wave equation [165], such that :

$$\begin{aligned} \frac{\partial^2 p(r, t)}{\partial t^2} - \nu^2 \nabla^2 p(\vec{r}, t) &= \Gamma A(\vec{r}) \\ \therefore p(\vec{r}, t) &= \frac{\Gamma}{4\pi\nu^2 |\vec{r} - \vec{r}_0|} \frac{\partial}{\partial t} \left( \delta\left(t - \frac{|\vec{r} - \vec{r}_0|}{\nu}\right) \right) \end{aligned} \quad (2.16)$$

This will be further discussed in chapter 3 section 3.2 and is used in chapter 5 for reconstruction algorithms as is the objective of optoacoustic imaging. The frequency response of the generated optoacoustic wave is a function of laser pulse duration and the size of absorber itself. For example, lower frequency components are dominant in the spectrum of induced ultrasonic pulse by the larger absorber. It is understood that for a finite size absorber, the interference between the constituent pointlike optoacoustic sources are composing the final generated wave and that, can be approximated by the convolution of Green's function for point source and temporal envelop of the deposited laser energy [116] :

$$p(\vec{r}, t) = \frac{\Gamma}{4\pi\nu^2} \frac{\partial}{\partial t} \int \frac{A(r)}{|\vec{r} - \vec{r}_0|} \delta\left(t - \frac{|\vec{r} - \vec{r}_0|}{\nu}\right) dr_0 \quad (2.17)$$

The explicit solution to the equation 2.17 is given for particular cases. For instance, the analytical model for a spherical absorber of radius  $a$ , being uniformly excited is expressed as [163] :

$$p_0(r, t) = \begin{cases} \frac{\Gamma \cdot (a - |r - ct|) \cdot (r - ct)}{2r} & \text{if } |t - \frac{r}{\nu}| \leq \frac{a}{2\nu} \\ 0 & \text{else} \end{cases} \quad (2.18)$$

This gives rise to the bipolar N-shape signal of optoacoustic, a succession of compression (positive) and rarefaction (negative) phase with temporal width indicative of the original size of the source. For a point source equation 2.18 can be further reduced to  $\Gamma \cdot (r - ct)/2r$ .

### Boundary build-up effect

Speckle is the direct consequence of interaction between coherent wave and subresolution scatterers, followed by the interference between the backscattered wavelets with absolute randomized phase. Unlike most of the coherent imaging system, optoacoustic hinges upon the absorption contrast rather than scattering. The superposition of wavelets from the subresolution absorbers along the unified body however, experience slightly different interference that let them devoid speckle. According to Z. Guo *et al.* [51] speckle formation can be attributed to the polarity of the incoming (toward the detectors) wavelets and their initial phase. In US PE, depending on the relative acoustic impedance of the scatterers *w.r.t.* the medium, the polarity can be flipped or maintained which means positive and negative initial phase. While interfering, partial overlapping of the out of phased and in phase wavelet results in random structure of the main wavefront. In contrast, the simultaneous generation of optoacoustic waves with akin polarity (with leading compression phase), yet randomized phase results in phase delay variation they propagate toward the surface of the tissue, except for the boundaries neighborhood. This in turn, leads to the constructive interference at boundaries, yet depending on the bulk object density (*i.e.* the distance between the optoacoustic pointlike sources within the bulk objecting structure should be less than their size [30]), generated wavelets will cancel out for adjacent absorbers except for the boundaries, where constructive interference yield the so called "build-up" effect, owing to the high correlation among them.



### 2.3.3 Optoacoustic image formation

One dimensional time resolved optoacoustic signals (A-scans) are collected by the ultrasonic transducer/s and that enables the reconstruction of the volume or if preferred cross-sectional image. Generally, optoacoustic imaging is divided into two main categories, microscopy and tomography. Similar to other types of microscopes, either optical or acoustics, in optoacoustic microscopy the focal area is scanned over the region or volume of interest. Normally, a focused ultrasonic transducer is employed to enhance the sensitivity [164]. In optical resolution microscopies, the optical and acoustic focal points are coincided, forming a confocal system. The light delivery can take place by variety of shapes, included the dark field illumination with the transducer in the center, optical fiber embedded in the center of the mono element transducer or forward mode meaning that the sample is situated between illuminating optical fiber and ultrasonic transducer. The spatial resolution can be defined by the employed focused ultrasonic transducer or optical delivery system.

The optoacoustic tomography on the other hand, is employing unfocused (or defocused) ultrasonic transducer/s to form the image. The acquisition is taking place synthetically by scanning mono-element transducer around the sample or using the array of elements. Deep OA imaging is based on recording the unscattered yet diffracted acoustic waves which originally are induced by absorbing the scattered photons. Unlike optical wave, the depth limiting of acoustic based imaging is not scattering but attenuation. Practically speaking, the depth to resolution ratio in OA is around 200 [14]. Nonetheless, the resolution is limited to the dynamic focusing provided by the aperture, much like the ultrasound receive beamforming. The array can be of three geometries, planar (linear in 2D) arrays ultrasound, concave (cylindrical or spherical) and circular arrays. The latter is capable of providing the full view image quality ( $> \pi$  angular coverage) as the elements are enclosing the object. Indeed, the view angle is an important factor in image quality which along the number of elements are resolving the achievable spatial (angular) frequency<sup>13</sup> by the aperture. In fact, accurate optoacoustic reconstruction is only insured when the sample is fully enclosed [177]. Yet, because of its geometry which encapsulates the whole sample, it may offer limited clinical applications such as breast cancer [85, 40] and osteoarthritis [148]. The other two can be employed in reflection mode and are more suitable for clinical applications. The planar geometry is used for bimodal optoacoustic and ultrasound imaging, since the arrays are available with variety of frequency response and the only challenge is coupling the optical delivery system [128, 61]. However, due to their finite aperture size and limited element size ( $\lambda/2$  interelement spacing), the quality of delivered image is compromised. What is noteworthy is that the success of these arrays in US PE imaging is due to the fact that the transmitted beam can be controlled, thus the investigating volume is visited from multiple angles. Plus the fact that the SNR can be increased by increasing the number of projections or focusing the beam inside the tissue. The number of projections in optoacoustic imaging is limited to the number of elements. A reasonable comparison in terms of SNR and resolution could be ultrasonic flash mode of imaging where acquisition is taking place by only one transmission and that is an unfocused planar beam propagating normal to the aperture. Hence, employing the conventional array for optoacoustic imaging is associated with limited-view artifacts due to the lack of angular frequency. The optimum reconstruction only belongs to the structure parallel to the array [127].

Last but not least, the concave geometries are a trade off between the circular and planar, with promises of improving the angle of view, yet by enlarging the element size, SNR can be increased as well [29, 40]. These arrays seems impeccable for only optoacoustic systems. Yet, their relatively small field of view might not be interesting for bimodality such as OPUS as the advantages of conventional ultrasonic images may not be met.

Regardless of the aperture geometry, the image formation is coming of two main form. The so called back projection is a gold standard algorithm which is estimating the object by solving the equation 2.17 for  $p_0 = \Gamma A(r)$ , for every recorded signal. Therefore, the final number of projections is not exceeding the number of employed transducers, and that affects both SNR and resolution. In practice, the concept is much like the ultrasonic delay and sum which is functioning based on time

13. More details can be found in chapter 4 section 4.2.2

of flight. Both of these are based on the same assumption, detectors are having omni-directional response with  $< \lambda$  interelement spacing. This is only true for the planar geometry. The second approach is model based reconstruction in which the so called forward mode, the projection of every voxel on the aperture, is measured or calculated and employed in sort of inverse problem. The formation of such a model is pursued in chapter 3 while in chapter 5 which is designated to image reconstruction, both of these approaches are explained and employed.

## 2.4 Conclusion

In this chapter an effort has been made to provide a learning ground for the reader with the principles of the two modalities of optoacoustic and ultrasound imaging. The chapter commenced with the interaction of ultrasonic wave with biological tissue, and that is followed by the fundamental of ultrasonic imaging including the imposed rules by the physics of acoustics, ultrasonic detectors and arrays which further leads to diffraction limited image formation. It was further pursued by briefly touching the physical phenomena involved with photoacoustic effect, namely optical wave propagation, light and sound coupling and optoacoustic wave generation. Through out the chapter, the similarities and differences between the two modalities have been discussed in order to pinpoint the crosscommunication and enabling the exploitation of possible complementary values by tandem employment, hence leverage the gain from the same probe.



# CHAPITRE 3

---

## A Discrete Imaging Model For Optoacoustic Ultrasound Imaging

---

I am an artist's model.

---

Albert Einstein

### Abstract

The presented thesis is mainly concerned with the design and characterization of an acoustic array to be used as a universal handheld probe. For that purpose, modeling the behavior of the array and its performance as an imaging system is fundamental. Generally this task is associated with solving the acoustic wave equation and its interaction with the active area of the array sensors. The main purpose of this chapter is to derive a discrete linear model for optoacoustic (OA) and pulse echo (PE) ultrasonic imaging based on the solution to the acoustic wave in linear regime.

### 3.1 Introduction

**H**YBRIDIZING optoacoustic and ultrasound imaging are facing some difficulties due to the fundamental differences in the physics of the two modalities. Yet, rather than acoustic wave generation, the physical phenomena in wave propagation and reception remain the same. Following the aforementioned hypothesis, a model can be obtained that explain the behavior of both modalities in imaging of the induced acoustic sources, irrespective of their nature (optically induced or backscattering the transmitted wave).

The main purpose of such a model is to determine the detection aptitude of the array in sensing the emanated acoustic wave from any point in the medium within the Field of View (FOV), given the geometry and boundary conditions. In order to have a realistic model, the characteristics of the sensors must be incorporated. These include the imposed diffraction effect by the finite size of the sensor and acousto-electric characteristics of the transducer. The latter defines the frequency response of the transducer and together with the former, they define the angle of vision parameter for transceiver known as spatio-frequency response or directivity.

Thereby the aim of the presented chapter is to model the transmission (for US), propagation, scattering and reception process. There are variety of the different approaches in modeling the acoustic wave propagation. These include but not limited to fast near field method [103, 104], analytical solution to the Rayleigh-Sommerfeld integral [180, 58, 146, 156], impulse response method [146, 99, 75] and angular spectrum method [140, 147]. The last two approaches are closely interconnected. In fact, the relation between them can be explained by spatial-temporal Fourier transform [145]. While the angular spectrum method determined the field on the plane of

interest at particular time, the impulse response approach is more suitable for localizing the time-dependent wave [145] in space. The impulse response method is commonly used for characterization of spatial-temporal characterization of the transient field due to its simplicity and comprehensiveness in determining the time dependent pressure at a given point. The approach which is based on the Green's function solution to the wave equation, simplifies the transient field as the convolution between impulse response and the normal velocity at the source. The impulse response itself is the convolution of acousto-electric impulse response (AIR) and spatial impulse response (SIR), explaining the spatio-frequency response of the transducer in far field. SIR is determined by the geometry of the active area of the transducer and its imposed boundary condition.

The remainder of the chapter is organized as follows. In section 3.2 we review the Green's function solution to the acoustic wave equation for a certain boundary condition. Using SIR, section 3.3 showcases the effect of transducer geometry on the transient/received field. Analytical solution to SIR has been derived for few geometries and will be briefly mentioned. Section 3.4 explains the formation of discrete linear model that represents the behavior of the array or *total system response* which is determined by both AIR and SIR. It also discusses the reception model which is formed as the average of incoming wave over the surface of transducer. The diffraction effect and consequently the imposed low-pass filter caused by the averaging effect will be discussed. Finally, section 3.5 discusses the main promises of IR such as calculation of acoustic radiation as well as weighting factor in time-delay based reconstruction algorithms.

## 3.2 Green's functions and acoustic wave equation

The governing equation for the acoustic wave propagating from the source within an isotropic and homogeneous compressible medium is given by [44, 109]

$$\frac{\partial^2 p(r, t)}{\partial t^2} - \nu^2 \nabla^2 p(r, t) = S(r, t), \quad (3.1)$$

where  $\nabla^2$  is the Laplace operator, the scalar function  $p(r, t)$  is the spatial  $r$  and temporal  $t$  dependent acoustic pressure,  $\nu$  is the speed of sound of the medium and  $S(r, t)$  is the deriving function of acoustic source. One can also express the the wave equation in terms of velocity potential  $\phi$ , knowing its relation to the pressure :

$$p(r, t) = \rho_0 \frac{\partial^2 \phi(r, t)}{\partial t^2}, \quad (3.2)$$

with  $\rho_0$  being the equilibrium density of the medium. For monochromatic wave, the above equation can be stated otherwise, which is equivalent to *Helmholtz's equation*

$$\nabla^2 \phi(r) + \kappa^2 \phi(r) = S(r), \quad (3.3)$$

where  $\kappa = \lambda/2\pi$  is the wavenumber and  $\lambda$  is the wavelength corresponding the frequency of the propagating wave. From the ultrasonic perspective, where PE is of interest, source can be considered as the excitation pulse to drive the transducer and will be denoted by  $S_t$ . On the reception, source can be regarded separately as an insonified backscatterer providing a measure of reflectivity [125] and will be denoted by  $S_r$ , which is a function of density and adiabatic compressibility. It can be extended to OA, where sources which are optically absorbing mioties inside the medium, being capable of absorbing and translating the incoming photons energy into the acoustic waves via photoacoustic effect.

Irrespective of the source nature, one can derive the analytical solution to the wave equation, using Green's function [166, 146]. Considering the left hand side of the equation as a linear partial differential equation, solving for  $p$  requires to inverse the differential operator. Green's function is playing the pivotal role here, as mathematically, it is the kernel of the inverse of the differential operator. Otherwise stated, it is the response of the system to a point source  $S_p$  [100] or the spatial impulse response. As a matter of fact, Green's function can map the excitation pulse to

the pressure field. The mathematics of this can be found elsewhere [108, 50], but generally the time domain solution reduces to the time *Helmholtz's* equation.

$$p(\vec{r}, t) = \int_T \int_{\Omega} \left( p(\vec{r}_0, t_0) \frac{\partial G(\vec{r} - \vec{r}_0, t - t_0)}{\partial \mathbf{n}} - G(\vec{r} - \vec{r}_0, t - t_0) \frac{\partial p(\vec{r}_0, t_0)}{\partial \mathbf{n}} \right) d\Omega dt_0, \quad (3.4)$$

where  $\Omega$  is the enclosing surface,  $\partial/\partial \mathbf{n}$  signifying the partial derivative in the outward normal direction at each point on the enclosing surface,  $\vec{r}_0$  and  $t_0$  are initial position and time of wave at the source and  $G(\vec{r} - \vec{r}_0, t - t_0)$  is the Green's function for a free space  $G^F$  is defined as follow :

$$G^F(\vec{r} - \vec{r}_0, t - t_0) = \frac{\delta(t - t_0 - |\vec{r} - \vec{r}_0|/\nu)}{4\pi |\vec{r} - \vec{r}_0|}, \quad (3.5)$$

The physical interpretation of the above formula is nothing but spherical radiation of a point source (*i.e.* impulse response of the medium). The Green's function can be set to satisfy certain set of conditions including the boundary and initial conditions. Depending on these conditions, *Helmholtz's* equation will be modified as well. A case in hand is when the US transducer is of concern. These conditions normally are imposed by the type of baffle [109] and consequently alter the IR. The free space Green's function is explaining the case where the field is not disturbed. For the case where the source (*i.e.* transducer) is situated on an acoustically rigid baffle ( $Z_{trans} \ll Z_{baffle}$ <sup>1</sup>), the contribution of the irradiated field is limited to the active surface area of the transducer. Therefore the Green's function for the hard surfaces  $G^H$  can be reformulated as :

$$G^H(\vec{r} - \vec{r}_0, t - t_0) = \frac{\delta(t - t_0 - |\vec{r} - \vec{r}_0|/\nu)}{2\pi |\vec{r} - \vec{r}_0|}, \quad (3.6)$$

Considering the finite size of the transducer, the emitter wave is expected to be planar in the near field. In such a condition, the normal derivative pressure is related to the source velocity such that :

$$\frac{\partial p(\vec{r}_0, t)}{\partial \mathbf{n}} = -\rho_0 \frac{\partial}{\partial t} \nu_n(\vec{r}_0, t), \quad (3.7)$$

Thus, the equation 3.4 can be restated as well known First Rayleigh-Sommerfeld integral [132, 50] to model the PZT transducers.

$$p(\vec{r}, t) = \rho_0 \frac{\partial}{\partial t} \int_T \left( \int_{\Omega_R} \nu_n(\vec{r}_0, t_0) \frac{\delta(t - t_0 - |\vec{r} - \vec{r}_0|/\nu)}{2\pi |\vec{r} - \vec{r}_0|} d\Omega_R \right) dt_0, \quad (3.8)$$

with  $\Omega_R$  being the active surface of the transducer and  $T$  the time span. For the case that the normal velocity is constant over the surface of the transducer, the pressure can be rewritten as the temporal convolution,

$$p(\vec{r}, t) = \rho_0 \frac{\partial}{\partial t} \nu_n(t) * \left( \int_{\Omega_R} \frac{\delta(t - |\vec{r} - \vec{r}_0|/\nu)}{2\pi |\vec{r} - \vec{r}_0|} d\Omega_R \right), \quad (3.9)$$

The first term of the above convolution is attributed to the uniformly distributed normal velocity over the transducer or acoustico-electric transfer function. If the transducer is being derived by an excitation pulse, in transmission mode, the term incorporate the signal via an internal convolution with the transducer AIR. The second term of the equation, the integral part, is known as spatial impulse response (SIR) which is describing the acoustic wave propagation from the transducer to the observation point  $r$  and/or the receive response to the incoming wave originated at  $r_0$ . Together they determine the spatio-frequency response of the transducer with an active surface area of  $\Omega_R$  and acoustico-electric transfer function of  $\rho_0 \frac{\partial}{\partial t} \nu_n(t)$ .

It worth noting that the radiation from the transducer is affected by the baffle type where the transducer is embedded. In fact, the two other assumptions of free space ( $Z_{trans} = Z_{baffle}$ ) and soft baffle ( $Z_{trans} \gg Z_{baffle}$ ) might be more adopted to the real case scenarios [31], specifically

---

1.  $Z$  denotes the acoustic impedance

the pressure release soft baffle such a polymer is employed. Thence the SIR must be extended to a more general case, where the boundary condition effect is incorporated, in order to have a realistic model [50] :

$$h^{SIR}(\vec{r}, t) = \int_{\Omega_R} \frac{\delta(t - |\vec{r} - \vec{r}_0|/\nu)}{2\pi |\vec{r} - \vec{r}_0|} \Psi(\alpha) d\Omega_R \quad (3.10)$$

with the directional dependent coefficient or obliquity term  $\Psi(\alpha)$  ;

$$\Psi(\alpha) = \begin{cases} \frac{1}{2} [1 - \cos(\alpha)] & \text{free space} \\ \cos(\alpha) & \text{soft baffle} \\ 1 & \text{rigid baffle} \end{cases}$$

where  $\alpha$  is the angle between the normal vector and  $\vec{r}_0$ .

### 3.3 Numerical solutions for transducers impulse response

As indicated earlier, the emission, scattering and reception events in linear loss less acoustics can be determined by solving IR equation. According to the *Huygen's* principle, averaging the spherical wave over the surface of the aperture will yield the solution to the impulse response integral. However, the evaluation of the integral remains nontrivial and requires elaboration toward the aperture geometries. The impulse response approach facilitates the estimation of acoustic field behavior, for any planar aperture with arbitrary geometry, as long as the aperture outlines are definable either analytically or numerically.

There exist the exact analytical solution to the SIR integral but only for a few simple geometries such as planar rectangular [99, 138, 158] , planar circular [146], strip concave spherical shell [42] and concave cylindrical [151]. Assuming that the outlines of the aperture is definable with few parameters, the analytically solution is rather simple. However, as the number of intersection increases, more discontinuities will be introduced. To cope with, superposition of subdivided region's field has been practiced [99, 146].

In order to raise the capacity of SIR approach in estimation of arbitrary geometries (yet planar), numerical implementation have been developed. By the means of discrete representation of the Rayleigh integral or the trigonometric functions defined in polar coordinates [75, 25], it is possible to address the arbitrary geometry, without far-field approximation.

#### 3.3.1 Numerical solution for subdiced planar aperture

The method used through out this thesis is based on the arc approach in which the aperture outline defining angles are sorted in favor of geometrical structure of the vibrating surface. Due to reciprocity of the acoustic wave propagation [82], it is easier to formulate the projection of the incoming spherical wave with radius  $r$  over the plane coincide with the aperture outlines. Then by averaging the cutting arcs ( $\Theta_i$ ) within aperture outlines ( $d_i$ ), IR can be retrieved. Consequently, for any point in the volume, the true nature of field can be retrieved by SIR such that :

$$h^{SIR}(\vec{r}, t) = \int_{\Theta_1}^{\Theta_2} \int_{d_1}^{d_2} \frac{\delta(t - R/\nu)}{2\pi R} \Psi(\alpha) r dr d\Theta, \quad (3.11)$$

where  $R$  is the distance between the aperture and the source. By assuming rigid baffle for the sake of simplicity we have :

$$\begin{aligned} R &= \sqrt{z^2 + r^2}; \\ \frac{dR}{dr} &= \frac{2r}{2(z^2 + r^2)} \implies 2RdR = 2rdr; \\ \therefore h^{SIR}(\vec{r}, t) &= \frac{(\Theta_2 - \Theta_1)}{2\pi} \int_z^{\sqrt{z^2 + r^2}} \delta(t - \frac{|R|}{\nu}) dR. \end{aligned} \quad (3.12)$$



For any arbitrary aperture-geometry, knowing that  $R = t'c$  the above equation can be further reduced to :

$$h^{SIR}(\vec{r}, t) = \frac{(\Theta_2 - \Theta_1)}{2\pi} \nu \int_{t_1}^{t_2} \delta(t - t') dt', \quad (3.13)$$

$$= \frac{\nu(\Theta_2 - \Theta_1)}{2\pi},$$

where  $t_1$  and  $t_2$  are respectively the times when the emanated wave is intersected with the aperture and where the intersection is outermost, the angles  $\Theta_1$  and  $\Theta_2$  are angles subtended at the projection of emanated spherical impulsive wave on the surface of the vibrating surface as illustrated by Figure 3.1. For the case of wave with more than one contributing arc, then the SIR will modify

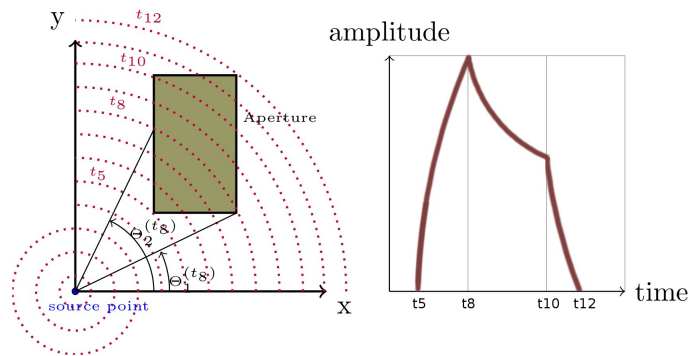


FIGURE 3.1: The response of the rectangular aperture to the spherical wave emanated from a point source. The intersection between the aperture and the circular wavefront projection is defined by the two angles for evaluating the Rayleigh integral.

as the summation of  $N$  contributing arc segments :

$$h^{SIR}(\vec{r}, t) = \frac{\nu}{2\pi} \sum_{i=1}^N [\Theta_2^{(i)} - \Theta_1^{(i)}]. \quad (3.14)$$

For a transducer embedded in rigid baffle, the nature of SIR is entirely defined by these intersections where the arc is located. Therefore the calculation of the SIR can be formulated toward finding the intersections of the aperture outlines with the emanated wave, sorting the angles  $\Theta$  and counting the arc segments meeting the aperture within the time span defined by  $t_1$  and  $t_2$ .

Despite the advantages, yet the outlines might be tricky to deal with. The associated discontinuity with the edges remains obtrusive for this formulation as well, giving rise to a very short response to be sampled correctly for the interaction of rather small aperture with a wave emanated from relative far distance. Additionally, the assumption of uniform vibration over the surface of the aperture might be violated intentionally or inherent to the physics (*i.e.* soft baffle). The cases in point are the focused (positive/negative) elements, aperture embedded in soft baffle, apodization and even capacitive micromachined ultrasonic transducers (CMUT) elements that are demanding for non-uniform membrane vibration simulation.

A proposed solution [124, 123] is based on the spatial-temporal discretization of the integral equation. Basically the aperture is represented by the summation of smaller composing sub-apertures with each weighted and phased accordingly, with respect to the application of concern. The integral equation of (3.11) can be modified to incorporate the weighting/delaying parameter by extending the obliquity term ( $\Psi$ ) to a more comprehensive factor ( $W$ ),

$$h^{SIR}(\vec{r}, t) = \int_{\Theta_1}^{\Theta_2} \int_{d_1}^{d_2} W(r, \Theta) \frac{\delta(t - R/\nu)}{2\pi R} r dr d\Theta \quad (3.15)$$

Solving as before turn the application of  $W$  into the convolution integral with a delta function

that yields

$$\begin{aligned}
 h^{SIR}(\vec{r}, t) &= \frac{\nu}{2\pi} \int_{\Theta_1}^{\Theta_2} \int_{t_1}^{t_2} W(t', \Theta) \delta(t - t') dt' d\Theta; \\
 &= \frac{\nu}{2\pi} \int_{\Theta_1}^{\Theta_2} W(t, \Theta)
 \end{aligned}
 \tag{3.16}$$

Now if the aperture surface is virtually divided into a set  $L$  sub-apertures,

$$h^{SIR}(\vec{r}, t) = \frac{\nu}{2\pi} \sum_{l=0}^L W^l[\Theta_2^{(l)} - \Theta_1^{(l)}].
 \tag{3.17}$$

Indeed, the accuracy of the method is depending on the size of the sampling rate. One should note that the oversampling introduced noise is being simply filtered by the frequency response of the aperture and therefore can be ignored. To solve for  $\Theta$ , the sub-apertures can be approximated by set of boundary lines making a polygon toward the geometry of its original shape [75]. The numerical calculation. The arc projections are found for every temporal sample as it is shown in Figure 3.1 and accordingly if the projection is intersecting with the lines, then the segment of the arc projected on aperture is added to the sum.

For every given voxel in a discrete medium, the SIR of the transducer can be calculated. Depending on the location of the voxel, the SIR and consequently the received pressure signal is altered correspondingly. Figure 3.2 illustrates the SIR subsection to the voxel's location. The SIR of a planar rectangular aperture/transducer is calculate for four voxels in the medium and is depicted individually. for the sake of visualization, the initial time is not considered. The growth in SIR to the saturation point is shorter for the voxels in front of the transducer but the long tail due to the longer width of active surface area. The latter is short instead, for the voxels further away as the relative distance is shrinking, thus faster decay is expected.

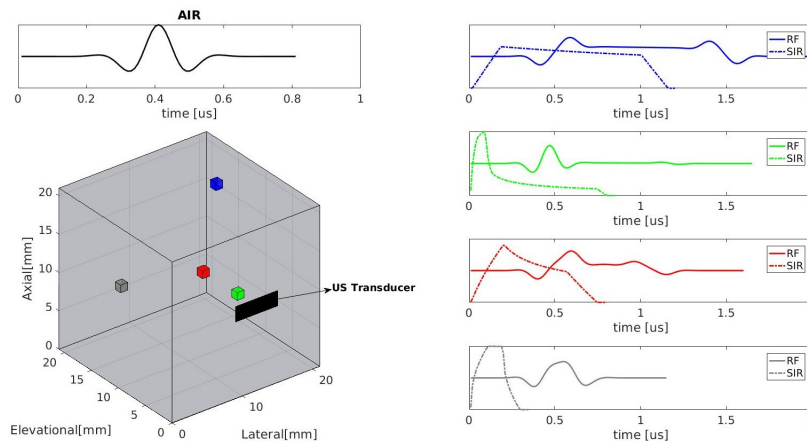


FIGURE 3.2: The calculated SIRs and received signals for 4 points/voxels in the 3D volume, *w.r.t.* the planar rectangular aperture. The SIR's voxel location dependency and the introduced distortion on the received signal is illustrated. The applied excitation pulse is of delta shape in order to make the transmit and receive events akin.

### 3.4 Discrete-domain model based on Impulse Response

Until here, an adequately reliable estimation of the ultrasonic transducer behavior in transmitting or receiving the acoustic wave using IR method has been obtained. Yet, an imaging system is composed of multiple elements (or one scanning element), known as array of transducers, which allows to focus the wave inside the medium and perform the imaging. In order to mimic the focusing effect, characterize the imaging performance of such a system and to show case its potent in true estimation of the medium properties, it is necessary to develop a model that counts for the wave propagation to/from any point in the medium and thereby explain the focusing. In order to make the model realistic, it is critical to take the spatio-spectral properties of the transducer and other related phenomenon into account.

Hence, the model is not only critical for performance characterization but design of the array/imaging system and further task optimization. Aside from the performance assessment which will be discussed in chapter 4, such a model has dramatic impacts on the quality of final image, if employed in the framework of image reconstructing. By obtaining a reliable model, it is indeed possible to relax the restriction imposed by the conventional algorithm based on analytical solution. Chapter 5 is specified to this subject.

Our intention in this section is to develop a mathematical model of underlying macroscopic physical phenomena of acoustic wave interactions, based on the IR method, for every point within the field of view of the imaging system. The nonlinear wave propagation and multiple scattering are ignored, on account of directness rather than ease. Further, assuming that no prior information is available from the media, the shadowing effect induced by highly reflective object, absorption loss, multiple reflection and speed of sound mismatches are neglected, yet they can be integrated toward the specified task. If available for OA imaging, the model can also include the propagation of exciting photon as an adaptive weighting factor on account of light absorption of transient intensity. A good discussion on this subject can be found in [105].

A linear discrete forward model for an idealized discrete-time linear shift-variant system is derived by modeling a spherical acoustic wave generated by a point source. The medium within FOV is considered as a discrete three dimension grid structure, with each voxel accommodating a source point. It can be assumed that the sources are uncorrelated bipoles (OA) or monopoles (US), arranged equidistantly apart in a lattice structure with inter-spacing of at least diffraction limit.

Using the Rayleigh integral, we can cast the point source as an aperture smaller than the wavelength of the migrating wave  $\lambda$  [176, 89].

$$\begin{aligned} S_k(r^s, t) &= \int_V A(r) \frac{\partial}{\partial t} \frac{\delta(t - |r^s - r^n|/\nu)}{4\pi |r^s - r^n|} dr^s, \\ &= A(r) \frac{\delta(t - |r^s - r^n|/\nu)}{4\pi |r^s - r^n|}, \end{aligned} \quad (3.18)$$

where  $(r^s - r^n)$  represents the distance between the detector and source.  $A(r)$  is a non-negative bounded and compactly supported function, incorporating the elementary surface of the  $S_k(r^s, t)$ . Generally,  $A(r)$  is a signal in the form of a delta function. The elementary surface or cross-sectional area of the source is the property of the investigating object but the insonification angle as well. Depending on FOV and the way the sources are being induced in the object,  $S(r)$  can be expresses as,

$$S(r) = \begin{cases} A(r) & \text{for } r \in \text{FOV} \\ 0 & \text{otherwise} \end{cases}$$

From equation 3.9 we know that the recorded pressure in linear system can be approximated by the convolution of three terms : AIR, SIR and the excitation signal. Along with AIR, SIR stands for the spatial variant low pass filter in a linear shift invariant system, otherwise known as transfer function relating the pressure wave of the  $k^{th}$  source  $S_k$  to the recorded pressure  $Y^{rec}$  of

the  $n^{th}$  element of the array.

$$Y_n^{rec}(r, t) = \sum_{r \in FOV} h_n^{AIR}(t) * h_n^{SIR}(r, t) * S_k(r^s - r^n),$$

$$h_n^{IR} = h_n^{AIR}(t) * h_n^{SIR}(r^s - r^n, t),$$
(3.19)

where the impulse response  $h_n^{IR}$  has been sampled temporally and discretized to be consist of  $L$  finite samples.

Expanding the formula for every discretized point in the medium within the aperture field of view yields to a time-discrete matrix representation of the above formula.

$$Y_n^{rec} = M \cdot S_k^{x,y,z}.$$
(3.20)

Similarly FOV can be discretized in Cartesian coordinates, in order to represent the target volume in a grid meshwork of  $X, Y, Z$  mesh or pixels.

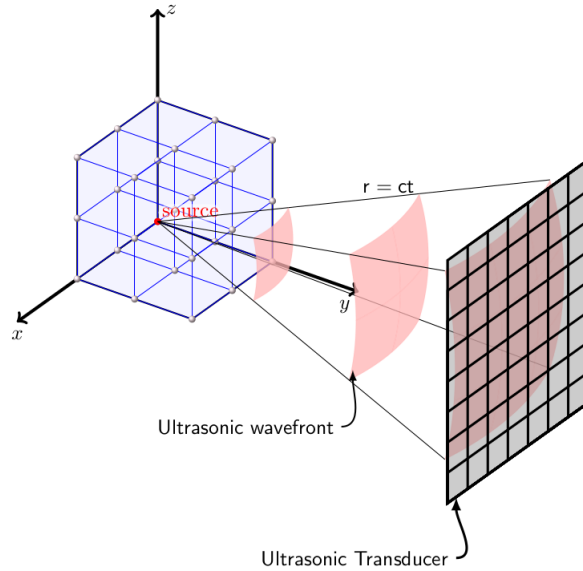


FIGURE 3.3: Depiction of the emanating wave from a source (shown by red) in the discretized FOV (blue lattice) and its intersection with the surface of ultrasonic transducer. Only the portion of spherical wave that is intersecting with the active area of transducer is presented. The rest of spherical wave is not being sensed by the transducer and that, the finite size of the aperture introduces a low pass filter with cutoff in the angular frequencies to the source wave.

Figure 3.3 illustrates the spherical acoustic wave irradiated from a source in the discretized FOV, containing a set  $K$  sources in the FOV, to the array of  $N$  transducers placed on the sensor place. Each transducer is capable of recording the incident pressure wave emanated by any of the sources in the medium. The received signal is the response of the transducer to an ensemble of incident signals from set of excited sources. We use the vector representation for the point sources signals for all sources as  $S_k^{x,y,z} = [S_1, S_2, \dots, S_K]^T$ . Similarly, the recorded signals from any source located at within the FOV by the array can be represented in the vector format as  $Y_n^{rec} = [Y_1, Y_2, \dots, Y_N]^T$ . Knowing the transfer function, it is actually the discrete matrix model  $M_{J \times K}$  (also known as the transfer function and imaging operator) that describes the response of the transducers to a set of control points acting in the FOV as point sources in the object and

vice-versa :

$$M = \begin{bmatrix} h_{(1,1)}^{IR} & h_{(1,2)}^{IR} & \cdots & h_{(1,N)}^{IR} \\ h_{(2,1)}^{IR} & h_{(2,2)}^{IR} & & h_{(2,N)}^{IR} \\ & \vdots & \ddots & \vdots \\ h_{(K,1)}^{IR} & h_{(K,2)}^{IR} & \cdots & h_{(K,N)}^{IR} \end{bmatrix} \quad (3.21)$$

The  $J \times N$  model matrix exemplifies the aperture properties with each column containing the  $N$  time-sampled spatio-acousto-electrical impulse of size  $L$  for each receiving element to the source at the pixel  $k$ ,  $1 \leq k \leq K$ . Let  $N$  denotes the number of sensors, then the final matrix is containing the response of all sensors, being vertically concatenated such that  $J = K \times L$ . The vector representation of the equation (3.20), in an lexicographical showcases the matrix convolution transform, with  $M$  as the imaging operator (kernel) for the reconstruction. On the other hand  $M$  is the transfer matrix containing valuable information about the designed imaging system, discussed in Chapter 4.

## 3.5 IR model matrix otherwise interpretation

Given a linear imaging system, the spatial impulse response of the system is often treated as the kernel or point spread function (PSF), allowing to realize the anisotropic degradation in spatial and angular frequency response of the system. Meanwhile, it is possible to identify the effective geometrical parameters associated with the ultrasonic field and in particular, ability of focusing and spatial sensitivity. However the physical interpretation of IR is not limited here. The IR provides a fruitful model with invaluable information *w.r.t.* the system characterization. In this section we briefly mention those which we find useful in the reconstruction algorithm.

### 3.5.1 Transient field

In the conventional pulse echo ultrasound, it is crucial to simulate the transient field as well as sensitivity field of the aperture. Due to the acoustic reciprocity theorem, the two are highly analogous. Depending on the geometrical parameters of individual transducer, the spectral operation and consequently the bandwidth of the transducer is highly spatial dependent. This property is also known as directive response, as mentioned in Chapter 2. For example, for a sensor of  $\lambda/2$  size, the response is approximately omnidirectional. For an unfocused planar transducer, owing to the diffraction nature of the wave, the near field extends and consequently angular response becomes narrower with the active surface area. With the help of acoustic lens, or spherical curvature, the wavefronts, which can be considered as semi-plane wave as long as they are in the near field, are refracted to the focal point and compromise a diffraction pattern defined by Fraunhofer diffraction [60]. In receive also, the emitted wave from the source can be regarded as a set of emitted plane wave, which can be partially collected by a sensor. The focused sensors collect or emit more of these semi-plane waves in compare to the unfocused array, as long as the object of interest is accommodated in the focal point, yet the sensitivity drops dramatically, for the out of plane areas. The number of required semi-plane wave,  $N_p$ , to define the monochromatic field in the near field, has a been approximated by Fresnel such that :

$$N_p = \frac{2\delta}{\lambda} \tan^{-1} \left( \frac{D}{2F} \right),$$

where  $D$  and  $F$  are respectively the diameter (or length) and focal point of the transducer, and  $\delta$  the diffraction limited focal point lateral width. On the other hand the negative focused transducer (convex) are considering a virtual focusing point behind the transducer, therefore expanding the

angular vision of the sensor, albeit at the cost of lesser averaging surface for the incoming/emitting semi-plane wave and therefore lesser transducing efficiency. Using IR, the transient pressure field which is similar to the receive, can be visualize. Figure 3.4 is showing the transient pressure field of the four cases calculated using spatial impulse response method.

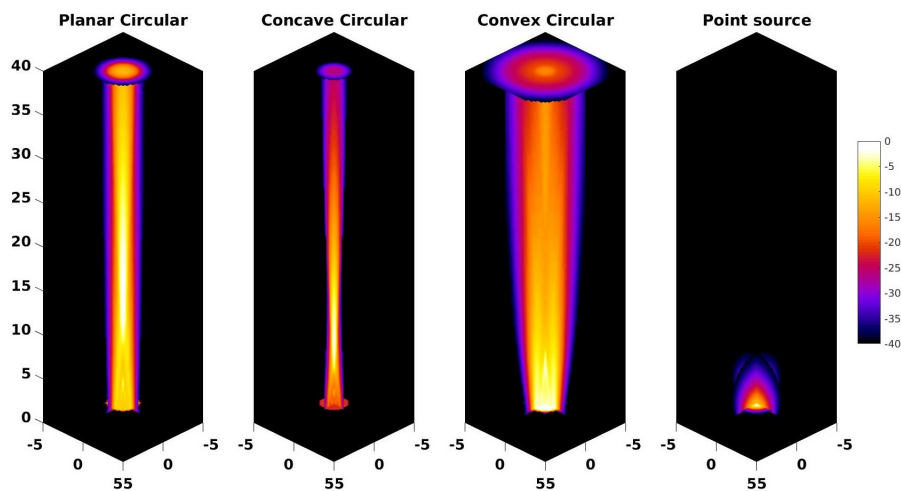


FIGURE 3.4: Logarithmic scale of the calculated transient pressure on the x-z plane for transducers with different geometry, from left to right, planar circular, positively focused concave circular (focal point set at 15mm), negatively focused convex circular, (focal point at -15mm) and point source. The transducer central frequency is set at 5MHz with 60% fractional bandwidth. The diameter of circular transducer is 12 mm. The contour shows the -6 dB *w.r.t.* the maximum pressure generate at the surface of the transducer, to mark the location where the field strength remain 50% of its maximum value.

The excitation pulse is set to delta in order to keep the transient field analogous to the sensitivity field. However, if the interest is on calculation of the exact sensitivity field, the contribution of each pixel must be explicitly assigned and attributed solely to that pixel. The voxel crosstalk matrix approach in chapter 4 section 4.2.1 will discuss how to obtain such a field in detail. Yet, this approach is useful in order to correct for the energy propagation and has a significant effect as an adaptive weighting factor [78] in delay-and-sum based algorithms.

### 3.5.2 Weighting factor

The system impulse response can be also employed as the weighting factor, for correction of the energy, in particular for reconstruction algorithms based on the analytical solutions. This is the case for back-projection algorithm and its correspondent pulse-echo ultrasound imaging, synthetic aperture focusing technique. The principle of these algorithms is already discussed in chapter 2. Briefly, it is based on the assumption that the neighboring sensors are sharing part of the volume within their angular vision, and for those regions, the focusing is possible by phasing and overlapping the received signal, follows by backprojection to reconstruct the point. Moreover, it is possible to treat the focused point as a virtual source, and by further post-processing, increase the depth of imaging [46, 91] and correct for the smearing effect due to overlapping the signals. There have been developed variety of adaptive weighting factors in order to improve the focused regions and out of focus smearing. Generally, they weight the signal or the reconstructed projections by the spatially adaptive factor of the size of the image/signal. Therefore, for every point the image is being weighted *w.r.t.* the coherency between the compounded pixels (or summed signals). Yet, for the out of focus regions closer to the sensor, where the pixel is confined to few or even one element projection, this weighting factor is ineffective. The situation is visualized by Figure 3.5, in which the possibility of focusing (beam forming) for the points in the far field (*i.e.* green) is illustrated. Localization of the points in the near field (*i.e.* blue) is blurred to the wavefront line (corresponding to the delay) as they are restricted to only one transducer.

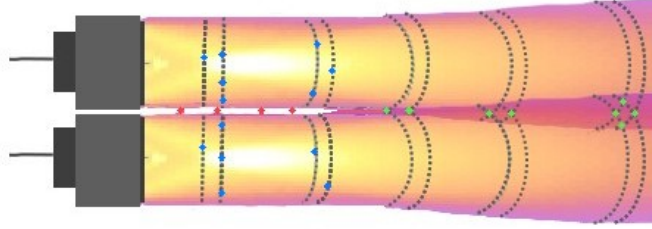


FIGURE 3.5: The schematic of the view angle of two staring transducer (width  $\gg \lambda$ ). The flat lines are indicating the near field where the waves have not been diffracted (diverged) yet. The points are implying the acoustic sources, in three colors indicating their visibility on the corresponding wave-fronts (lines) where the array may or may not localized them based on their location.

As stated in the previous section, the near field expands with the size of the aperture. The larger element also means higher averaging over the surface of the transducer, which despite the imposed diffraction, it is useful where the SNR is low, such as the case for optoacoustic or SAFT based total focusing pulse echo. The inherent advantage of spatial impulse response as a weighting factor is more vivid for these areas, where the response of every point is calculable, regardless of the location of the point. From previous sections, we know that SIR can explain the modulation in the strength and shape of the received signals. In the other words, it is possible to model the imposed cutoff frequency on both the spatial (angular) and temporal (averaging) frequency of the acoustic wave. In their work, Turner *et al.* employed an adaptive weighting map based on SIR in virtual source SAFT. Their weighting factor adaptively takes into account the overall contribution of SIR for the incoming signal [157]. Alternatively it is also possible to weight the analytically solution by looking into the spectrum of each pixel-element SIR and weighting the signal accordingly, based on its frequency compartment. Hence, the reconstruction algorithm counts for the spatial-spectral discrepancies introduced by the size and shape of the element to the recorded signals and further, the associated and to be compounded projections [78]. The latter is rather more adaptive, and the weighting accommodates toward the relative transfer function (SIR). In chapter 5 section( 5.3.1), this method will be discussed in details.

### 3.5.3 The aperture limited view

In order to focus the ultrasonic wave using phase array or retrieve a point source, the simple trick is to modify the phase and amplitude of individual element's (transceiver) signal in a way to compensate for the distortion caused by the linear time invariant system. The introduced distortion is better understood by excavating the information contained in the model matrix. As represented by figure 3.3, in the reflective or back-ward mode of imaging, the system is only able to partially recover the spherical wave. The finite size of the aperture is acting as a low pass filter in the angular frequency of the incoming wave, results in a diffraction limited resolution.

The loss of information due to the limited aperture, indeed is integrated in the IR matrix, along with the averaging over the surface of transducer, explained earlier. It is known that each component of the Fourier transform of the impulse responses, is the transfer function associated with that component, estimating the spatio-temporal filter in the angular frequency. In fact, the transfer matrix contains the transfer functions between the aperture to the object points or sources. If the source/object plane be parallel and co-aligned with the imaging plane (where the traducers are located), the number of angular frequency can be associated with the number of plane wave. Basically the spherical wave can be decomposed to a set of plane wave; each with a particular angular frequency  $\omega$  and wave number  $\kappa$ . In this very case  $\omega$  and  $\kappa$  are replaceable via  $\kappa = 2\pi/\lambda \simeq \omega/\nu$ . If we express equation 3.5 in frequency domain, for a given point in 3D space in Cartesian coordinate, we can expand it to *Weyl's* integral [169] such that ;

$$G^F(x, y, z, \omega) = \frac{e^{i\kappa\sqrt{x^2+y^2+z^2}}}{4\pi\sqrt{x^2+y^2+z^2}}$$

Assuming homogeneity by ignoring the evanescence waves ( $\kappa_z = \sqrt{\kappa^2 - \kappa_x^2 - \kappa_y^2}$ );

$$G^F(x, y, z, \omega) = \frac{i}{2(2\pi)^2} \int_{-\infty}^{\infty} \int_{-\infty}^{\infty} \frac{e^{i|z|\sqrt{\kappa^2 - \kappa_x^2 - \kappa_y^2}}}{\sqrt{\kappa^2 - \kappa_x^2 - \kappa_y^2}} e^{i(\kappa_x \cdot x + \kappa_y \cdot y)} d\kappa_x d\kappa_y \quad (3.22)$$

The physical interpretation of *Weyl's* integral is nothing but representation of decomposed spherical wave as a set of plane waves angular spectrum.

This a very important property to express how many plane waves or degree of freedom we can achieve with the aperture in hand for a given point, in order to focus the acoustic wave or define the wave emitted from the point as depicted by Figure 3.6.

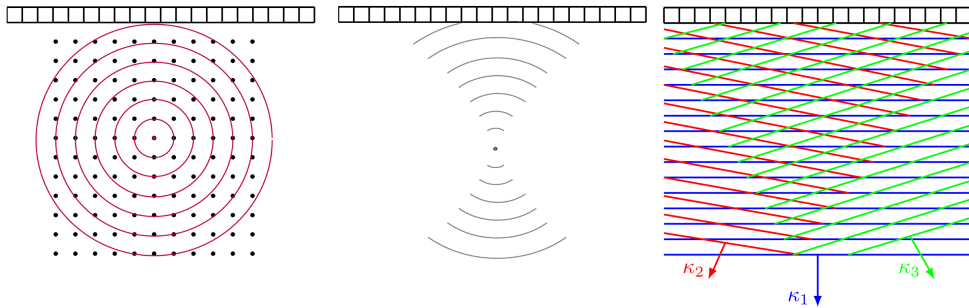


FIGURE 3.6: Schematic diagram for visualization of linear array limited view angle. Left : a point source in the medium emitting spherical wave; middle : the ability of the linear array to back-propagate the received angular frequency in order to focus on the point by time inversion of the array signals; and right : generated angular frequency by the array to mimic the spherical wave as a set of decomposed plane waves. The schematic shows the spatial variance of the array in recovering/receiving the angular frequency of the source from the medium

Additionally, the limited aperture has been a consideration point to assign the limit in sensibility of the aperture to the angle incoming plane wave. This is highly depending on the relative orientation between detection and source plane that discussed in the reference [127]. Figure 3.7 represents this reciprocity between a linear array and a needle like structure, with different orientation (left). The reconstructed data (left) only manage to reproduce part of the structure for which, the emanated wave has been detected by the the array. As the tilting angle is increasing toward the normal degree, the ability is gradually lost. We explain how we can exploit these information by eigen analysis of the transfer matrix, in chapter 4 section 4.2.2.

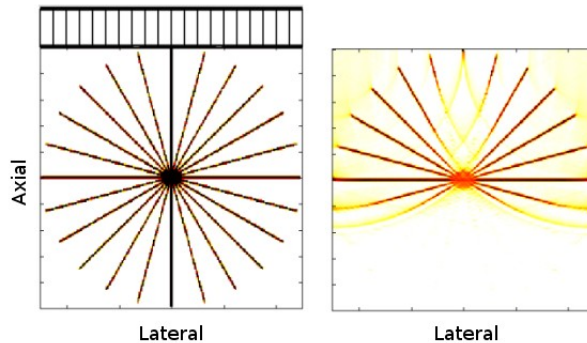


FIGURE 3.7: The angular sensitivity of linear array to the incoming wave from the object with different relative orientation. Left : The original optoacoustic spike-like object, with each is emitting an isotropic semi-plane wave with specific angular frequency; Right : the reconstructed image. For both simulation and reconstruction, k-wave toolbox has been employed [155]



## 3.6 Conclusion

In this chapter, a discrete model has been developed for acoustic calculations in interacting acoustic wave with the OPUS imaging system composed of tranceiving elements. The calculation is based on the system impulse response that relates the source to the recorded signal by the convolution between the source strength and the transfer function of the medium, therefore the ability of aperture in focusing and retrieving the physical properties of the medium is reproducible. Within the framework of this method, the model that describes the imaging performance of any imaging system can be developed. The method has been implemented in matlab software to showcase its potentials in accurately defining the wave propagation in the loss less medium and its interaction with both the detecting and emitting aperture, in order to estimate the transient or sensitivity field. I presented the derivation of the model for the linear time invariant system of imaging. Multiple effects, describing the wave generation, propagation and reception events, required for designing an imaging system is incorporated in the model. This includes the spatio-temporal low pass filtering for individual transducer in the array due to the finite size of the element and the angular low pass filtering due to the limited angle of view of the overall aperture. The model can be adopted to the the prior knowledge of the transducer and more generally aperture behavior in transmitting and receiving the wave into the discretized loss less medium.

Using this model, I can study and assess the performance of the OPUS imaging system and extract information regarding the spatial sensitivity field, achievable spectral information and the ability of the imaging system in resolving the sources in the medium (discrete points). These properties will be discussed in details in the next chapter for geometrical designing of the array. Furthermore, as the model contains the system behavior information, as an estimator can be used for the reconstruction in order to increase the accuracy of the output OPUS images. The process is also known as deconvolution and will be discussed in chapter 5.



# CHAPITRE 4

---

## Design and characterization of the OPUS handheld probe

---

The grand aim of all science is to cover the greatest number of empirical facts by logical deduction from the smallest number of hypothesis and axioms.

---

Albert Einstein

### Abstract

Hybridizing optoacoustic and ultrasound imaging comes with the promises of delivering the complementary morphological, functional and metabolic information of the tissue. The present chapter is exploring the optimal geometrical properties for a handheld probe for volumetric OPUS imaging, being capable of addressing the requirements of both imaging systems. In order to find the optimal parameters and further assess and optimize the performance characteristics of both imaging systems, series of evaluations studies and analysis in the context of pre-reconstruction model (*i.e.* transfer matrix) were carried out. The evaluation took place by means of voxel crosstalk analysis and eigenanalysis, revealing information about the spatial sensitivity, aliasing and ability of focusing on specific target. Based on these benchmarks, the optimum design parameters of the transducer is proposed in terms of number and size of the elements, arrangement and aperture dimension. We believe that our design facilitates the transformation from bench to bedside with great capacities for clinical imaging.

## 4.1 Introduction

**T**HE first and foremost objective of any imaging system is to acquire the localized information about the physical properties of the investigating medium. In medical imaging, the captured data are needed to be inferred to as a set of anatomical and/or physiological meanings about the tissue or its components. Assessing the fidelity, efficiency and the overall performance of the imaging system in capturing and localizing the "quanta" is a milestone in the design of imaging system.

Given the increasing role of OPUS imaging in molecular interrogation for clinical and preclinical studies, there have been significant efforts and advances in the design and development of this hybrid imaging system. On the practical basis, majority of the designed systems are optimized toward performing a specified task. Such is the case for transvaginal probe [87], rectal probe [15, 38], intravascular probes [72, 86, 28] and mammographic systems [174, 40, 85]. The benefits of

hybridizing these two modalities are becoming more evident where the functional information is required to be localized on the basis of anatomical structure.

For a single purpose probe with specified task, the system performance can directly assessed and optimized simply via task-related metrics. In that case, a consequential assessment correlates the performance of an imaging system with the given tasks for which the system was intended on. For example, it is possible to increase the sensitivity of OA imaging by optimizing the light delivery systems. This is the case for minimally invasive procedures where the interstitial illumination light delivery [86, 38] is an option. Also, if the sample can be enclosed by detectors and exposed by multiple directions, as is the case for breast, the number of projections with moderately larger elements [40, 85] are two parameters enhancing the performance. By contrast, multi-purpose portable imaging systems are limited to the task based optimization, since optimization for specific task might not be persuasive to others. To begin with, maximizing the projection angle is limited to the ease of tissue access and optimizing the illumination is highly biased procedure toward the assigned task, aside from being minimally invasive.

The early attempts took place by integrating the light delivery system such as optical fibers with the commercially available standard US transducers. This trend is being practiced on 2D images using linear array transducers, mainly due to their availability, low cost and moderately simple assembly requirements. Replicating this fashion for the 3D imaging with the two dimensional matrix arrays is demanding and nontrivial. It is needless to say that in volumetric imaging, providing a high resolution window into the anatomical and physiological properties of the investigating tissue is closely bounded to the probe characteristics and its ability to extract the information.

In OPUS imaging, distinctive features of the tissue, including location, size, shape, and physiological activities are encoded in the pressure waves, either optically via photoacoustic effect or as a measure of reflectivity to the emanated pressure wave (pulse-echo). In that sense the goal of OPUS imaging system is two fold ;

1. Optimize the radiation field in order to stimulate the interaction between the transmitted wave (optical or ultrasonic) and object within the window of the volume of interest (VOI), hence generating virtual sources,
2. Estimate the distribution of the sources by detecting the emanated wave from the induced virtual sources at the surface of the medium.

The first task is associated with differences exist in the perspective of the two modalities, mainly due to the nature of irradiating wave. In general, there are more degrees of freedom for ultrasonic transmission, as the speed of sound and degree of coherency of the acoustic waves accede the electronic beamforming for focusing or steering purposes, even-though with imposing certain constraint in the array geometry. The ability of multiplying the transmission event of course is accompanied with higher resolution and signal-to-noise ratio (SNR), owing to the increase in number of projections and angle of view. On the other hand, in OA imaging, source generation is fundamentally a different process. Optically absorbing moieties are translating the absorbed photon into broadband acoustic pulses. As the speed of light is 6 order of magnitude higher than speed of sound in soft tissues, the generation of acoustic waves by the induced sources can be considered as a simultaneous event that happens upon the laser pulse incident. In terms of number of obtained projections, it is analogous to flash mode of imaging for pulse echo ultrasound, where all the elements are derived at the same time with no phase delay. Hence the quality of the final image is limited to the number of projections provided by each receiving elements.

In the pursue of analogy, OA has another limitation which emerges from the interaction of optical wave with biological tissue. The optical photons are subjected to decoherence over the course of propagation beyond microscopic level, which gives rise to high attenuation. Despite the efforts in wave-front shaping [27], controlling the light or even explaining the behavior of photons migration in biological tissue in diffusive regime remained challenging. However, transition of light from ballistic to diffusive regime by virtue of multiple scattering events brings about the optical coverage for the entire VOI, which is optimally equal to the FOV of the receive aperture. Indeed, as long as the scattered photons are being absorbed, they contribute to the optically induced

acoustic wave. Yet, scattering limits the penetration depth, and leaves the deeper moieties with much lesser photons, hence lower SNR.

The effective penetration of the light is the function of optical properties of the tissue, pulse repetition rate, radiant energy, beam diameter and illumination angle, out of which the last three are modifiable but the compromise is constraint to the maximum permissible exposure (MPE) provided by the American National Standard Institute (ANSI) safety standard [1]. Deep light deliver requires high energy, yet by expanding the light beam diameter, the optical fluence will increase [81]. Moreover, it is known that perpendicular illumination minimizes the reflection from skin and shortens the optical path to the absorber. Another challenge yet might be the arising clutters caused by high fluence of the superficial tissue at the irradiation site. If coincides with the transducer view angle, it will obscure the weak signal from the deeper structure and lowers the contrast to background [71].

Granted the optimum radiation, the ability of the system to detect and resolve the induced virtual sources is defining the signal fidelity which is addressing the second task. Indeed the fidelity of the OA reconstructed data is highly subjected to the properties of the detector. In fact, due to the nature of photoacoustic effect, the accuracy of the reconstruction algorithms is only ensured when the full view angle is provided by the detection aperture [117]. Unless explicitly accounted for, in the back-ward epi-illumination OA imaging systems, finite aperture and detection view angle of less than  $2\pi$  alters the reconstructed features and result in an inaccurate estimation [117]. Similarly in US imaging, providing high resolution images is closely bounded to the aperture characteristics. For example, an aperture as large as  $60\lambda$  is required to provide  $1^\circ$  of spatial resolution[102]. When the large aperture is desired, the mainstream approach is to find a compromise between the element size and number of channels. The elements are representing stronger directional response with increasing the size and thus narrow the spatiotemporal frequency response. Additionally, averaging and diffraction over the active area of the element distorts the frequency contents of the collected signal. The conventional US arrays are demanding for  $\lambda/2$  inter-element spacing to avoid grating lobes. This leads to high number of elements and consequently high channel counts. To address this compromise, variety of undersampling strategies have been pursued [11, 98, 179, 79] among them the unconventional geometries [26, 102, 131] are benefiting from the  $60\lambda$  effective aperture size with lesser but larger elements. This is possible thanks to the lower periodicity of the sparse geometry which relaxes the aforementioned restrictions. This concept prompt further investigation.

The objective of this chapter is to extend this concept and investigating the annular geometry for multipurpose backward epi-optoacoustic and ultrasonic pulse echo imaging techniques. The proposed ultrasonic transceiving probe has the advantage of mitigating the number of channels requires for 3D US imaging while preserving the spatial resolution. What is more, the inherent central cavity of the probe furnishes the in-line illumination arrangement. The latter prepare the expedient agreement between fluence and blind folding the clutter [61] via minimizing the overlapped region between the optical fluence at irradiation side and elements view angle. In designing a bimodal imaging system, finding the number, size and geometrical distribution of the elements is a tricky task.

In chapter 3, the mathematical description for the model matrix has been represented along with the brief introduction about the system quality characterization by interrogating the model. In this chapter, a systematic evaluation approach is being followed in order to heed the aforementioned challenge in geometrical design and optimization of the bimodal handheld probe. The design characteristics for the aperture in terms of overall performance, ability of focusing, spatiotemporal frequency response and aliasing will be examined using the transducer model crosstalk matrix [136] and eigenanalysis. The objective assessment of the design is followed by the system optimization with regards to the number, size and geometry of the transducer. Further, the imaging performance of the imaging system and its capabilities of estimating the original data is discussed in chapter 5 using quantification metrics.

## 4.2 Pre-reconstruction generic assessment

In designing the imaging system, it is indeed critical to assess the probe performance. It is advised that the evaluation and optimization criteria be more comprehensive to be subjected to a classified task, and that the design system can perform for range of unforeseen tasks. In order to evaluate the design of an imaging system and proceed with further optimization, a *de facto* protocol standard that provide an insight to the imaging quality of the designed system is critical. For this purpose, the objective assessment of the imaging system based on the point spread function (PSF) [181] and spatial sensitivity [136, 171] has been routinely practiced. PSF is associated with the ensemble of detected acoustic waves emanated from the observation point and its neighboring. Often considered as the system response to a point source, PSF reveals information about the resolution as well as the accompanied streaking artifacts. However, because of the limited view in the backward-OPUS systems, limited set of data is acquired by the aperture which is giving rise to uncertainties in the source estimation. Therefore PSF based characterization is highly biased to the merits of the reconstruction algorithm. Under the assumption that the model matrix  $M$  is non singular, the estimator is asymptotically unbiased and efficient. Therefore one can optimize the parameters toward obtaining a system with minimum variance estimator. However a non-singular full rank matrix for backward mode OPUS is nontrivial to be achieved and even so, nontrivial to verify. Alternatively, PSF can be calculated analytically [146] via a linear model  $M$  based on the spatial impulse response that incorporates the properties of transceivers. For a shift-variant system like OPUS, it is important to determine the source-voxels position within the FOV that can be reliably determined in terms of its standalone contribution and resolvability from the neighboring voxels. As for every voxel in the 3D lattice, there is an attributed function (IR),  $M$  can be treated as the matrix containing voxel basis function. The integration over the spanned basis of each voxel indicates the value of corresponding voxel and is proportional to the integration of sensed acoustic wave over the surface of transducer. Aside from the characterization of reconstructed image, in the literature two evaluation methods have been suggested for the generic assessment of the imaging system, the voxel crosstalk matrix [130, 136, 171] and eigenanalysis [149, 161] to further exploit the imaging operators  $M$ .

### 4.2.1 Voxel Crosstalk matrix

In chapter 3 the mathematical formulation of discrete model matrix  $M$  has been described, assuming that for each voxel in the FOV, the system impulse response can be estimating using the convolution of SIR and AIR. The intuition for crosstalk is to relate the ability of system in detection to the designed configuration parameters. Since the OPUS is dealing with the acoustic waves that are propagating in a diverging manner throughout the medium, estimation of the value for a given voxel is incorporating the uncertainties. These uncertainties are mainly associated with the contribution of other voxels averaged over the surface of the aperture within the same time span, as depicted in Figure 4.1. The voxel crosstalk matrix accounts for this interdependence by providing metrics for quantifying a system capacity to describe precisely which voxel contributes to the received data by the system and whether or not these individual contributions are distinguishable *w.r.t.* each other, giving a measure of intervoxel crosstalk of the design system.

The concept of crosstalk is developed by Barrett *et al.* [13] for Fourier domain but the crosstalk concept can be generalized to any expansion [136]. As a mean of design evaluation, the crosstalk matrix provides metrics for system comparison. If the constituents of each matrix entry are examined, it becomes apparent that the diagonal elements of the crosstalk matrix determine the sensitivity of the imaging system to the corresponding voxel location in object space.

Additional information can be acquired by analyzing the off-diagonal entries in each row of the crosstalk matrix to distinguish among the spatially dependent contributions made by neighboring voxel coefficients, *i.e.* aliasing of information from other voxels into a voxel of interest. The crosstalk concept can be generalized to any expansion function provided the object can be adequately represented.

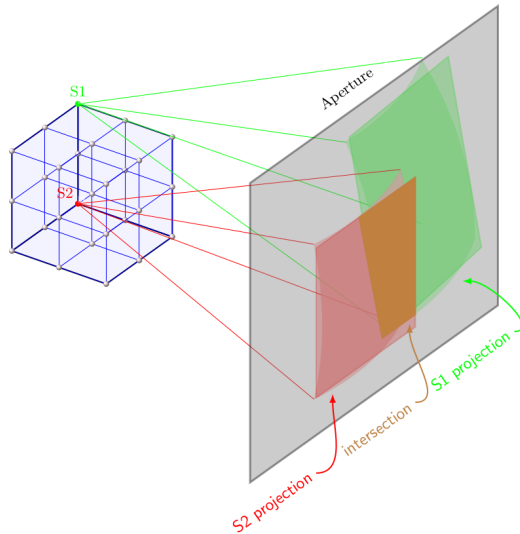


FIGURE 4.1: The projection of emanated waves from two source located in voxels apart over the surface of detecting aperture. The brown region represents the intersection area between the projection of two sources.

The concept of crosstalk has been established in assessment of system design to reveal the interconnection between the expansion function of the imaging system [13]. When the system is shift variant, the basis could be considered as voxel and the speculation occurs over the signal leakage between the adjacent voxels. Hence the effect of aperture in spatial blurring, spatial sensitivity and aliasing is amenable to an analytic description. Voxel crosstalk matrix can be obtained as follow :

$$H = M^T M \quad (4.1)$$

where  $(.)^T$  denote the transpose conjugate.  $M$  can be treated as the calibration matrix, whereas the crosstalk matrix  $H$  describes the aliasing between expansion functions attributed to each voxel.  $H$  is also the covariance matrix of  $M$ , essentially a square matrix with diagonal elements describing how sensitive the system is to the acoustic wave emanated from a specific voxel, thus implying the spatial sensitivity. The off diagonal elements stand for the contribution of neighboring voxels crosstalk *aka.* spatial aliasing. It is worth noting that  $H$  is closely related to the least square estimator and also the time reversal operator [149]. Rigorously, there is a high consistency between the diagonality of matrix  $H$  and the preciseness of the source estimation  $\hat{S}$ .

### Signal fidelity metric

In the signal processing community, there have been many objective metrics proposed for the evaluation of matrix quality, including the signal fidelity metrics that evaluate the distortion in the signal through comparison analysis with a reference signal. It is feasible to extend the concept to the system design [171] for the sake of quantitative analysis of these qualitative measures. By considering the identity matrix as a reference, a fidelity principle for the quality assessment that interrelate the quality of the voxel crosstalk matrix to the reference.

The conventional signal fidelity metrics has been utilized for systematic evaluation of the voxel crosstalk matrix. The utilized figure of merits (FoMs) in this context are the conventional objective quality assessment as follow root mean square error (RMSE) and mean absolute error (MAE) which mainly are based on the average magnitude of error between the distorted voxel and the reference value. These metrics are defined as follow :

$$\text{RMSE} = \frac{1}{n} \sqrt{\sum_{i=1}^n |e_i|^2} \quad (4.2)$$

$$\text{MAE} = \frac{1}{n} \sum_{i=1}^n |e_i| \quad (4.3)$$

where  $e_i$  represents the estimated error of the  $i^{\text{th}}$  pixel.

The difference between RMSE and MAE is the scoring rule which unlike MAE, it is quadratic for RMSE. This means that RMSE has a high penalization for large errors but MAE weights equally, thus conveying information about the degree and amount of error in a model. The benefit of employing them simultaneously in one analysis stems from the fact that these metrics are complementary to each other, providing a robust systematic approach in quantitative analysis of imaging performance [170]. Together they render information about the variation in set of error, with the following condition

$$\begin{cases} \text{RMSE} > \text{MAE} & \text{the variation between errors} \propto |\text{RMSE} - \text{MAE}| \\ \text{RMSE} = \text{MAE} & \text{same errors with same magnitude} \end{cases}$$

On the other hand, one of the mostly used metrics, PSNR (peak signal to noise ratio) is the ratio between maximum possible power of the image and the power of the distorted image.

$$\text{PSNR} = 20 \log_{10} \left( \frac{\text{MAX}_I}{\text{RMSE}} \right) \quad (4.4)$$

where  $\text{MAX}_I$  is the maximum possible pixel value in the image. The higher PSNR can be interpreted as higher quality and lesser errors.

## 4.2.2 Eigenanalysis

As the name implies, eigen-decomposition of a square matrix  $A$  features prominently the characteristics of matrix by delivering basis of eigenvectors  $q$  scaled by scalar eigenvalues  $\lambda$ .

$$\begin{aligned} Aq &= \lambda q \\ \text{assuming that eigenvectors are linearly independent;} \\ \therefore A &= Q\Lambda Q^{-1} \end{aligned}$$

where  $Q$  is the square matrix the projection of  $A$  in the eigenspace, containing eigen-vector  $q_i$ , for each column and  $\Lambda$  is a diagonal matrix with element along the diagonal standing for corresponding eigenvalues  $\lambda_i$ . The eigen-decomposition can be looked as an expansion of the matrix with respect to its basis (*i.e.* eigenvectors), each with weighting coefficient (*i.e.* eigenvalues). Therefore the matrix can be represented simply as weighted combination of basis. The eigenvectors of the operating matrix depict the principal structures of the detected wave component, reserving the original properties of the original matrix. Their frequency distribution have been used to extract the major eigenvectors (spectral) from the minor ones (*e.g.* noise) [149]. In another words, distinguishing the strengths and deficiencies of these systems. The values of  $\lambda$  can be linked to the energy level or stability parameters of the matrix. Often the transfer matrix (or its equivalent time-space domain matrix *i.e.* the model matrix) is not a square matrix or not diagonalizable. This affect the linear independency of eigenvectors thus, the singular value decomposition can be used instead.

### Singular value decomposition

The singular value decomposition (SVD) is similar to eigen-decomposition; knowing that the eigenvalues of the covariance matrix  $A^T A$  are the squared of the singular value of  $A$  and singular



vectors of  $A$  corresponds to eigenvectors of  $A^T A$  for  $A$  a rectangular and not necessarily square matrix [125]. The SVD of matrix  $A$  can be written as;

$$AV = U\Sigma \Rightarrow A = U\Sigma V^T$$

where  $\Sigma$  is a diagonal matrix the same size as  $A$  and is expected to be zero except its diagonal element, denoting the singular values.  $U$  and  $V$  represent the left and right orthonormal singular vectors. Alternatively, columns of  $U$  and  $V$  can be respectively interpreted as the eigenvectors of matrix  $AA^T$  and  $A^T A$ . For matrix  $A_{m \times n}$  with  $m > n$ ,  $U$  is a square matrix of size  $m \times m$  with meaningful eigenvectors along the first  $n$  column;  $\Sigma$  is  $m \times n$  with singular values along the first  $n$  rows and  $V$  a square matrix of size  $n \times n$ , then on can represent the SVD as;

$$A_{m \times n} = \underbrace{\begin{pmatrix} u_{11} & u_{21} & \cdots & \cdots & \cdots & u_{1m} \\ u_{12} & u_{22} & \cdots & \cdots & \cdots & u_{2m} \\ \vdots & \vdots & \ddots & & & \vdots \\ \vdots & \vdots & & \ddots & & \vdots \\ \vdots & \vdots & & & \ddots & \vdots \\ u_{1m} & u_{2m} & \cdots & \cdots & \cdots & u_{mm} \end{pmatrix}}_{U_{m \times m}} \underbrace{\begin{pmatrix} \sigma_1 & 0 & \cdots & 0 \\ 0 & \sigma_2 & \cdots & 0 \\ \vdots & \vdots & \ddots & \vdots \\ 0 & 0 & \cdots & \sigma_n \\ \vdots & \vdots & \ddots & \vdots \\ 0 & 0 & \cdots & 0 \end{pmatrix}}_{\Sigma_{m \times n}} \underbrace{\begin{pmatrix} v_{11} & \cdots & v_{1n} \\ v_{12} & \cdots & v_{2n} \\ \vdots & \ddots & \vdots \\ v_{1n} & \cdots & u_{nn} \end{pmatrix}}_{V_{n \times n}}$$

For the well resolvable sources, the response of the array to the source can be associated with the singular vectors, such that its phase and amplitude are required for the array to define the source (*i.e.* focus in transmit or receive). This property has been shown before by Chambers *et al.* [24] for point like scatterers. Therefore, eigen or singular based analysis provides a simple but credible mechanism for the comparative evaluation between two or more imaging system.

Another noteworthy aspect is the possibility of expressing  $A$  as the combination of its principal components  $E_k$ , such that :

$$A = E_1 + E_2 + \cdots + E_n$$

where  $E_j = \sigma_j u_j v_j^T$

The norm of each component matrix is equivalent to the singular value, expressing the energy or significance of the associated component.

$$\|E_j\| = \sqrt{\lambda_j(A^T A)} = \sigma_j$$

The contribution of  $E_j$  in reproducing  $A$  can be estimated which is subjected to the value of  $\sigma$ . Since the singular values are arranged in descending;  $\sigma_n < \sigma_{n-1} < \cdots < \sigma_2 < \sigma_1$ , one can estimate how many of component matrices are necessary to reproduce the original matrix, hence remove the singularities and remove the dimensionality.

$$A_r = E_1 + E_2 + \cdots + E_r ; \quad r < n$$

$$\|A - A_r\| = \sigma_{r+1} \approx 0$$

## Rank of matrix

This boundary, also referred to as the rank of matrix,  $N$ , happened to be estimated from empirical observation of the frequency distributions of Fourier transformed eigenvectors [135] or the spectrum of the eigenvalues. In principle the eigenvalues provide a measure of fidelity of the components such that the  $i^{th}$  eigenvalue exemplifies the  $i^{th}$  eigenvector significance. In fact the

sum of the eigenvalues or the nuclear norm of the matrix declares the energy of the matrix. Thus the spectrum of eigenvalues which is a generalized form of the Fourier power spectrum, helps us to discriminate between the primary and secondary components (null function).

$$M = M_{prim} + M_{null}, \quad (4.5)$$

where the columns of the data matrix  $M_{prim}$  are highly correlated. The physical meaning of matrix rank  $N$  can be interpreted as the number of resolvable structures and on that account, the diffraction limited resolution achievable by the aperture.  $N$  is similar to the quantity of semi-plane wave  $N_p$  (chapter 3) the aperture can receive or generate, for a given well resolved point in the medium. Furthermore, in order to optimize the reproducing process and removing singularities, specially for the sake of reconstruction, estimating the rank plays a pivotal role. In that, a popular heuristic approach is singular value thresholding (SVT) where the rank of matrix is of close proximity to the nuclear norm of matrix  $\|\cdot\|_*$  as follow :

$$SVT_\kappa(M) = \arg \min \frac{1}{2} \|(M - M_{prim})\|_F^2 + \kappa \text{rank}(M_{prim}) \quad (4.6)$$

where  $\|\cdot\|_F$  is the Frobenius norm and  $\kappa$  denotes a positive scalar. The solution to the equation 4.6 is given either by imposing a hard threshold on the singular values exceeding  $\kappa$  ;

$$SVT_\kappa(M) = \sum_{i=1}^n H(\sigma_i - \kappa) + u_i v_i^* \quad (4.7)$$

with  $H$  being the Heaviside function, or soft thresholding by subtracting the  $\kappa$  to approach zero, denoted by ".+".

$$SVT_\kappa(M) = \sum_{i=1}^n (\sigma_i - \kappa)_+ + u_i v_i^* \quad (4.8)$$

$$SVT_\kappa(M) = \arg \min \frac{1}{2} \|(M - M_{prim})\|_F^2 + \kappa \|M_{prim}\|_* \quad (4.9)$$

Such a problem is nonlinear in compare to the Tikhonov regularization [22] and beyond the scope of this chapter (please consult chapter 5 section 5.2 for further details). However, our approach in this section leans toward the overall perspective of the effective rank. The system with larger effective rank is imputed to the superior focusing competence [149] and more accurate set of acquired data. In a similar fashion, the performance of the system can be analytically evaluated by inspecting the behavior of its eigenspectrum which is also related to the energy and nuclear norm of the system and further evaluation the singular vectors.

## Eigenspectrum

The spectrum of the eigenvalues can be used to evaluate the system performance. Eigenspectrum which is simply depiction of the matrix eigenvalues distribution in ascending or descending order, allows to empirically find the rank and distinguish the main structures and keep only the valuable components, but estimate their fidelity as well. There are two hypothesis associated with eigenspectrum for evaluating the system, the first one is that the system with the larger eigenvalue obtains a superior performance in reproducing the original matrix. In that context, the faster decay in the spectrum is an indication for lower fidelity and consequently poor performance. The other, however, stems from the higher number for the rank, and the value of the main eigenvalues, regardless of the decay type.

## Singular vector analysis

On the other hand there is a hypothesis that emphasizes on the quality of the eigenvectors rather than eigenvalues. As mentioned earlier, the rank of transfer matrix can be estimated from

the Fourier of singular vectors as well. On top of that, these vectors are containing information about the missing projections of angular frequencies for the plane of object parallel to the imaging plane, which is a feature of instrument itself in terms of limited view angle. Subsequently, SVD estimates that the reconstructed image will be missing these angular frequency information, even if OPUS is a perfect backward imaging system (*i.e.* infinite detectors). Therefore, the superior performance is achieved by the system with the stronger singular vectors intrinsic to the most informative object features, even if it contains weaker eigenvalues [17].

For the case where the array and the imaging plane are perpendicular, singular vectors are related to the plane wave decomposition, the angular direction of these plane waves progressively increases as the singular value weight decreases. Due to the spatial symmetries of the configuration,  $H = H'$  thus  $U = Vt$  and each singular wave is transformed into its phase conjugate after propagation from the array to the imaging plan.

The advantage of eigen-decomposition or SVD is the fact that they provide a basis for appraisal analysis between two measurement systems. The singular vectors of a measurement system represent the basic structure of the sensed image component and the singular values provide a measure of how many components are measured and the fidelity of with which can be estimated. For a shift variant system like OPUS, the singular vectors delivered by the SVD are acting as the signal components and the singular values are playing a role of transfer function.

For the case where the array and the imaging plane are perpendicular, singular vectors are related to the plane wave decomposition. For the orthogonal transfer matrix where the following conditions are fulfilled ;

$$\begin{cases} M^T M = M M^T & \text{normality} \\ E_j E_k = 0; \quad j \neq k & \text{orthogonality} \end{cases} \quad (4.10)$$

The angular frequencies of these plane waves has a direct relationship to the singular value weight such that the parallel component has the maximum fidelity (larger singular value).

### 4.3 Array design

It is a well known fact in volumetric imaging that providing a high resolution 3D imaging is closely tied to the aperture characteristics. The quality of the final image is constrained by the number of transducers that defines the number of projections, total aperture size provided by the transducer's active area and frequency response that filters the frequency-rich nature of OA wave or US excitation signal. Aside from the number and size of the transducers, their geometrical distributions play an important role in providing a uniform sensitivity response to an incoming pressure wave. In particular, the questions we try to answer in this chapter are :

- How far the interelement spacing on the array can be increased without affecting the receive information ?
- What is the influence of the aperture size, element size, and the geometrical parameters of the individual transducer ?
- How the bandwidth of the transducer defines the resolution ?

Going to three-dimensional imaging requires at least two dimensional array of transducers in order to achieve the electronic focusing and scanning the volume. Fully populated arrays, despite promises are highly demanding and if respected accordingly, would be costly in addition to optical coupling concomitant difficulties.

In the pursuit of alternative pattern, with sparser distribution and lower periodicity, we found that annular array has shown a good agreement between limited number of transducers and the geometrical distribution in order to provide a uniform coverage. In US imaging, the analytical solution based on *Huygens-Fresnel* and classical SAFT principle explains the achievable spatial resolution for annular geometry which is equivalent to the fully sampled aperture of twice the size working in flash-echo mode [113]. Parenthetically, this demonstrates the superior achievable resolution in US imaging in compare to optoacoustic (which is akin to flash-echo mode), mainly due to the higher obtainable projection.

Albeit in a real case scenario for the otherwise point sources/detectors, the angular sensitivity diminishes with increase in the size of element. Further, averaging over the surface of elements diminishes the lateral resolution. However, this averaging behavior increases the SNR of the transmitted and recorded signals plus the fact that the ensuing blurring effect can be tackled by the correct weighting factors [78] or deconvolving the SIR [97]. In chapter 5, the degree of effectiveness for each of these approaches will be evaluated. Yet, because of the transducer larger active surface the near field extends, hence the transducers shows a directional response and that has a negative impact on spatial sensitivity. The ill-suited narrow view angle can be compensated by defocused transducer or introducing a negative lens in front of the elements. Withal, in such configuration there is not much degree of freedom to simultaneously evaluate the effect of the number and size of the elements.

On a comparative study [102], Graullera *et al.* found similar performances between sunflower Fermat-spiral array and circular-annular array. The lesser periodicity in Fermat spiral configuration encourages the sparser distribution and subsequently more freedom in choice of parameters. The sparse array also means larger aperture, which brings about a large view angle that concede with more angular frequencies for the transmitted or received wave and simply more spatial degree of freedom in defining the behavior of the emanated wave at each point of the medium in the far field. Thus the number of focal spots are increasing with the gain in aperture size, even if the central part of the aperture needs to be compromised for the optical illuminating probe. Considering the optical probe radius  $R_O$ , the position of  $n^{th}$  element can be defined as [131] :

$$r_n = (R_{Ap} - R_O) \sqrt{\frac{n \cdot \Phi}{(N - 1) \cdot \Phi}} \quad (4.11)$$

where  $\Phi \approx 137.51^\circ$  is the the golden divergence angle which is approximated by the ratios of

Fibonacci numbers, an indication of irrationality that follows the lesser periodicity and grating lobe. At this angle, the peculiar arrangement of the outer elements are relatively compact, insuring the uniform spatial response.

In the next section we are investigating the effect of number and size of elements in two arrangements, annular circular and annular spiral. For the simulation study the elements are set to function at 5MHz central frequency with 80% fractional bandwidth. For the numerical calculation and *in silico* studies, the well known spatial impulse response (SIR) method has been used to correlate the radiating source at a given point to the pressure-field sensed by the sensors. This is taking place by convolution between SIR and acousto-electric impulse response (AIR) of the transducer. We found the well known FieldII simulations toolbox [74] convenient. The quantitative and qualitative evaluation are taking place in the frameworks of pre-reconstruction commensurate with the aforementioned analysis tools and metrics. To optimize these parameters, a systematic analysis based on aforementioned approaches has been followed rather than heuristic trial and error based up on visual assessment.

### 4.3.1 Frequency response

In contradistinction to US imaging, the frequency response of the detector in OA commensurate with the absorbents structure, as the source frequency response are solely defined by the size of the absorbent. For instance, a 5 mm diameter absorbing structure can produce the OA spectrum of 0 to 1.5 MHz with the peak at 0.45 MHz [8]. This is where the importance of broadband acoustic response for the detector is being recognized in OA imaging. Therefore depending on the targeted tissue, one must manage the trade-off between the sensitivity with the frequency response. In an attempt, Andreev *et al.* [8] formulated the frequency response of the absorbing structure. According to their formula, the upper generated frequency by a sphere of diameter  $a$  can be found using ;

$$f_{a_{peak}} \simeq \frac{1.5\nu}{a}$$

For a multi-purpose imaging system however, the absorbing structure might be different in size and structure, and therefore choosing the right frequency response is a hard agreement between many parameters. As an example, the optically absorbents structure in the breast tissue are within the range of 0.5 to 10 mm diameter. Such a broad range can induce the acoustic waves with different frequency response, from few MHz down to tens of KHz [5], which according to the above formula would be 9 MHz down to 48 KHz.

Therefore, we believe that the 5 MHz transducer with 80% fractional bandwidth (B.W.) is a satisfying compromise. In theory, this B.W. allows us to register absorbent with a size down to 0.3 mm.

### 4.3.2 Light delivery system

The light penetration carrying enough photons for the sake of OA pressure pulse  $P_{max}$  induction has been reported upto upto 20 mm [40] and 80 mm [80] respectively for in *in vivo* and *ex vivo*. The light delivery in OA imaging probes is normally consist of multiple optical fibers or one or two fiber bundles that is coupled to the US probe. The illuminated light on the surface of the imaging tissue propagates supposedly in a fashion to optimally and uniformly cover the FOV of the US probe. Hence, the light delivery mechanism intends to adopt to the requirements of the US probe ; yet optimize the trade-off between the optical fluence for deep tissue imaging (*i.e.* > 20 mm) and maximum permissible exposure to pulsed laser which for skin is permitted upto 20 mJ/cm<sup>2</sup> with corresponding intensity (time averaged) of 200 mW/cm<sup>2</sup> for 10 Hz pulse repetition frequency [1]. Maximizing the probability of OA signal generation is crucial for improving the sensitivity of OA imaging system. For a point source, the relation between the maximum achievable induced OA

pressure pulse  $P_{max}$  and the fluence per pulse  $F$  is given by [178] :

$$P_{max} \propto \frac{\Gamma \mu_a F}{\tau^2} \quad (4.12)$$

where  $\mu_a$  is the absorption coefficient of the point,  $\Gamma$  is the Grüneisen parameter describing the transduction ability of the absorbent in optic to acoustic wave conversion and  $\tau$  is the standard deviation for full-width half maximum of the Gaussian profile. When the higher power is more favorable, as is the case for optically deep imaging, the single fibers are less preferred than fiber bundles. The small core of single fiber makes them insusceptible to deliver high energy density at the irradiation site. On the other hand, the large active area of the bundle allows them to be easily coupled to higher laser energy density.

Aside from the energy density, other parameters playing essential role in the dynamics optical fluence are the beam diameters and illumination angle. Monte Carlo simulations were performed for further evaluation of these factors [70]. Simply put, a set of photons (3000000) with equal weights are launched into the interface of water with skin surface. The photon propagation through the medium is governed by the *Henyeey – Greenstein* phase and exponential probability distribution functions to count for random walk scattering angle and step size *w.r.t.* the photon energy loss. The process is repeated for every photon, individually, till the remained energy doesn't exceed than the preset value for the minimum energy of a photon. The medium is discretized to a known grid size and the energy loss of each voxel is assigned to the tissue type optical properties. Finally, the spatial map of energy loss/deposition is calculated and can be related to fluence by an adaptive division of obtained map over the known local absorption coefficient. For the generic handheld probe, the aim is to cover the FOV of the ultrasonic array upto 30 mm. As for any optically deep imaging, the

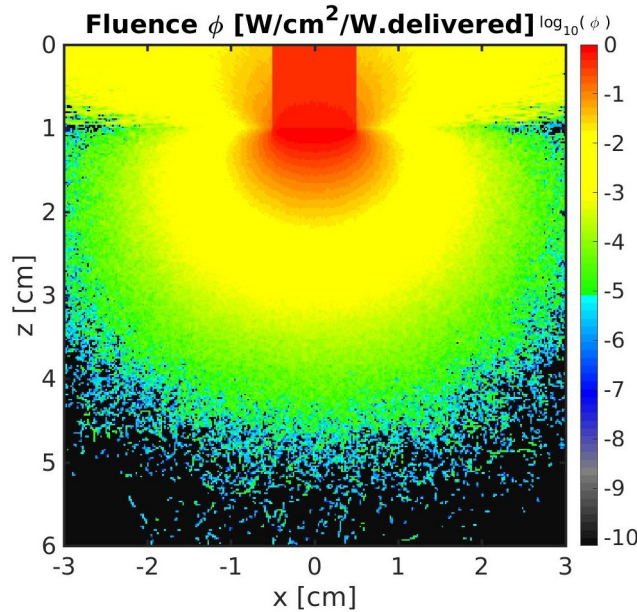


FIGURE 4.2: The logarithmic scale of optical beam fluence of the 1cm beam irradiating on the surface of epidermis and water. The reflection of the fluence back to the water and propagation of the light is presented.

heterogeneity of the tissue causes higher scattering and perhaps lesser axial fluence of the injected light to the imaged tissue. Moreover, the skin is acting as an inhibitor, owing to its moderately high reflection and optical heterogeneity. However, for the sake of ease in calculation, we simplify the simulation in to three parallel layers with optical properties of water, epidermis and dermis tissues. Through a series of simulations with varying beam diameter and angle of illumination, we empirically conclude that 10 mm  $\varnothing$  beam perpendicularly irradiating the surface of tissue satisfies the 30 mm requirements. Figure 4.2 shows the  $xz$  profile of optical fluence from 10 mm  $\varnothing$  beam

with 1000  $nm$  wavelength irradiating on the surface of skin (located at  $z = 1cm$ ) perpendicularly. At 30  $mm$  depth, the  $-3$  dB energy density is achievable. Another noteworthy aspect is the high energy density ( $> -1$  dB) at the irradiation surface upto few  $mm$  depth; which results in so called clutter. In design of the array, the elements size and their distribution can be arranged for the aperture to be least sensitive, if not blind, to the incoming wave from the aforementioned area.

### 4.3.3 Design strategy

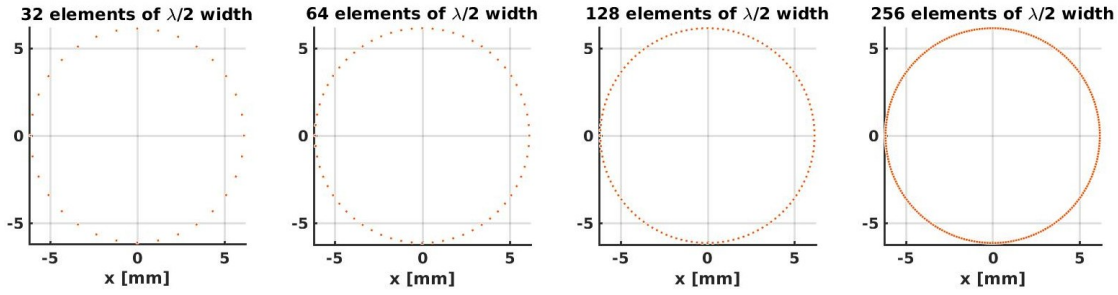
In this section, by taking into account the light delivery system housing for perpendicular illumination, we are exploring the optimum geometrical properties for the handheld OPUS. The design array supposedly provides enough flexibility in element's width, high and distribution such that the periodicity is minimized and the agreement between directivity, sensitivity, spatial aliasing can be settled.

To begin with, simple segmented annular geometry where the elements are distributed equidistantly in a ring fashion around the optical probes has been considered. This geometry offers the circular symmetry for the ultrasonic beam, making the volumetric imaging possible with no mechanical steering required. A forward looking segmented annular array of 128 elements operating at 5 MHz center frequency with 80% fractional bandwidth has been modeled.

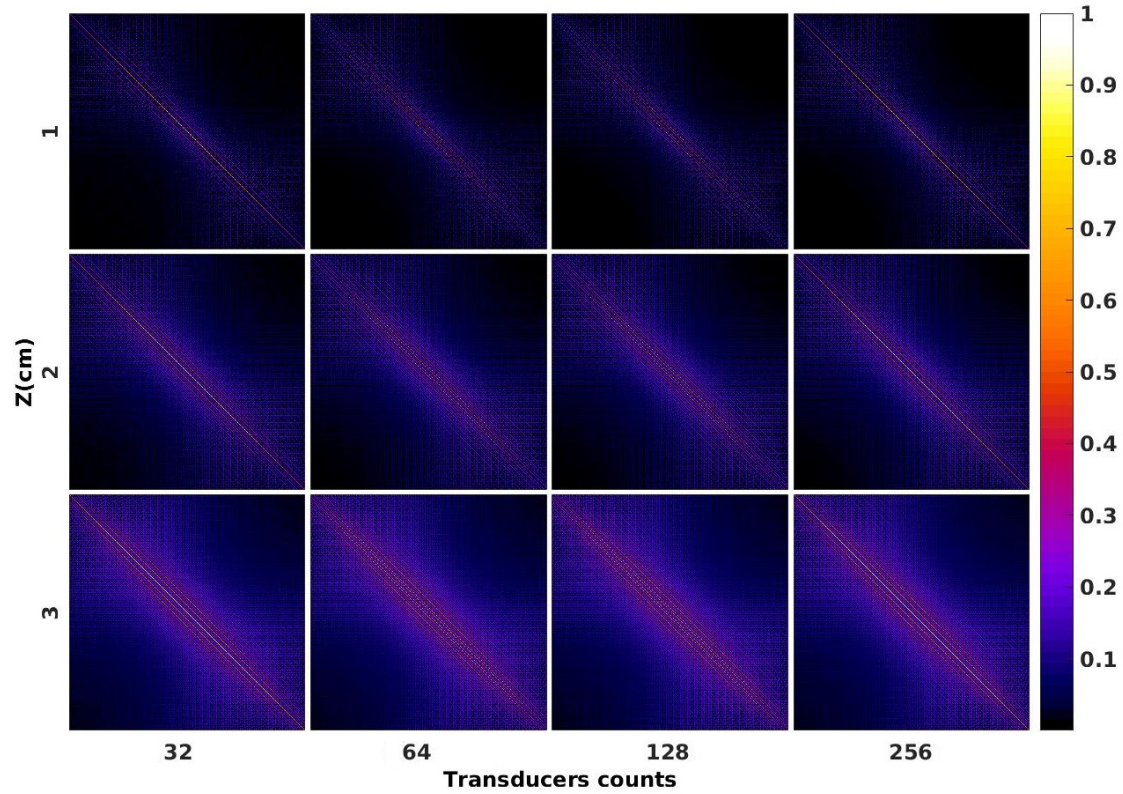
#### Inter-element spacing

We start with the effect of inter-element spacing but for this particular geometry which confines to one ring, it has a direct effect on the number of projections. Herein the results of voxel crosstalk analysis of the model matrix that estimates the spatial sensitivity and spatial aliasing are presented for four arrays composed of 32, 64, 128 and 256 elements of  $0.5 \lambda$  size as shown by Figure 4.3a. The 11  $mm \circlearrowleft$  lumen is considered for the optical probe which imposes a linear and reciprocal relationship between element number and inter-element spacing. The height of element is set to  $\lambda/2$  for all of the arrays, in order to eliminate the other possible discrepancies (*e.g.* directivity). The FOV of  $18 \times 18 \times 20 mm^3$  has been considered, but only three axial slices, each composed of  $100 \times 100$  pixels has been visualized.

Figure 4.3b represents the crosstalk matrices calculated for each of the arrays at three different  $xy$ -planes away from the aperture, respectively at 1, 2 and 3  $cm$ . Since OPUS is a spatial variant imaging system, voxel basis functions, as the name indicates, are well localized in spatial domain and indeed is effective for space relative concerns such as spatial sensitivity and spatial aliasing. While  $i^{th}$  diagonal element of the crosstalk matrix  $H$ , determines the strength of the corresponding voxel's  $H_{ii}$  contribution to the measured data, the off-diagonal elements  $H_{ij}; i \neq j$  reveals the correlation between the elements  $i$  and  $j$  such that the value of  $\frac{H_{ij}^2}{H_{ij}H_{ii}}$  indicates the separability and consequently spatial aliasing between two voxels. Therefore, a better imaging system is the one with weaker off diagonal and stronger diagonal elements. This can be investigated in both quantitative and qualitative manner. The quantitative analysis is taking place by comparing the crosstalk matrices individually with the unitary matrix via the aforementioned FoMs. The results are summarized in the Table 4.1. The RMSE and MAE are the error measurement factors, therefore their lower values theoretically indicate for a better performance, in contrast to PSNR with otherwise interpretation. Yet, rather than the matrix rank, the other FoMs surprisingly are not showing a substantial change as the number of elements are increasing, making the interpretation non-trivial. On the other hand the rank is suggesting a better performance with increase in the number of elements. Specifically, the aperture with 256 elements is showing the full rank-behavior. The qualitative analysis in parallel with quantitative analysis, draw the similar conclusion. Figure 4.4a is demonstrating the 60 dB logarithmic scale (*w.r.t.* the energy at the surface of the transducer) for the sensitivity map. With more elements, the energy is naturally increasing and a larger area is being covered. This is obvious also, from the Figure 4.3b, with the diagonal elements showing stronger amplitude for aperture with more element counts. While off diagonal elements might be increasing in quantity, they show lesser value per individual parasitic contribution( $H_{ij}$ ). This is the main reason behind the more or less constant FoMs in Table 4.1. In the same context,



(a)



(b)

FIGURE 4.3: (a) Schematic of four annular arrays differ in number of elements and inter-element spacing and (b) their crosstalk talk matrices for three  $xy$ -planes parallel to the aperture situated at the axial distances (depths) respectively at 1, 2 and 3 cm away from the aperture. The crosstalk matrices are normalized *w.r.t.* the maximum element in each matrix.

Figure 4.4 illustrates the spatial aliasing, or the over all inter-voxel crosstalk, for the two central and marginal pixels.

Regarding or regardless of the transducer count, one might pose the question "What if the overall active surface area be the same for all apertures"? In such a sense, simply by increasing the width of elements to meet the boundaries of the neighboring, not only overall active surface of the apertures becomes analogous, but by doing so the effect of element width can be investigated as well. Our analysis therefore is extended toward the apertures with the same number of elements but larger size in the same geometrical distribution. The qualitative results are represented in the right column of the Figure 4.4. It is clear that the apparent reflectivity of target in US and source



FoM	$xy$ -plane	32 elements	64 elements	128 elements	256 elements
RMSE	1cm	0.0588	0.0589	0.0595	0.0595
	2cm	0.0878	0.0896	0.0901	0.0903
	3cm	0.1254	0.1295	0.1296	0.1296
MAE	1cm	0.0317	0.0320	0.0323	0.0324
	2cm	0.0586	0.0599	0.0602	0.0604
	3cm	0.0928	0.0959	0.0960	0.0960
PSNR	1cm	24.6111	24.5986	24.5134	24.5036
	2cm	21.1306	20.9538	20.9095	20.8817
	3cm	18.0364	17.7565	17.7480	17.7491
Rank	1cm	1568	3136	6272	10000
	2cm	1536	3072	6144	10000
	3cm	1568	3136	6272	10000

TABLE 4.1: Quantitative evaluation of virtual array performance on transducer count.

in OA depends on the position of target *w.r.t.* the array. The spatial sensitivity map of the probe aperture as a function of cited trade-off at three different axial planes (depth) respectively at 1, 2 and 3 *cm* are illustrated. The effect of element width on the sensitivity is clear. Regardless of the element count, the element size has a direct effect on the sensitivity map. Additionally, the presented data are inferring the directivity effect as a function of element width on the sensitivity field, and the introduction of diffraction (Fresnel) pattern as well. For example, for the case of aperture the 32 elements of  $4\lambda$  width in Figure 4.4b, the near field is extended up to 3 *cm* with mark on the sensitivity map.

On the other hand, interpreting the aliasing map would be a bit complicated. While for the central voxel, there is not much noticeable difference between the left and right column, the result for the marginal image suggest that the aliasing increases, if the element size increases, and that is accompanied by the larger contribution of particular pixels  $H_{ij}$ , almost equal to the corresponding pixel  $H_{ii}$ . Looking into the quantitative result 4.1, one can further conclude that element width, increase the SNR as suggested by the value of PSNR. The vague point might be arising though from the reduction in the error, which is not expect from the aperture with lesser projections. But one should consider that the RMSE and MAE are ignoring the fact the the errors are lesser as the overlapping area in this specific geometry is decreasing with the larger element size, due to the directive angle of view. Therefore, the last two metrics result must not be incorporated, and this condition is dictated by the sensitivity map. The rank however didn't change from previous result as the number of projections remains the same.

Both the spatial sensitivity and aliasing are computed after voxel crosstalk matrix which is calculated from the system mode matrix . As could be expected, with increase in number of elements and lesser inter element spacing, the performance of the system in terms of aliasing improves but due to the smaller size of elements, the overall energy drops.

The other sort of analysis that might help us with the interpretation is the eigenspectrum analysis for each of the four virtual probe. As depicted by Figure 4.5, the probe with the larger elements are containing the largest eigenvalue which is an indication to the signal fidelity, yet faster decay demonstrate a lower performance. The subtle difference between probe with 128 and 256 elements, making the 128 elements probe with  $\lambda$  interelement spacing ( $\simeq$  element width) is a reasonable choice of imaging performance. These results along with the crosstalk outcomes confirm that 128 element aperture provides the right trade off between the number of elements and interelement spacing and similarly the width of elements.

It worth noting that the rank of our model matrix is not found from the eigenspectrum which is a heuristic challenge, rather we used the eigenfrequencies of the eigenvectors for proper selection of eigenvector and in order to distinguish the null space, knowing that the null space is spanned by the column of eigenvectors corresponding to the vanishing eigenvalues with high-frequency vibration

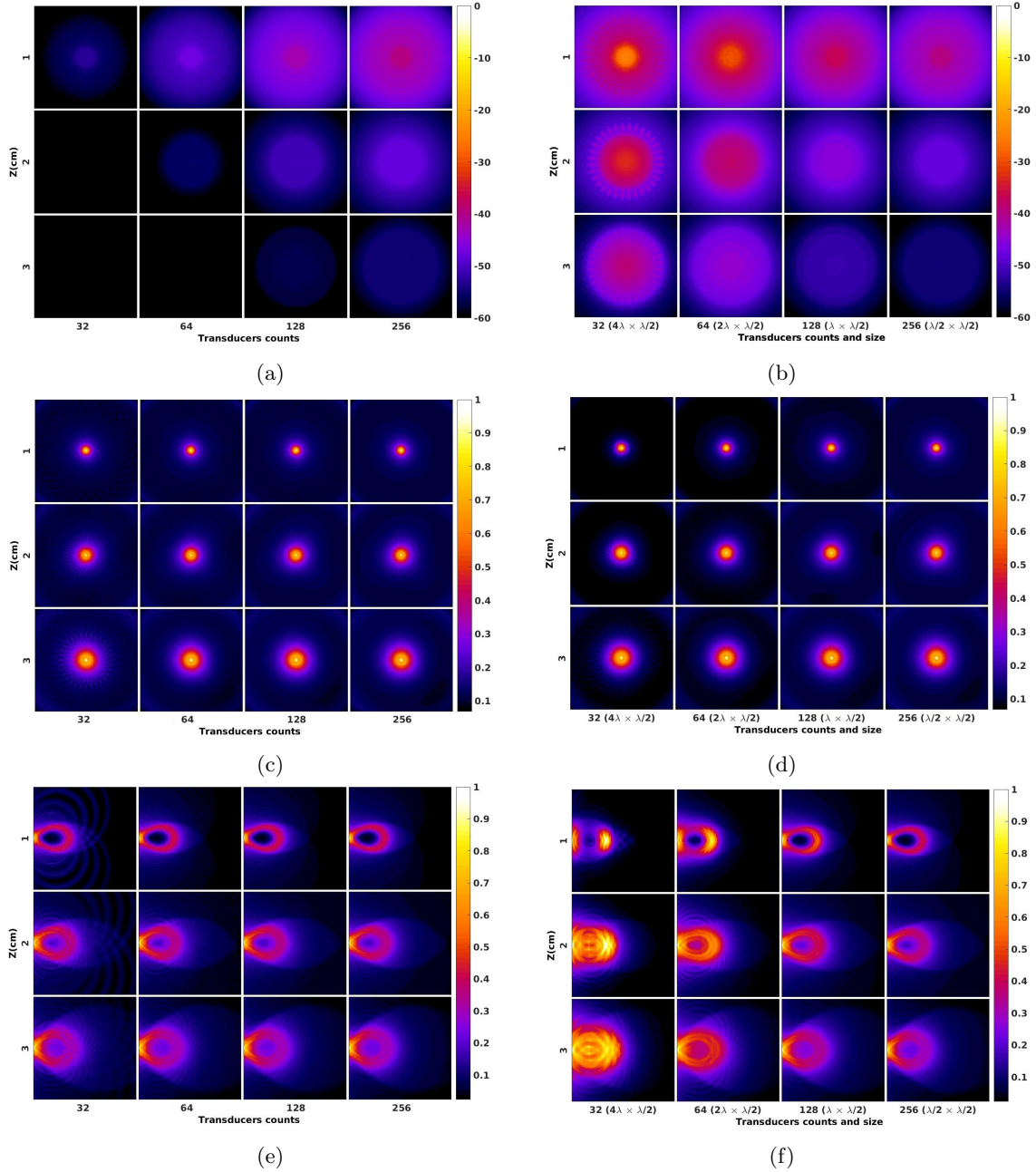


FIGURE 4.4: (a,b) 60 dB sensitivity map of four virtual apertures with different number of elements, in three axial planes away from the aperture. (c,d) Spatial aliasing for the central elements and (e,f) The marginal elements. The parasitic contributions from other voxels are decreasing with increase in transducer count. The images are normalized with respect to the maximum value (*i.e.* the corresponding voxel) of the image. In left column the element size are equal and in right varying per aperture.

(*e.g.* noise) thus highly inaccurate. This representation shows the most correlated eigenvectors that are the principal component of the matrix in the vicinity, indicating spatial frequencies. Even though each vector contains more than one spatial frequencies, they are still distinct from noise (null space) with much higher vibration and lower eigenvalue. Figure 4.6 is representing the spatial Fourier transform of the singular vectors of the crosstalk matrix calculated for the aperture with 32 elements at the 2cm axial plane.

FoM	$xy$ -plane	32 ( $4\lambda \times \lambda/2$ )	64 ( $2\lambda \times \lambda/2$ )	128 ( $\lambda \times \lambda/2$ )	256 ( $\lambda/2 \times \lambda/2$ )
RMSE	1cm	0.0149	0.0226	0.0323	0.0375
	2cm	0.0287	0.0436	0.0554	0.0602
	3cm	0.0479	0.0701	0.0834	0.0882
MAE	1cm	0.0035	0.0073	0.0129	0.0159
	2cm	0.0114	0.0219	0.0313	0.0350
	3cm	0.0243	0.0430	0.0548	0.0590
PSNR	1cm	36.5410	32.8994	29.8134	28.5208
	2cm	30.8396	27.2041	25.1347	24.4010
	3cm	26.3915	23.0796	21.5817	21.0932
Rank	1cm	1568	3136	6272	10000
	2cm	1536	3072	6144	10000
	3cm	1568	3136	6272	10000

TABLE 4.2: Quantitative evaluation of virtual array performance on element counts-width.

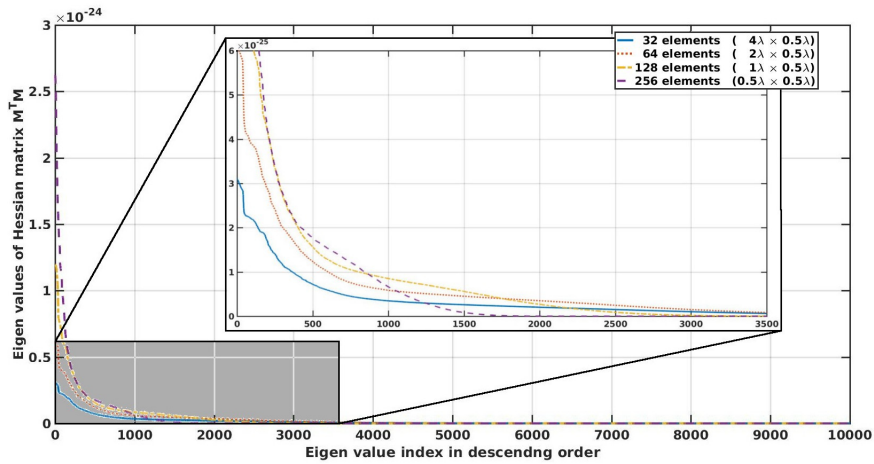


FIGURE 4.5: Eigenspectra of the hessian matrices for the transfer matrix of four virtual arrays. The highlighted region has been magnified for better visualization.

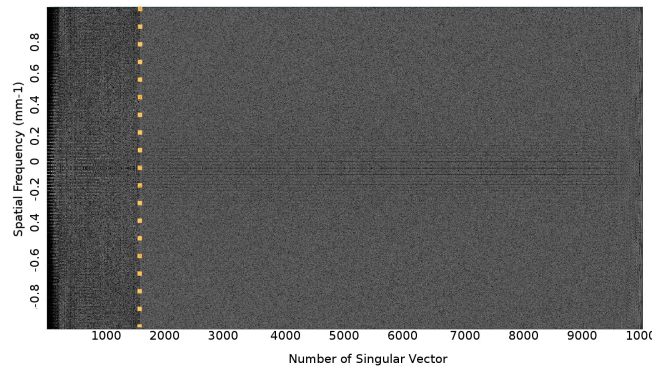


FIGURE 4.6: The spatial frequency of model matrix eigen-vectors. The yellow dotted line shows the rank where the null space (right side of the line) is distinguished from the primary components (left side of the line).

## The aspect ratio

Clearly, the aperture with 128 projections requires the larger elements to ensure the adequate SNR for detection of weaker pressure wave. This is true specifically for the PZT based transducers, where the thermal-induced noises are decreasing with wider elements owing to their higher electrical capacitance. As the element width is limited to  $\lambda$ , therefore the degree of freedom or the parameter to play with is the height of the transducer. However, the element height must be commensurate with the angular vision to avoid the directive angular view. Give the size of element  $h$  set at central frequency  $f_0$ , it is known that the -6 dB angle of view  $\beta$  is inversely proportional to the element size (in this case height  $h$ ) [173],

$$\beta_{-6dB} = 2 \arcsin \left( \frac{0.6\lambda}{h} \right). \quad (4.13)$$

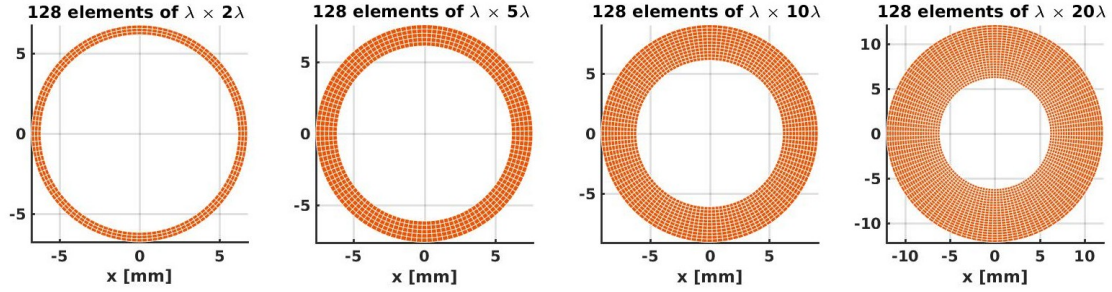
To cope with, we simulate the negatively defocusing for every element in convex structure as if the focus is behind the transducer thus the angle of vision expands. In real case, there are some limitation associated with manufacturing the curved surface for transducer and defocusing is taking place by the help of negative acoustic lens [126] to diffract acoustic rays and energy away from the center and further minimize the near field. It has been shown that the acceptance angle  $\beta_{-6dB}$  can be enlarged upto  $60^\circ$ . Therefore the overlapping area and consequently FOV grows larger and accepting angle increases. In our simulation study, we divide the element to  $\lambda/2$  sub-elements and apply the delay such that the emanating wave on the surface is diverged by the cylindrically convex active surface. The delay is applied such that the radius of curvature (ROC) is half of the element height, for every element of the transducer, in order to compensate for the directivity. It worth noting that due to the acoustic reciprocity, the transmission field where elements are driven by delta shape pulse are analogous, if not exactly the same, to the receive sensitivity.

Figure 4.7b represents the crosstalk matrices calculated for four arrays varying in the height respectively 2, 5, 10 and 20  $\lambda$  and is followed by the Figure 4.8 which highlights the effect of element height in both spatial sensitivity and spatial aliasing.

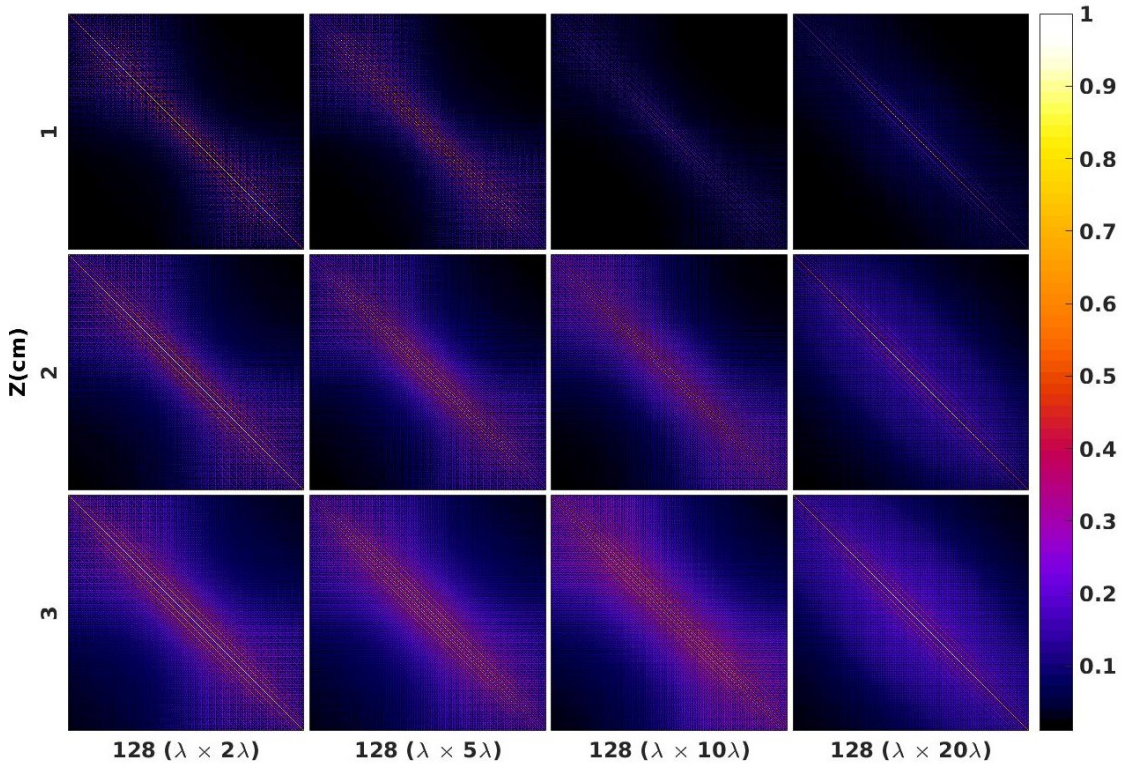
A simple interpretation based on the visual analysis of crosstalk matrix quality for the four apertures is implying the superior performance of the aperture with larger elements. The relatively stronger diagonal elements which brings about the higher sensitivity for the volume of interest, is depicted in Figure 4.7b. The ringing artifact in the sensitivity map is introduced by the negative focusing. It will be shown on chapter 5 that this artifact might affect the quality of the image if not incorporated into the image reconstruction step. Yet, it seems that the aperture with  $20\lambda$  element height is showing a more uniform behavior in sensitivity and energy distribution than the rest of the apertures with smaller elements. In terms of the spatial aliasing, it is expected that the larger elements give rise to more aliasing, but in fact their weight of these parasitic contribution is more important than their numbers. In general, higher number of low weighted spatial aliasing is preferred to lower number but heavy weighted contribution. At first, it seems that both the number and their weight is increasing as the element increases, as is the case for the aperture with  $2\lambda$  and  $5\lambda$ , but then the individual weights are decreasing even-though it seems that it is distributed to the neighboring voxels, causing much lower crosstalk between neighboring voxels.

As a conclusion, from the qualitative analysis, in single ring segmented annular array the best result is given by the aperture with 128 elements of  $\lambda \times 20\lambda$  size. It has the weakest off-diagonal components indicating the lesser aliasing, along with the prominent diagonal elements. Moreover, the spatial sensitivity map is more uniform with higher energy.

Table 4.3 outlines crosstalk analysis of the imaging performance of segmented annular array of 128 elements. The aperture with  $20\lambda$  element height has the highest PSNR, which is an indication for the sensitivity. Also, it seems that for the volume of interest, the aperture provides the full rank matrix up to the depth of 3 *cm*. The value for RMSE and MAE are close to the aperture with  $10\lambda$ , yet lesser than the other two, indicating a better capability in separating the two contributor. The imaging operator of each of these arrays has been subjected to the rank measurement as well.



(a)

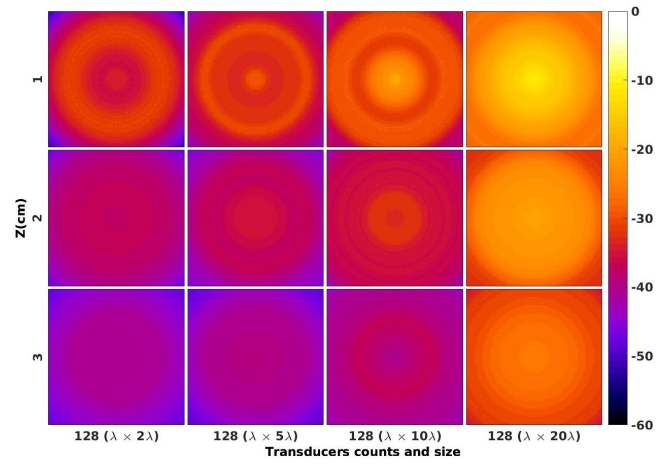


(b)

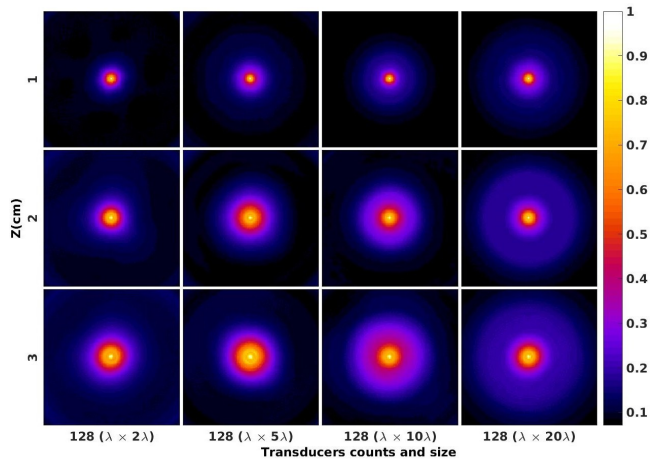
FIGURE 4.7: (a) Schematic of four segmented annular arrays of 128 elements varying in element height. (b) The corresponding crosstalk matrix for three axial plane away from the aperture. It is clear that for the aperture with larger elements, the diagonal elements are stronger and off-diagonal elements are much weaker.

Again, it seems that only the  $20\lambda$  element height can bring the full rank properties for the 128 projections, in this specific geometry.

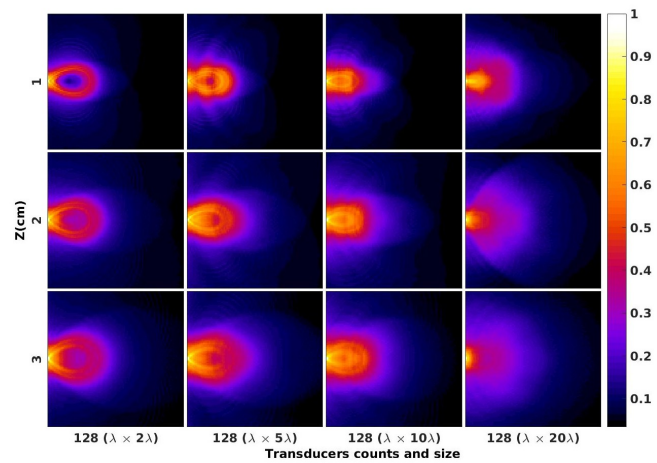
The later is also visible form the qualitative result as depicted by Figure 4.8b and 4.8c, where the aliasing map are suggesting that for a larger aperture the significant parasitic contribution from the neighboring area of the voxel of interest is indeed shrinking. As mentioned earlier, an important aspect of the error metrics used for performance evaluation based on the model matrix is that the RMSE and MAE can be analyzed in parallel. While MAE is affected by large amount of averaging errors, RMSE is implying particular large errors. One can also look into the differences between the RMSE and MAE in order to evaluate the variance in the individual errors. As the difference is negligible, the we believe that the errors are in the same magnitude.



(a)



(b)



(c)

FIGURE 4.8: Qualitative comparison on the effect of the height based on (a) 60 dB sensitivity map, (b) spatial aliasing for the central pixel and (c) spatial aliasing for the marginal pixel. The aperture with larger elements shows a better spatially sensitivity with lesser parasitic contribution.

FoM	$xy$ -plane	128 ( $\lambda \times 2\lambda$ )	128 ( $\lambda \times 5\lambda$ )	128 ( $\lambda \times 10\lambda$ )	128 ( $\lambda \times 20\lambda$ )
RMSE	1cm	0.0933	0.0966	0.0429	0.0447
	2cm	0.1282	0.1298	0.1255	0.0940
	3cm	0.1553	0.1566	0.1717	0.1244
MAE	1cm	0.0457	0.0513	0.0231	0.0281
	2cm	0.0826	0.0862	0.0851	0.0704
	3cm	0.1123	0.1159	0.1288	0.0991
PSNR	1cm	20.6059	20.3032	27.3482	27.0032
	2cm	17.8453	17.7321	18.0281	20.5383
	3cm	16.1746	16.1044	15.3063	18.1041
Rank	1cm	6144	6144	6144	10000
	2cm	6144	6144	6144	10000
	3cm	6144	6144	6144	10000

TABLE 4.3: Quantitative evaluation of virtual array performance on element height.

This spatial crosstalk map provides a measurement of the spatial aliasing and sensitivity based on the discrete model of the aperture. By employing the spatial crosstalk potentially a principled argument is provided for comparative studies between the performance of different imaging system. It mentioned earlier that eigenanalysis is providing another argument. To further investigate the effect of larger elements in the performance of these annular arrays and a more robust conclusion, examination of the matrix rank and the effect of contributing object space singular values to the model matrix were performed to explore the eigen-properties of the four apertures. The eigenspectrum of the four virtual arrays is illustrated in the Figure 4.9. Once again the aperture with the larger elements are establishing a well performance, which is shown by slower decay accompanied with larger eigen components as well, which are the two main parameters in eigenspectrum analysis.

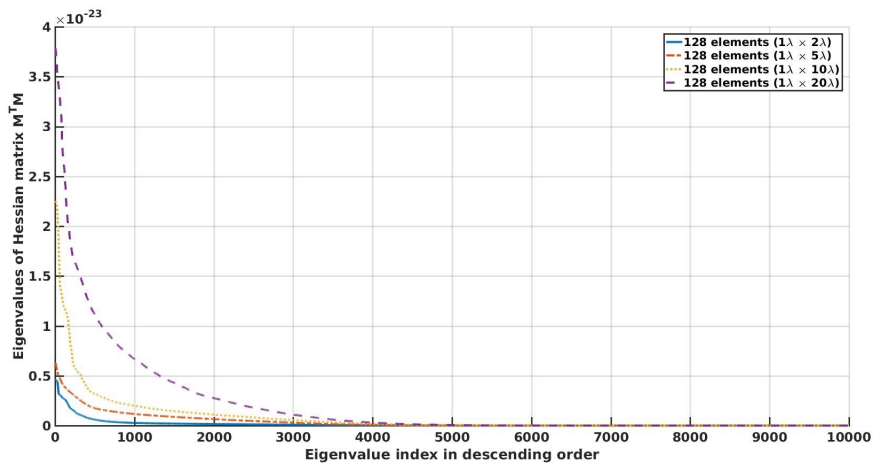


FIGURE 4.9: Eigenspectra of the hessian matrices for the transfer matrix of four virtual arrays, varying in the height of element.

Next is a survey on the aperture limited view and its effect on the information gain/loss, by further excavating the model matrix. It has been discussed that in the backward mode optoacoustic imaging, such as the handheld probe, where the angle projections are highly limited to the acquisition side, the system is able to partially acquire the emanated wave from the medium. Comparatively, this problem has been overcome in US imaging by the help of beam-forming in transmission, the finite size of the aperture limits the generation of US wave in particular direction as well. The information about the number and type of angular frequencies ( $\simeq$  plane-waves) that

an aperture can generate or similarly receive, in order to define a point in the FOV are contained in the transfer matrix. For an object plane parallel to the aperture (axial planes), these information can be retrieved using SVD. For example, for plane wave imaging, each angle of transmission can be determined by the Fourier transform of the singular vector. The first singular vector is corresponding to the emission of DC component (*i.e.* flash plane wave traveling in direction perpendicular to the transducer). Normally, the largest singular vectors are associated with low angular frequency components. However this not always true about annular geometry. For the case where the object plane is near the aperture, the lower angular frequency components are not being detected at all due to the limited detectors directivity. This property of the annular geometry is rather useful in OA imaging, as it allows to avoid the induced clutter at the superficial irradiated layers.

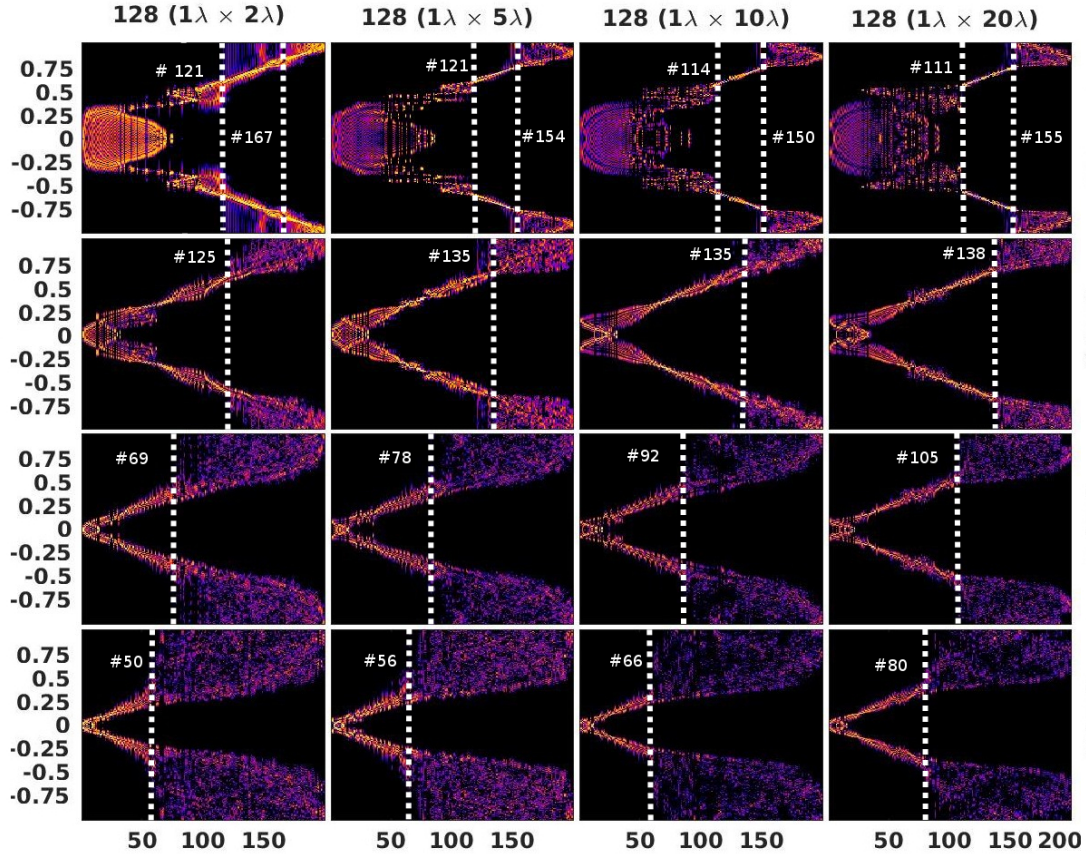


FIGURE 4.10: SVD analysis of the transfer matrix for 200 observation points along the central line at 4 different axial planes away from the aperture. The spatial Fourier transform of all singular vectors of the transfer matrix of the aperture. The  $y$ -axis is the spatial frequency ( $mm^{-1}$ ) and  $x$ -axis is the number of singular vectors happen to be the same as number of control points. If not polluted with the noise, every main singular vector is bounded to a particular spatial frequency. The white dash line is the boundary of the significant singular vectors from the noise with the number pinpointing the degree of freedom for defining the spectral resolution for defining control points.

Figure 4.10 represent the spatial fourier transform of the right hand side singular vectors, for four axial plane away from the transducers, respectively 0.1, 1, 2 and 3  $cm$ . As the system response is symmetrical, we only investigate a line along the center containing 200 control points for of the size of 12  $mm$ , where the maximum sensitivity in every plane is expected, as shown by the Figure 4.8a. For the axial plane located at 1  $mm$  away from the transducer, as depicted by the first row in Figure 4.10, the left side of the white dashed line is depicting the discrepancies associated with the lower angular frequency components. On the other side, the higher frequency components, in the right side of the second dashed line, are not containing information but noise. The relative



meaningful information are limited to the area between the two dashed lines, thus lesser clutter wave is being detectable. For the other three axial planes, where the control points are farther from the aperture, the lower angular frequency components are stronger and contain resolvable information. The separating border between the noise and meaningful data is highlighted by the white dashed line. The adjacent number is pinpointing the turning point of which segregate the resolvable and unresolvable spectral areas. Unlike the 1 *mm*, the meaningful the other plane are located in the left side or the lower frequencies. One can notice that with the larger elements, not only higher amount of angular frequency are available, owing the larger aperture, but the frequency component are defined in a finer fashion where each meaningful singular vector contains narrower spectrum. Each singular vector of the propagation operator is associated to certain frequencies. Therefore, an estimation about achievable spectral resolution is feasible by the corresponding peak frequency to the turning point of singular vectors  $\omega_{peak}$ , such that; *spectral resolution* =  $1/\omega_{peak}$ , recalling that the OPUS is a spatially and spectrally variant imaging system. To be more accurate, the singular vector associated with the  $\omega_{peak}$  can be found using the correlation function analysis expressed by [133] :

$$C(\omega) = \frac{\langle v_i(\omega).v_{i+1}(\omega) \rangle}{\langle v_i(\omega) \rangle . \langle v_{i+1}(\omega) \rangle} \quad (4.14)$$

where the  $v_i$  is the  $i^{th}$  spectral singular vector (*i.e.*  $i^{th}$  column of FFT of  $V$ ) and  $\langle . \rangle$  is the average over  $\omega$ . This function does nothing but measuring the similarity between the two singular vectors. The smallest the value of  $C(\omega)$  stands for the least correlation and implies for the turning point.

Intriguingly, for the case of point like targets, the number of significant singular vector is attributed to the number of targets for the resolved system [125].

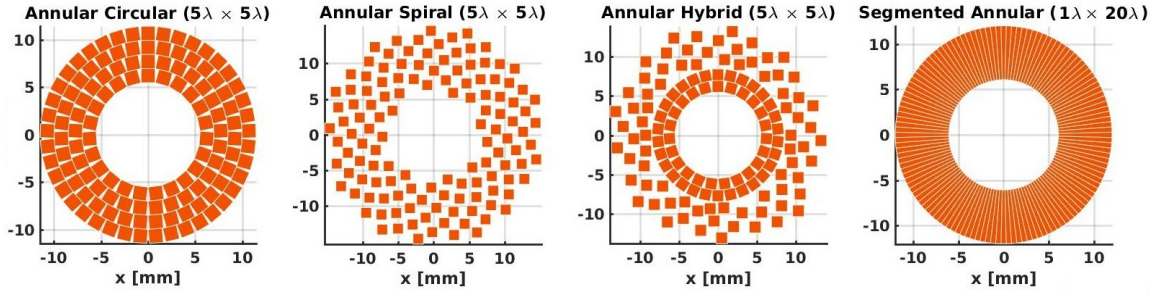
Another phase to consider could be the strength of DC components with the depth. It is true that the higher angular frequency are lost with depth, which also means lesser degree of freedom for defining the given point in the medium, the DC or lower frequency components are presenting a stronger contribution with lesser discrepancies. We attribute this behavior to the directivity or acceptance angle of the aperture. Therefore it is clear that the apparent reflectivity of target in US and source in OA depends on their position *w.r.t.* the array (*i.e.* being spatial variant). Therefore both the quantitative and qualitative results are suggesting the aperture with 128 elements of  $\lambda \times 20\lambda$  size provides a superior performance and the befitting agreement between the different determining parameters.

Withal, one degree of freedom remained to be explore, and that is the geometrical distribution. As the imaging performance is shown to be improving with increase in the size of both element and aperture, a sparser geometry may provide the chance to enlarge both.

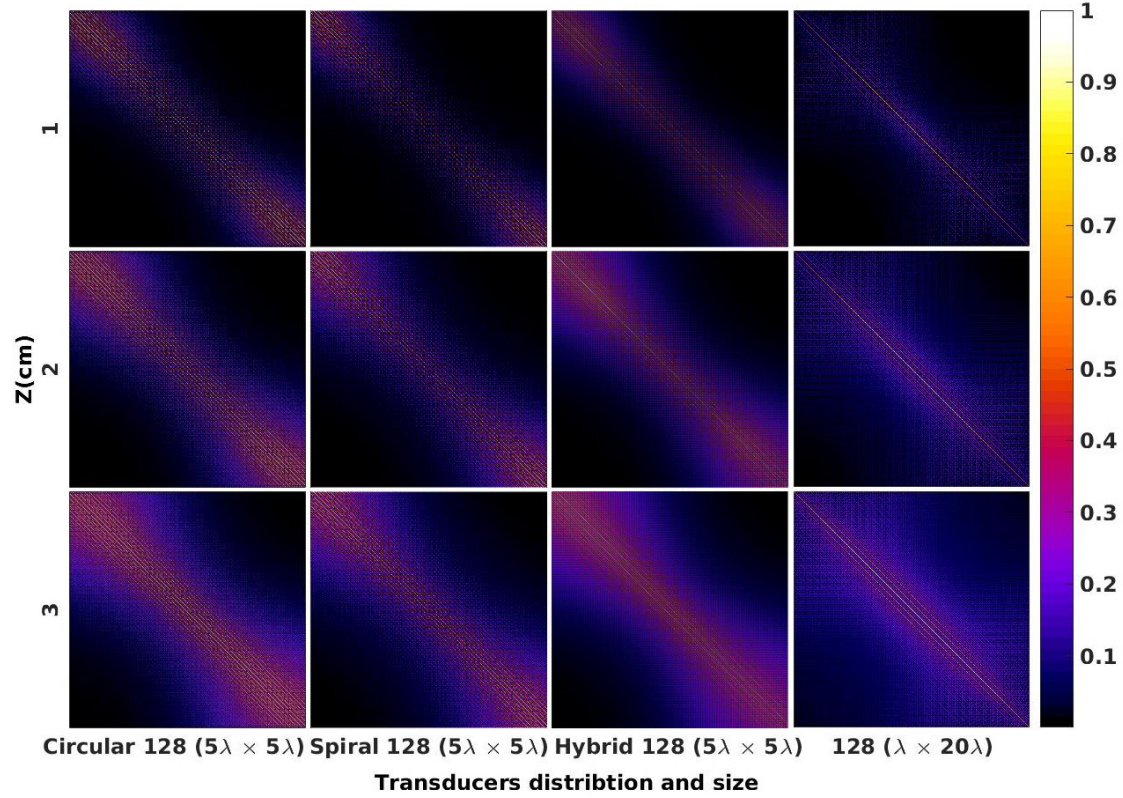
## Geometrical distribution

In the search for a pattern with least periodicity, hereby we explore the geometrical distribution and in that, we would like to see the possibility of increasing the aperture and individual element size such that the unitary aspect ratio for all the elements is hold. Three geometries are analyzed namely, annular circular array (or multiring annular), annular spiral (Fermat) array and annular hybrid 4.11a. The more populated arrangements of the first two aforementioned arrays (*i.e.* no tubular cavity), also known as curvilinear arrays [102], showcased a comparative performance for ultrasound phased array imaging. The last one is a combination of annular spiral and annular circular, to compensate for the energy loss due to the sparse nature of Fermat-spiral. Taking into account the majority of available digital acquisition (DAQ) systems, and to remain analogous to the one-ring segmented annular array, we limit the number of elements to 128. In all cases, minimum interelement spacing has been set to  $5\lambda$  which allows the element enlargement upto the size of  $5\lambda \times 5\lambda$ . We employed the crosstalk matrix and eigenanalysis of both model matrix and transfer matrix for the sake of performance appraisal between different geometries. The same FoMs have been employed for the sake of quantitative comparison appraisal between the apertures and for drawing a decisive conclusion.

Figure 4.11b summarizes the voxel crosstalk matrix of the three considered arrangements plus the segmented annular array for the sake of comparison. The visual perception of the crosstalk



(a)



(b)

FIGURE 4.11: (a) Schematic of virtual annular arrays of 128 elements varying in geometrical distribution. (b) The corresponding crosstalk matrix for three axial planes away from the aperture.

matrix structure implies that for the first three geometries, the central elements of the voxel crosstalk matrix are weighted less than the corner ones, specifically for the 1 cm axial plane. These elements are corresponded to the contribution of central pixels, meaning that the sensitivity of the imaging system for the central area must be lower than the marginal voxels. Figure 4.12a verifies the above statement, specially for the spiral array. The sparse geometry tends to dissipate the energy over the VOI but lack of central elements and limited element's acceptance angle cost severely the energy in the central part. As the distance between the object plane and the plane of imaging increases, the consequences are less severe till at 3 cm almost nullifies and ends to a more or less uniform sensitivity for all voxel in the FOV. This effect was the initial reason behind the hybrid geometry, with the aim of concentrating the overlapping energy at the center, in front of the luminal cavity. The situation improves and the lower energy area is shrinking but in compare

to the segmented annular array, the central area still suffers from the lower energy (Figure 4.12).

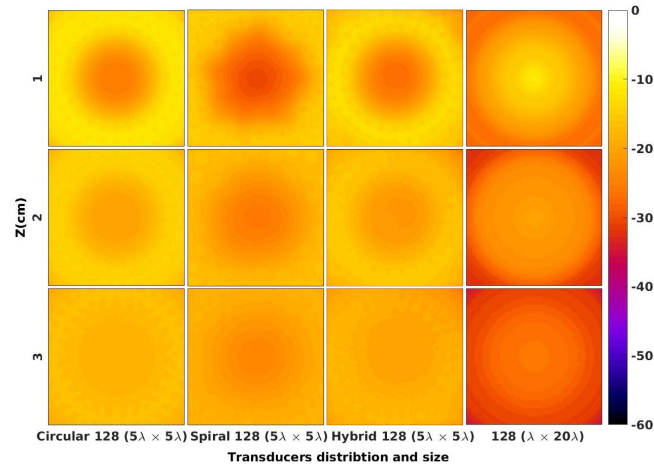
<b>FoM</b>	<b><i>xy</i>-plane</b>	<b>Circular</b> ( $5\lambda \times 5\lambda$ )	<b>Spiral</b> ( $5\lambda \times 5\lambda$ )	<b>Hybrid</b> ( $5\lambda \times 5\lambda$ )	<b>Annular</b> ( $1\lambda \times 20\lambda$ )
RMSE	1cm	0.1127	0.0904	0.1033	0.0447
	2cm	0.1513	0.1198	0.1433	0.0940
	3cm	0.1863	0.1471	0.1745	0.1244
MAE	1cm	0.0468	0.0366	0.0454	0.0281
	2cm	0.0813	0.0624	0.0793	0.0704
	3cm	0.1157	0.0870	0.1109	0.0991
PSNR	1cm	18.9613	20.8779	19.7195	27.0032
	2cm	16.4050	18.4292	16.8734	20.5383
	3cm	14.5938	16.6468	15.1620	18.1041
Rank	1cm	10000	10000	10000	10000
	2cm	10000	10000	10000	10000
	3cm	10000	10000	10000	10000

TABLE 4.4: Quantitative evaluation on the performance of four virtual array varying in distribution.

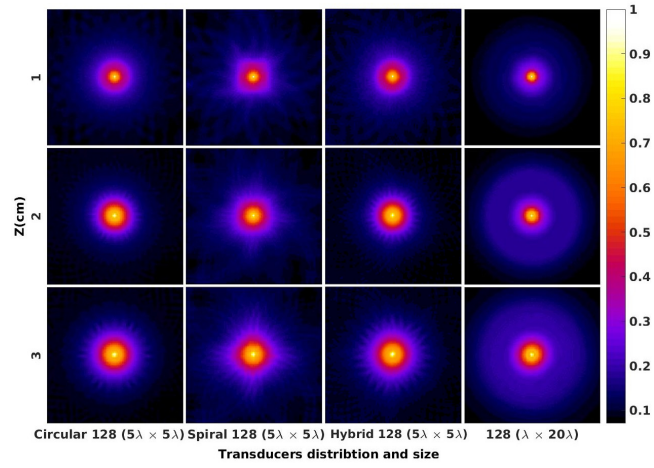
Apart from the sensitivity, sparser geometry might showcase a superior performance in terms of spatial aliasing. As depicted by Figure 4.11b, might not be a good reference for visualization, as compacting the  $10000 \times 10000$  pixels in limited area might suffers from the lack of details. However, the strongest and weakest off-diagonal elements in a bigger scale, respectively belong to the segmented annular circular and the annular circular array, which corresponds to the PSNR values (Table 4.4). The annular circular array can be considered as a set of four concentric rings segmented into sectors with a certain period. Even though this periodicity of the array pattern is lesser than the conventional matrix array, it is still inducing a certain level of grating lobes. The circular deployment of the elements, however, bestrewns the energy of the grating lobes over the FOV, erecting the pedestal side lobes as diagonal band in the vicinity of main diagonal of voxel crosstalk matrix. Meanwhile, due to the peculiar arrangement of the Fermat-spiral, the location of every element is unique and unpredictable, thus the periodicity is minimized and so the grating lobes. As a result, the off diagonal elements are more or less uniformly weighted and crosstalk between the voxels are lesser. The later is also can be inferred from the RMSE and MAE values.

Table 4.4 puts this interpretation into quantitative terms. One can notice that in all the three geometries the RMSE is always higher than MAE by a factor upto 2, whereas for segmented annular, they have lesser differences. These metrics showcase a better performance and lesser error for the spiral annular array owing to the sparse nature of this configuration; yet, among all four, the segmented annular showcases a superior performance with the least error and highest PSNR, even with smaller averaging surface of the transducers. Both the quantitative and qualitative analysis of voxel crosstalk matrix indicate the superior performance of segmented annular array.

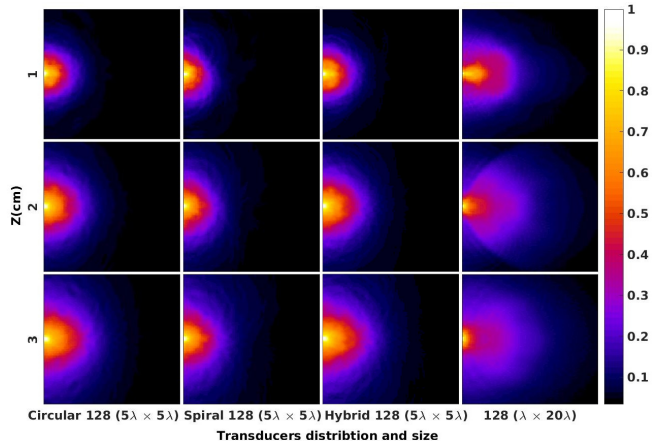
Similar to the previous case analysis, here we also looked into the spatial sensitivity and aliasing of the two central and marginal pixels. It turns out that the most uniform distribution of energy belongs to the aperture with circular annular configuration, but also the maximum sensitivity. The lesser aliasing from sparser geometry was pretty much expected, for both central and marginal case. Figure 4.12b illustrates least and most localized energy distribution for a specific pixel respectively belongs to the segmented annular array and annular spiral array. However, the hybrid strategy seems to ameliorated the trade-off between the aliasing and spatial sensitivity, as is the case for the deeper planes. Yet, the segmented annular array contains less major parasitic contributors than the rest, justifying the quantitative results. Unlike other comparison analysis, the rank of model matrix itself does not handover a straightforward inference. In the first glance, it seems that all the geometries are providing full rank matrix for the VOI. For this reason, we leave the further interpretation to the eigenspectrum analysis of the model matrix. Until now, the eigenspectrum analysis results were in favor of aperture with over all larger element and more projections.



(a)



(b)



(c)

FIGURE 4.12: Qualitative comparison on the effect of the geometrical distribution based on (a) 60 dB sensitivity map, (b) spatial aliasing for the central pixel and (c) spatial aliasing for the marginal pixel. The sparser aperture is, the lesser aliasing but lesser overlapping energy as well.

Such a conclusion applies here as well, where the segmented annular array decays faster than

the rest has relatively weaker eigenvalues (Figure 4.13). The second weakest belongs to the annular spiral array, due to the energy distribution. The annular circular presents the superior performance due to the well arranged structure. The circular array contains large elements and uniform distribution, therefore slower decay with larger contributors (eigenvalues) are expected. The annular spiral and annular circular are composed of same element size, and even bigger aperture. But the associated eigenspectrum are showing faster decay with much smaller component. We believe that this might be due to the minor overlapping between the projections provided by each element in compare to the annular circular aperture.

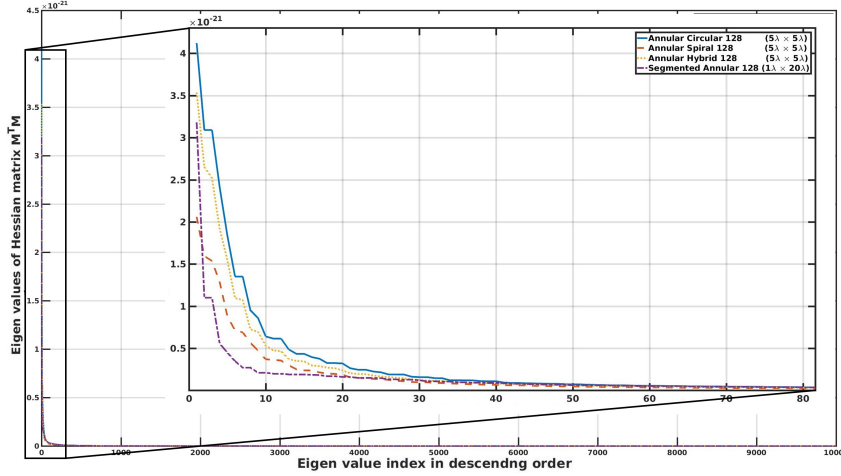


FIGURE 4.13: Eigenspectra of the hessian matrices for the model matrix of four virtual arrays with different configuration. The highlighted regions are magnified for the sake of visualization.

Last but not least, we investigated the capability of these four apertures in effective collection of angular frequency. Similar to Figure 4.10, Figure 4.14 illustrates the spatial Fourier transform of the right singular vectors, from SVD decomposition of their transfer matrix. The Fourier singular vectors basically can be seen as the angular frequency, or the direction of the incoming wave that is visible to the imaging system. Depending on the distance of axial plane (containing the sources) to the aperture (imaging plane), some of the angular frequencies are being filtered, either at low frequencies due to the lack of elements in the center, or at higher frequencies because of limited angular view and acceptance angle (*i.e.* directivity). Just like the segmented annular array which is discussed in Figure 4.10, the annular circular configuration is exhibiting the incomprehensible response to the lower frequency component, for the points close to the aperture ( $1\text{ mm}$ ) and the rest of components are associated with some disparities if not discrepancies. Albeit this property is in favor of filtering the clutters. By analogy to the segmented annular array, both annular circular and annular spiral arrays are containing more robust DC components for the axial planes in the far-field ( $\geq 1\text{ cm}$ ) and comparative number of valuable components, printed next to the white dashed lines. The slightly better performance of spiral array could be due to the slightly larger aperture size, allowing the acquisition of higher frequency components. The ripple structure can be attributed to the non uniform distribution of the elements in spiral configuration. As a conclusion, all these four aperture showed-case a comparative performance, with slightly better functioning for each, depending on the evaluation approach.

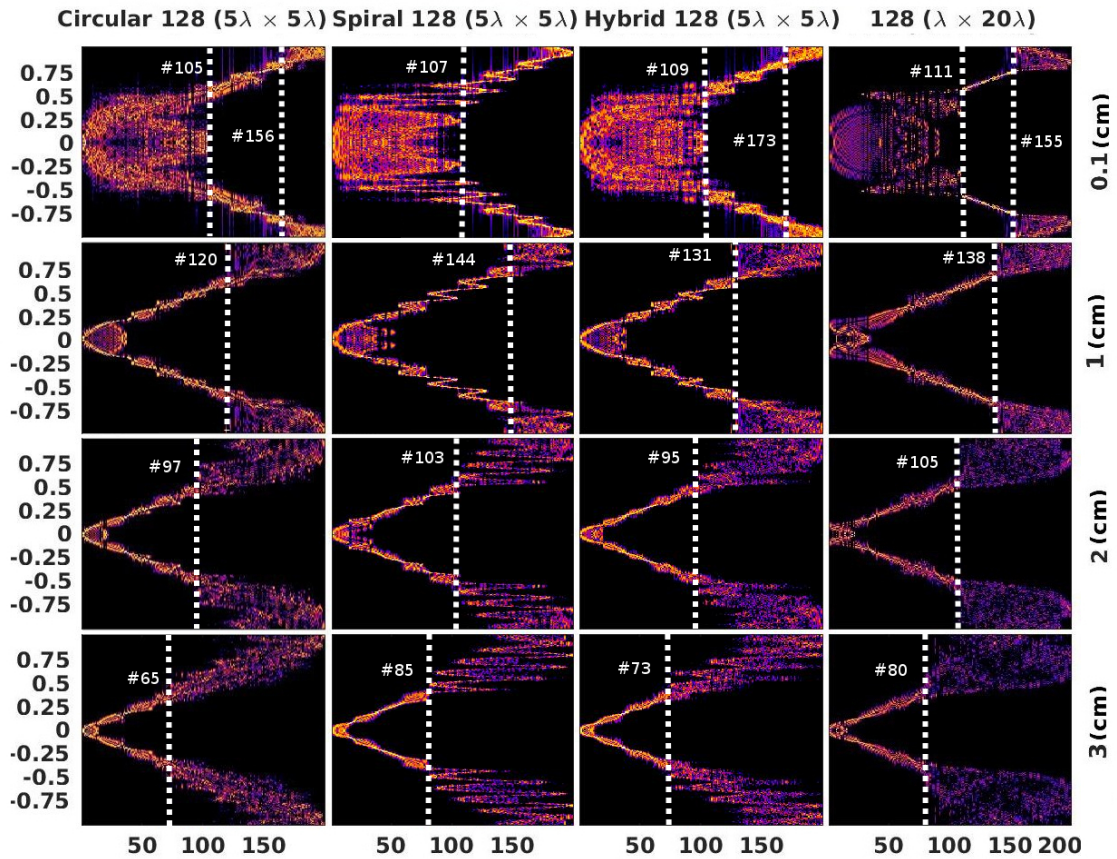


FIGURE 4.14: SVD analysis of the transfer matrix for 200 observation points along the central line at 4 different axial planes away from the aperture. The spatial fourier transform of all singular vectors of the transfer matrix of the aperture. The y-axis is the spatial frequency ( $mm^{-1}$ ) and x-axis is the number of singular vectors happen to be the same as number of control points. If not polluted with the noise, every main singular vector is bounded to a particular spatial frequency. The white dash line is the boundary of the significant singular vectors from the noise with the number pinpointing the degree of freedom for defining the spectral resolution for defining control points.

## 4.4 Conclusion

In this chapter we have applied the concept of voxel crosstalk matrix and eigenanalysis for design and characterization of OPUS handheld probe, in terms of geometrical properties. A set of FoMs for these evaluation approaches have been employed to get quantitative figures for a more robust comparative appraisal. To do all these evaluations, primarily the numeric-discrete-model developed for each of the apertures. Such a model facilitates the performance assessment of the system and further optimization, if required. As the discrete model is sampled with an interval close to the diffraction limit, calculation of cross-talk matrix is an immense effort, specifically for the aperture containing defocused bigger elements ; where every element is considered as ensemble of set of  $\lambda/2$  size sub-elements delayed accordingly. Therefore it is important to not oversample the discretization of the forward model (*i.e.* model matrix) and avoid redundancies. Not to mention that this rule also applies for the calculation of the eigen and singular vectors for the transfer matrix.

Nonetheless, in this chapter we described and employed two pre-reconstruction performance assessment approaches for evaluation of imaging capability of handheld bimodal imaging system. This pre-reconstruction appraisal is indeed important to avoid any biased evaluation due to the merits of reconstruction algorithms. In general a superior performance was accompanied with higher number of elements, larger element size and larger aperture. Yet, there is a trade off between the number of projections and size of the element, or so to say resolution and sensitivity. The agreement can be made by the intercession of geometrical distribution, however for large elements the directive acceptance angle must be compensated. This is happening by the help of negative focusing via convex surface or negative lens. One must be aware of the induced clutter and thereby, manipulate the angular vision such that the blind vision holds for the optically irradiated site. Annular array is expected to improve the volumetric imaging performance of such a bimodality system, thanks to its geometry. The circularly symmetrical response enables the volumetric imaging with uniform energy distribution in the field of view. We demonstrated the avails of the annular probes in the OPUS imaging by elaborating appraisal analysis. The annular arrangement provides additionally a cavity for accommodating the light probe, enabling perpendicular illumination, shortening the optical path to the absorbents and gaining the less skin reflection. Using Monte Carlo simulation, we found that 10 mm diameter of beam width perpendicularly illuminating at the surface of the object provides a desirable fluence. Considering the directivity of the transducers, the annular cavity in the center of the array imposes a blind acceptance angle for 5 mm in front of the housed optical fiber bundle, hence much lower sensitivity for the induced clutter.

After series of simulations and analysis we found similar performance between segment annular, annular circular and annular spiral arrays, with almost equal element size of 20 to 25 mm<sup>2</sup> vibrating surface. The next chapter evaluates the performance of these three geometries in the framework of post-reconstruction analysis. This will further followed by experimental studies in chapter 6 with the help of a single element scanning in a same fashion as the array configuration, such that synthetically it will emulating the proposed array.

### 4.4.1 Perspective

Owing to the frequency response of the transducer, the received OA signal is partially obtained and that takes place with non-uniform amplitude. Consequently the image is reconstructed from a set of incomplete data. To radically address this problem, one way is to pursue a multi-frequency band approached where the information from the edges and boundaries (rapid change in OA signal) of the absorber is expected from the transducer elements with the higher central frequency while transducers with lower central frequency render higher SNR and a better contrast for the main structures (slower change in OA signal). The ultrasonic transducer to a great extent determines the sensitivity, imaging depth, contrast and spatial resolution of this bimodality system.

The frequency spectrum of the induced acoustic waves are governed by the size and shape of the absorbing structure. Yet, much of the frequency band, specifically in the higher frequencies are

being filtered by the bandwidth of the transducer. To tackle simultaneously the aforementioned drawbacks, a dual frequency band annular ultrasonic array can be designed and evaluated utilizing numerical simulations.

The frequency-amplitude dependent distortions and the effect of light propagation can be further incorporated with the model to minimize the quantification errors in the accuracy of deliverable data. Yet the information regarding the medium of interest must be available. As US provides the anatomical map, one can use the map as prior information for optical wave propagation.

Last but not least, this work was inspired by the recent manifestations of CMUT technology in both design and improvement in ultrasound and OA imaging. However, for CMUT technologies, FieldII requires further considerations associated with the physics of CMUT transduction. This effect can be included in the future studies.



# CHAPITRE 5

---

## Post processing algorithm for OPUS, reconstruction and evaluation

---

The eternal mystery of the world is  
the comprehensibility. . .the fact that  
it is comprehensible is a miracle. . .

---

Albert Einstein

### Abstract

In reflection mode imaging systems, the acquisition of multi-frequency data is taking place in space-time domain to pinpoint the underlying structures by forming an image. Two classes of reconstruction algorithms are considered : delay and sum (*i.e.* back projection) and model based. The ultimate aim is to adopt the algorithm to the designed probe, such that the accuracy of the imaging system output maximizes. As the handheld OPUS is far from ideal imaging system, mainly due to the associated limited angle of view, spatial under-sampling and finite element size, the potentials of the reconstruction algorithms in dealing with *no ideal* imaging scenarios are investigated in details. The other intention of the chapter, however, is to conduct an appraisal study on the performance of the array based on the final image. The quantitative assessment of imaging system performance based on the task-based image quality metrics are applied in order to compare the designed probes in providing the high quality image. Our interests are identifying the point spread function of the system, ultrasonic contrast in anechoic regions and minimizing the artifacts.

## 5.1 Introduction



EDICAL imaging in the first place is aimed to obviate the need for dissection the tissue, which traditionally has been practiced to study the relationship between the anatomy, pathology and physiology. The reconstruction and rendering the volumetric three dimensional (3D) representation of the acquired data-set has evolutionary outdated the mental reconstruction from multiple 2D slice projections. In fact, the routine 3D acquisition via clinical scanning technologies has leveraged the importance of volumetric visualization in everyday clinical practice. The main value of the 3D representation is rooted in the fact that biological structures their-selves are 3D objects, therefore rendering in multidimensional fashion facilitates the clinical diagnosis and treatment/surgery planing. Despite the benefits and important advantages of voxel based visualization, it may suffer from the calculation time. The diffraction limit rendering of relatively large volume requires long reconstruction and rendering time. There exists an obvious paradox between the potentials promised by producing high-fidelity images and the

required calculation time for a reliable extraction and interpretation of the information they hold into the quantifiable measures for a better insight with respect to the structure and function of the tissues. This chapter will focus on two methods of the reconstruction algorithm in order to facilitate the productive analysis of the acquired information, including the accurate anatomy and functional mapping to ultimately enhance the diagnosis. Incorporated in these objectives is the quantitative assessment of the output data. Therefore, a post-reconstruction analysis can take place over the final optimized imaged in order to assess the capability of the imaging system. Noteworthy is that the post-processing is only an enhancing step toward human interpretation while at best preserves the amount of information of the received information rather partially losing them. Therefore it is a must to acquire and employ as much as information available, including the imaging system distortion and if possible, investigating medium.

The OPUS image reconstruction, whether model based or those based on analytical solutions like delay and sum back projection (DSBP), are associated with some degree of uncertainties. The model based algorithms are developed upon the propagation of the acoustic waves from emanating voxel in the volume, also known as forward model. Inverting the model to further proceed with image reconstruction can be considered as an inverse problem. This paradigm might be more adaptable to the non conventional arrays and doesn't impose any restriction but incorporates the system behavior. However, the inversion might be tricky and depending on the size of VOI can be computationally inefficient. Meanwhile, the analytical algorithms with promises of exact mathematical formula and numerical stability are mainly developed for canonical measurement aperture with ideal point like shape of transceivers that enclose the entire sample with half wavelength inter-element spacing or infinite line detectors [118]. The imposed constrained by the second type of algorithms make them hardly an appropriate choice for the designed handheld probe. Variety of approaches has been practiced to tackle this problem, among them iterative algorithms [119, 129], adaptive weighting factor [117] and virtual sources [126]. On the other hand, the model based and optimization based reconstruction [18, 96, 161], that is either adapted to the geometry of the system or minimizes the artifacts arose from imperfections in measurement system.

In this chapter our focus is on the post-processing methods required to deliver the optimum output, given a set incomplete measurement of the sparse backward mode OPUS. First and foremost, the deviation introduced by the transfer function of transceiver (AIR) must be alleviated. Then, the maximum achievable projections for ultrasound and optoacoustic imaging will be briefly touched, and on top of that, the optimized DSBP algorithm will be discussed to address the limited number of projection. In order to tackle the constrict of finite element size, two approaches are followed, namely the virtual detector and sub-sampling. The results will be compared with the model based image reconstruction, where the reconstruction is happening by a matrix based deconvolution of forward model from the measured data. The last step involves inversion, and therefore the regularization is compulsory to cope with the artifacts arose from limited number of projections and limited angle of view.

## 5.2 Deconvolution of acousto-electric impulse response

In acoustic linear regime, the received signal can be expressed as the convolution of the sensed pressure ( $x_n$ ) with the transducer's acousto-electric impulse response ( $h_{AIR}$ ). In general, the transducer acousto-electric impulse response acts as a nonuniform band pass filter that distorts the rich frequency information of the optoacoustic signal. Additionally, the axial resolution and image quality in both ultrasound and reflection-mode optoacoustic imaging is being degraded.

$$y(n) = x(n) * h_{AIR}(n) + e(n) \quad (5.1)$$

where  $e(n)$  is the error or noise of the measurement system and is independent to the  $x_n$ . The original signal can be estimated by deconvolution process in order to reverse the effect of AIR, thus the resolution and so the bandwidth can be improved. Given the ill-posed nature of deconvolution, the correct choice of deconvolution technique enables the obtainment of the true signal from the measured output, is a key step prior to the reconstruction. The Fourier division based approaches

are easily implemented and fast but one must be cautious when deals with the signal with low SNR. One way is to weight the frequency content using a window function, within the division process, thus hampering the noise. Yet, due to the band limit detection of the system, it is still not a robust method to higher level of noise, as is the case for both OA and synthetic aperture US. The more rigorous approaches include minimum mean squared error (MMSE) and Wiener filter with comparative performance as both approaches provide the tunable optimization parameter to enhance the retrieving process and increase the robustness to the noise. While Wiener filter minimizes the mean square error between the polluted and true signal by estimating explicitly the spectral power density of the noise, the MMSE is a matrix based deconvolution method in which regularization parameter determines the optimization level by minimizing the  $L^2$ -norm cost function. The given formula for Wiener filter minimizing the minimum square error is given by [120] :

$$G_e(\omega) = \frac{H^*(\omega)S_x(\omega)}{S_e(\omega) + S_x(\omega)|H(\omega)|^2} \quad (5.2)$$

where  $S_x(\omega)$  and  $S_e(\omega)$  are the estimated power spectrum of the signal and noise and  $H(\omega)$  the power spectrum of the AIR obtained by the discrete-time Fourier transform of  $h_{AIR}$ . A powerful alternative, as mentioned earlier is matrix based deconvolution. The convolution step can be defined by matrix multiplication via Toeplitz matrix formation of the convolution term.

$$y(n) = H_{AIR}x(n) \quad (5.3)$$

where  $H_{AIR}$  is the Toeplitz matrix form of the  $h_{AIR}$ . Therefore the deconvolution follows the matrix inversion, with a regularization parameter  $\Gamma$ , for MMSE<sup>1</sup> :

$$\arg \min \left\{ \|Hx(n) - y(n)\|_2^2 + \Gamma^2 \|x(n)\|_2^2 \right\} \quad (5.4)$$

$$\hat{x}(n) = (H^T H + \Gamma^T \Gamma)^{-1} H^T y(n) \quad (5.5)$$

where the  $\hat{x}(n)$  is the estimation of  $x(n)$ ,  $\Gamma = \mathcal{L}\alpha$  is the regularization matrix containing the penalty term  $\alpha$  and  $\mathcal{L}$  is a discrete approximation to derivative operator, imposing smoothness on the solution. The choice of  $\mathcal{L}$  and  $\alpha$  forces  $x$  to be effectively dominated by components in low-dimensional subspace. The penalty term in MMSE determines the level of the noise and the error *w.r.t.* the true signal  $x(n)$ , to further deliver a reasonable solution to ill-posed problems. However at the end of the day, the two deconvolution approaches are interrelated if they be regarded from the singular values perspective [56]. For the SVD based methods  $\mathcal{L}$  is replaced by the identity matrix. Given the regularization parameter  $\Gamma = \alpha\mathcal{I}$ , with  $\mathcal{I}$  being the identity matrix and  $\alpha$  the penalty term, the least square solution can be seek in singular value thresholding such that the thresholded singular value matrix  $S_T$  only contains non-singular elements along its diagonal, given by damped SVD (soft thresholding) :

$$S_{T_{ii}} = \frac{\sigma_i}{\sigma_i^2 + \alpha^2} \quad (5.6)$$

where  $T$  is the threshold value to be the same as the rank. On the other hand, the Wiener filter output  $\hat{x}$ , can be affiliated to singular values by :

$$\hat{x} = \sum_{i=1}^T f_i \frac{u_i^T b}{\sigma_i} v_i \quad (5.7)$$

$$f_i = \frac{\sigma_i^2}{\sigma_i^2 + \alpha^2}$$

---

1. In this very case, when the assumption is zero mean Gaussian for signals, MMSE is equivalent to Tikhonov.

knowing that filter factor  $f_i = \sigma_i S_{T_{ii}}$ , and  $b$  the recorded noisy signal. It might be true that MMSE inherits the merits of ideal Wiener in order to deal with the noise as they are in the same shape [7]. Here we practice the two and for finding the regularization parameter we are employed L-curve [20]. It is known as a robust regularized solution, when the error/noise norm is not known. To simply put, performance of least square minimization problem as a function of penalty term is evaluated via the plot of regularized solution  $\|\Gamma x(n)\|$  versus residual norm  $\|Hx(n) - y(n)\|$  for several penalty terms. Normally the solution is found in the corner value of the plot, where the residual norm is smaller than the error. Yet another popular way to find the penalty parameter with no prior information about the noise level, is the generalized cross validation (GCV) [49]. By minimizing the GCV function, the optimum penalty term promised by GCV,  $\alpha_{opt}$ , is obtained. This is taking place by the help of SVD thresholding. The function is defined to be :

$$\text{GCV}(\alpha) = \frac{\sum_{i=1}^T \left( \frac{u_i^T \delta}{\sigma_i^2 + \alpha^2} \right)^2}{\left( \sum_{i=1}^T \frac{1}{\sigma_i^2 + \alpha^2} \right)^2} \quad (5.8)$$

### Simulation test data

Herein, we practiced the Wiener and MMSE deconvolution for the point source signal detected by an element positioned in front of the source. The signal is corresponded to a micro-sphere of the size  $150 \mu m$  with unity initial inside the micro-sphere and zero elsewhere. For the sake of simplicity the effect of SIR is ignored. The frequency response of AIR is corresponding to the transducer with 5MHz central frequency and 80% fractional bandwidth. The estimation of  $\alpha_{opt}$  for both the GCV and L-curve methods took place by the matlab based regularization toolbox [57]. Figure 5.1 depicts the true optoacoustic signal from the micro-sphere, AIR, recorded signal and the deconvolved signals using Wiener and MMSE deconvolution approach. We added 10dB white Gaussian noise to count for the error in the measurement system and also to test the robustness of each method. We have found similar behavior for the three approaches which is in agreement with our hypothesis stated in previous section. To further asses the performance, we employed

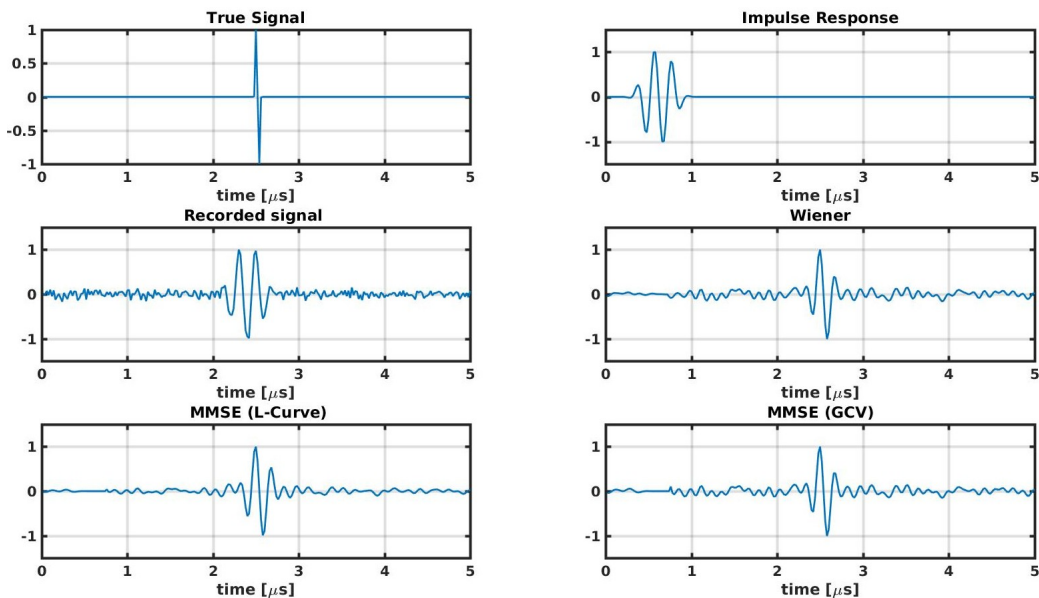


FIGURE 5.1: The effect of acousto-electric impulse response (AIR) on the recorded signal and three method of deconvolution to retrieve the original signal in the presence of -10 dB noise.

the metrics such as cross-correlation to measure the resemblance, PSNR, RMSE and MAE to measure the error *w.r.t.* the original signal. The results are outlined in the Table 5.1 suggesting that for this particular case, the GCV showcases the superior performance with least error and maximum resemblance. However if the noise level increases, as is the case for small transducers

FoM	Wiener	L-curve	GCV
CC	1.398	1.393	1.401
PSNR	16.5	16.4	16.5
RMSE	0.1495	0.1509	0.1490
MAE	0.0654	0.0630	0.0696

TABLE 5.1: Quantitative evaluation of three deconvolution approaches in presence of 10dB noise

and for weak OA signals and synthetic aperture focusing technique (SAFT) ultrasound, the soft thresholding L-curve is not showing a superior behavior. We extended the above approach by adding -10 dB white Gaussian noise. The results are presented in the Figure 5.2. Even though the GCV approaches couldn't completely retrieve the original shape of the signal, yet it behaves relatively better than L-curve and Wiener filter. The shape of the signal is not completely retrieved for any of approaches. The noise level of the GCV is the lowest and visual interpretation from the estimated output is more trivial. GCV showcased a better performance than noise reduction and minimizing the error. The above conclusion is also validated by the proposed metric in quantitative manner, outlines by Table 5.2.

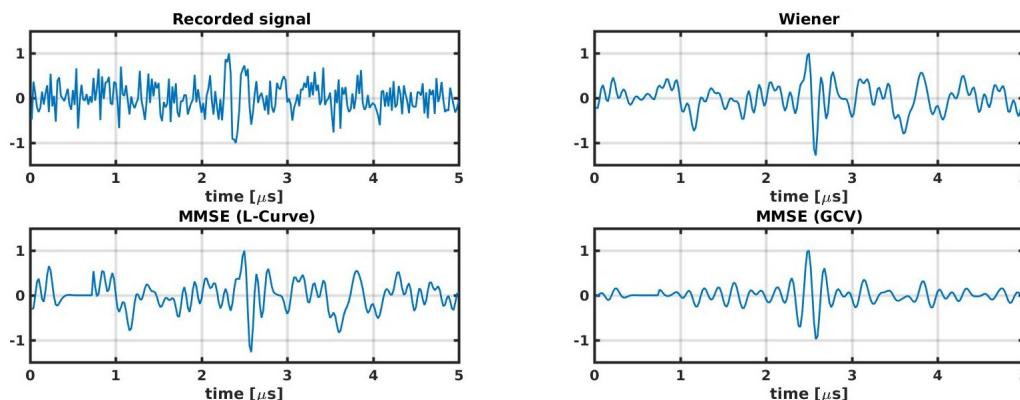


FIGURE 5.2: The comparison between the performance of deconvolution approaches for retrieving the original signal in the presence of -10 dB noise.

FoM	Wiener	L-curve	GCV
CC	1.69	1.7	1.27
PSNR	10.32	10.01	13.65
RMSE	0.3	0.31	0.2
MAE	0.23	0.24	0.12

TABLE 5.2: Quantitative evaluation of deconvolution approaches in presence of -10dB noise

It is indeed possible to apply the hard thresholding with more appropriate result, yet the output signal would be more of the shape of impulse response than the original signal as suggested by Figure 5.3. There exist a trade off between the noise and side lobes which is left to the choice of regularization parameters and holds for the Wiener filter as well. These side lobes might give rise to what is known in the literature as the ringing artifact (Figure 5.4) in the image, where dealing with the artifacts is what deconvolution is aiming at in the first place.

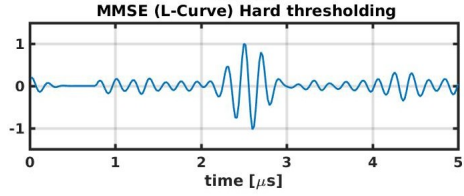


FIGURE 5.3: The performance of MMSE deconvolution approaches regularized by hard thresholding using L-curve in the presence of -10 dB noise.

This side effect specifically affects the boundaries of the absorbing object which is normally containing the high frequency information (due to the expeditious transition). Recalling from chapter 3, we know that the AIR can be incorporated into the imaging operator  $M$  (model matrix) and deconvolution can take place via matrix operations. Although this will be practiced in the model based algorithms, it is noteworthy to mention that the sparsity of the matrix will be decreased and as a consequence, the inversion cost increases. Since the AIR effect is irrespective of source position, the deconvolution can be taken place in a separate step, even for model based algorithms.

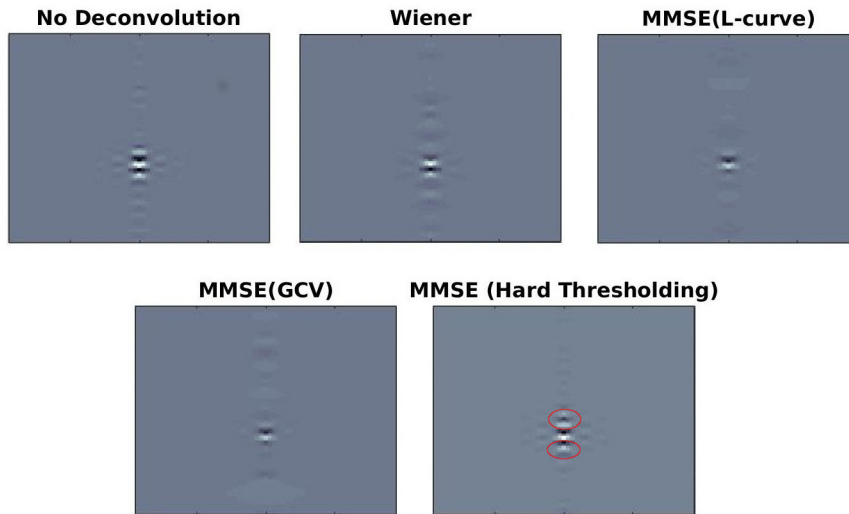


FIGURE 5.4: The comparison between four deconvolution approaches in the reconstructed image. The hard thresholding has lesser value for the lumpy background due to suppression of the noise yet with artifacts indicated by the red circle.

We intuitively conclude that the deconvolution has a direct effect in minimizing the artifact imposed by the measurement system due to the AIR but also noise. Under certain conditions, a signal may be characterized and recoverable from the recorded one completely, if the noise level be low. Therefore the averaging is employed in real case measurements to suppress the noise level. Throughout the rest of the chapter we utilized the MMSE GCV for its superiority and robustness in finding the right trade-off between the estimation of true signal and hampering the noise level.

### 5.3 Method based on the Delay and Sum Back Projection

One major phase of acoustic imaging is the image reconstruction which functions better if the information about the source induction is foretold. To that end, in optoacoustic imaging, a short pulse of laser in the range of nano-second is inducing the broadband acoustic waves out of the targeted chromophores in a simultaneous manner, from acoustics point of view. Meanwhile, in ultrasound imaging, the medium is irradiated by a band limited acoustic wave and the backscattered

waves by the acoustic are partially detected and recorded by the transducers. The irradiation can take place in multiple events with different orientations, thus the number of projections are increasing but also the tangential resolution is improved. On that account, US imaging is advantageous in providing a better resolution. In-fact the number of transmission events can increase up to the number of elements  $N$ , thus providing  $N \times N$  raw signals signals for every transmitter-receiver pair of elements in the array. This technique is known as full matrix capture (FMC) and enables US imaging with factor of  $N$  more projections than OA with analogously one transmit event (induced optically).

Conventionally back-projection (BP) or delay and sum (DAS) methods have been used for reconstruction of both the US and OA images. These algorithms are basically applying the time-domain focusing technique in order to locate the source. Basically for every recorded signal by  $i^{th}$  element, of the wave which might be transmitted by the  $j^{th}$  element or induced otherwise, one can set the intensity of the voxels within the projection with regards to the receiver-voxel pair (or transmit-voxel-receive) time-delay. Then the corresponding time-window of the recorded signal submits the intensity of the voxel. Subsequently, by spatial compounding the projections (for every recorded signal) in a coherent manner a synthetic focusing is taking place. Thus at the focus, back-projected signals are reinforced against the noise and out of focus back-projected signals. Therefore this method is equivalent to the delay and sum on the recorded signals. In fact, under the condition of full tangential view, it is approximately equal to the time reversal operator as one can retrieve the source in the medium from set of recorded signals. To be concrete, let  $s_i(t)$  denotes the measured pressure by the element of the  $N$  element array probe located at  $i^{th}$  position  $r_i$ , with  $i = 1 \cdots N$ . Then the DSBP reconstruction value  $I_k$  for the  $k^{th}$  voxel located would be [76]

$$I_k(r_k, t) = \sum_{i=1}^N w_{k,i} s_i(t + \Delta t_{k,i}) \quad (5.9)$$

where the operation  $\Delta t_{k,i}$  defines the adjusted time-delays for the array to focus at voxel location  $r_k$ ;  $\Delta t_{k,i} = |r_k - r_i|/\nu^2$ . The weighting factor  $w$  supposedly enhances the reconstruction at focused areas and suppress the side lobe levels. Depending on the location of the voxel, whether in the nearfield or far field of the aperture, the back-projection perspective can be altered<sup>3</sup>. As it is stated in chapter 3 equation 3.6, the response of the system to a point source is the alteration to Green's function  $G^H$ , as OPUS is considered as a nearfield imaging *w.r.t.* the aperture. In fact, in the medium at rest where the acoustic reciprocity can be followed, the propagation of a wave emanated from point source located in voxel  $k$  in half-space, with evolution function  $q(t)$  can be defined by

$$p(r_k, t) = q(t) * G^H(r_i, r_k, t) \quad (5.10)$$

Often said that the DSBP does not require knowledge of Green's function as a priori information. This condition is important for the OPUS imaging at the presence of dispersive medium. Nonetheless there are similarities between delay and sum and time-reversal which promises the spatial-temporal matched filtering properties<sup>4</sup>. Even though these similarities might not be so evident on the grounds that the time reversal is not a model based beamforming, while DSBP can be considered as one, on the account of time-delay [35] as is shown in section 5.3.4. Where the time reversal is of interest, the source localization via simulation of wave back-propagation from the array [76] is taking place. It follows the time reversed of signal  $s_i(-t)$ , then the terms in the integral of the equation 3.4 can be restated such that;  $G^H * \partial p / \partial \mathbf{n} - p \partial G^H / \partial \mathbf{n}$ ; for the

2. As for the pulse echo ultrasound, the time of flight for the transmission is also incorporated, thus  $\Delta t_{k,i} = |r_k - r_j|/\nu + |r_k - r_i|/\nu$

3. Albeit in the presence of dispersive/refractive media, the focusing ability of the array would be subjected to the properties of media as well. Our concerns are not involved with these cases as the medium properties for multi-purpose probe is supposed to be not known in advance.

4. The principle of matched filter is analogous to acoustic reciprocity theorem in loss less dispersion free media by considering the fact that the convolution of system impulse response of  $h(t)$  by its inverse  $h(-t)$ , as if the system is fed by the inverse impulse response as input, provides the maximum output at  $t=0$ . In this case back propagating signal in loss less dispersion medium optimally results in constructive interference at the desired time and space.

time reversing. The state terms are further reduced to  $(p * G)$  as can be deduce from equation 3.9. Hence, the time reversed back propagation of the array signals can be stated as :

$$I(r, t) = \sum_{i=1}^N s_i(-t) * G^H(r, r_i, t) \quad (5.11)$$

The weighting function in the equation 5.9 is optimally compensating for the divergence of the wave over the course of propagation, such that at the focus where  $r_k = r$ , the focusing retrieves the original pressure at  $k^{th}$  voxel, where the source is located. By setting the right delays and weighting factor, it can be shown that the process acts as a spatial filter to retrieve the source of pressure wave emanated at specific location. For the aforementioned reason, it follows that the weighting function is taken as  $w_{k,i} = 1/2\pi|r_k - r_i|$  and thus, the backprojection of ensemble of filtered projection can be restated as the convolution of each element's recorded signal with the time-reversed Green's function,

$$\begin{aligned} I_k(r_k, t) &= \sum_{i=1}^N s_i(t) * \frac{\delta(t + \Delta t_{k,i})}{2\pi|r_k - r_i|} \\ &= \sum_{i=1}^N s_i(t) * G^H(r_k, r_i, -t) \end{aligned} \quad (5.12)$$

Hence one can conclude that the DSBP and analytical realization of time reversed back-propagation are demonstrating similar prosperous performance to an identical degree ;  $I_k(r_k, t) = I_{TR}(r, -t), \forall r$ . In another word, Green's function weighted DSBP can be considered as the analytical formulation of time reversal. In fact, the equation 5.12 is closely related to the universal backprojection derived by Xu *et al.* [175] :

$$I_k(r_k, t) = 2 \sum_{i=1}^N \left[ s_i(t) - t \frac{\partial s_i(t)}{\partial t} \right] \quad (5.13)$$

For ultrasound imaging, normally the log compression is used while for OA, the compression, rarefaction, derivative and maximum amplitude decrease are among the choices in order to estimate the source strength [62]. As the OA signals are often noisy, the contrast of the backprojection would be insufficient to recognize the object. Thus a filter is chosen for suppressing the noise. The popular choice of filter is Ram-Lak filter with cut-off frequency  $\omega_c$  in order to roll off the higher frequency components where noise presents.

$$F(\omega) = 4sinc(2\hat{\omega}) - 2sinc^2(\hat{\omega}) \quad (5.14)$$

where  $\hat{\omega} = \omega/\omega_c \in [-1, 1]$ .

Noticeable is that the DSBP is exact only for an infinite linear transducer array and if it is being used, it imposes the certain constricts in the design of the transducer due to its underpinning principles. Firstly, the algorithm does not meant to correct for the diffraction effect over the surface of the transducer as the initial assumption is treating the elements as point source/detector. Secondly, such analytical solution is based on the continuous discretization of the incoming wave-front, which is emanated from the far field (relative to the elements) where the phase shift between the recorded signals are multiple integer of  $\lambda$ . Thence the  $\lambda/2$  interelement spacing is required for keeping the resemblance between the recorded signals which enables the in-phase focusing. The out of phase energy *aka.* grating lobe, will leak to the main lobe energy of the neighboring source and falsifies the estimation of source strength. Further, the type of interference in the summation phase of projections influences the nature of speckle which could be of importance in US imaging. On the other hand, the spatial aliasing artifact would be unavoidable to the degree that the quality of the final image would be severely downgraded. Incorporating the element directivity in the weighting factor of the back projections will attenuate the out of focus contributions, give by [90] :



$$\frac{\cos(\beta)}{|r_k - r_i|^2} H(\beta_{cut}) \quad (5.15)$$

where the Heaviside function  $H(\beta_{cut})$  with cut off acceptance angle  $\beta$ ; such that  $H(\beta_{cut}) = 1$  only when  $(\beta_{cut}) < \beta_{-6dB}$  and 0 otherwise. However, aliasing, undersampling and non uniformly sampling artifacts distort the underlying data and final image quality.

### 5.3.1 Weighted Synthetic Aperture

Traditionally DSBP reconstruction algorithm has been employed for synthetic aperture focusing technique (SAFT), where a large aperture is synthesized by back projecting the sequential measured signals using smaller apertures, in this case receiving elements. The spatial compounding of back projected low-resolution images yields the fully dynamic focused image for all voxels, if FMC is employed. This technique is known to provide the maximum resolution among the DSBP based algorithms. In US mode SA beamforming, a full array acquisition based on individual performance of the transducer elements provides a set of  $N^2$  signals associated with every transmit-receive pairs<sup>5</sup>. All elements are sequentially transmitting acoustic pulse followed by a passive listening to record the echo. The received signals by each element are properly delayed and set of low resolution images corresponding to each transmission are aggregated to form the final raw image.

In this way the full aperture resolution is insured [113] via full dynamic focusing but sacrifices the SNR with depth, as the acoustic pulse excited from a single element. The focusing is performed by introducing the delay time that compensates the differences in round-trip time of flight (or one way trip of OA) from the emitter to the focal point and then to each and every receiver. This approach is also call total focusing method (TFM) for improving angular view while there is a trade-off between number of transmission and frame rate, yet it is possible to decouple the pulse repetition time by sparsifying the number of transmission events at the cost of image resolution. Our interest is to evaluate the designed probe performance based on the final provided image. In order to avoid biased evaluation we disregard the acquisition time and focus our concern primarily on leveraging the image quality. Nevertheless, owing to the lack of elements in the center of the annular probes and its peculiar geometry, SA approach is suffering from low spatial resolution, phase distortion, off axis contributions, low contrast and other artifacts related to the geometry of the transducer. Indeed, it is challenging to tackle all of these factors simultaneously. Aperture weighting technique is being used in pulse-echo (PE) US imaging and improves the contrast at the cost of resolution. This approach is efficient when there is round trip acquisition involved for acoustic wave, yet it is not optimum for OA imaging where there is no control on the transmitted wave. For that reason, we developed a weighted dynamic focusing based reconstruction approach namely, weighted synthetic aperture (WSA), to address the aforementioned defects. We elaborate WSA to estimate the spatial location, size, reflectivity function of the insonified (for PE) or absorption coefficient of the illuminated (for OA) targets for both imaging modalities. The effect of aperture spatial sensitivity into the imaging system is addressed with the spatial impulse response (SIR). The synthetic aperture technique is recognized for amending the lateral resolution but if the requirements are not satisfied, the phase distortion can be introduced where the phase aberration due to the separable delay approximation occurs. An adaptive weighting factor that combines the coherence factor (CF) [63] and phase coherence factor (PCF) [21] is employed to minimize these artifacts.

#### Coherence factors

OPUS is recognized as an imaging system with moderately high coherence between the received pressure between each element. This coherence can be disturbed, if the sampling doesn't take place in a uniform manner. At a given time instance, the produced pressure field within the medium

---

5. In OA mode, same formula applies with a factor of N less summation (no insonification) leading to even lower SNR and higher level of side lobe.

traveling toward the imaging plane can be considered coherent in time and space<sup>6</sup>. The back projection of the recorded signals are pinpointing the source of pressure-field by estimating the maxima in each overlapped region. The coherence between the projections can be stated by the correlation coefficient, a degree of resemblance via otherwise interpretation of van Cittert-Zernike theorem [101] which yields a coherence-based metric named coherence factor (CF) [63]. Therefore, estimating the resemblance between recorded signals (or equivalently the projection voxels) is directly proportional, if not identical, to assessing the spatial coherence of the ultrasonic field and vice versa.

CF is an adaptive weighting factor known to be effective in minimizing the aberration and side lobe level. It is defined as the ratio of coherent sum (*i.e.* focal point) to the total incoherence sum of the signal intensity (*i.e.* off axis contributions) across the aperture. On the other words, the intensity of coherent sum is much lower for side lobes and other aberrations. For the imaging artifact suppression and image quality enhancement, coherence factor CF is weighting the envelop of the raw signals as follow :

$$CF(t_k) = \frac{\left| \sum_{i=1}^N S_i(t_k) \right|^2}{N \left| \sum_{i=1}^N S_i(t_k)^2 \right|} ; \quad CF \in [0, 1] \quad (5.16)$$

where  $r_{i,k} = \sqrt{(x_k - x_i)^2 + (y_k - y_i)^2 + (z_k)^2}$  is the distance of the  $k^{th}$  voxel located at  $x_k, y_k, z_k$  coordinate, to the  $i^{th}$  transmitting or  $j^{th}$  receiving element and is corresponding to the time of flight  $t_k = \sqrt{(r_{i,k})^2 + (r_{j,k})^2} / \nu$ .

During the coherent summation phase, the out of focus regions are associated with the phase distortion. Therefore there would be the misalignment between troughs and peaks of the signal projections while at the focus perfect alignment is expected. The phase distortion is less experienced by the incoherent summation as troughs are turning into peaks due to the square factor. At the absence of distortion, in-phase summation between projections leads to optimum focusing, indicated by 1 for CF value. The value is calculated for every voxel within the medium and is incorporated in the weighting factor of equation 5.9 via dot product in order to enable the focusing error depletion. Nonetheless, this amplitude based weighting approach is vulnerable to the noisy data and is lesser efficient with lower SNR signals [112], as is the case for US-TFM and OA signals.

A more robust factor is proposed by Li *et al.* by further elaborating the numerator in 5.16 by excluding the spatial frequencies subjected to the out of phase contributions and phase distortions [92]. In their paper, they have shown that its only the low-spatial frequency components of the received aperture is contributing to the coherent summation, once again showcasing the superior performance of the larger aperture in defining the objects. As a result the coherent summation is penalized further to smaller region, increasing the in- focus estimation. However this methodology is strictly defined for the conventional linear arrays and might not perform well with sparse geometries, where the energy of aperture is not necessary accumulated in the lower frequencies. Albeit, with further adaptation toward the geometry of designed probe might rivals its competence, yet depending on the aperture, the adaptation might differ and again lead to an unbiased evaluation.

Alternatively, Camacho *et al.* proposed PCF [21], an adaptive weighting factor based on the phase variation between beamformed received signals of individual elements. After the time of flight is compensated for the received RF signals, the phase dispersion for each time point (voxel) is calculated. The PCF matrix constituent thus composed of weighting factors of values between zero and one, associated with the calculated standard deviation in the phase  $\sigma_\phi$ . At the focus (on-axis), the standard deviation between the echos are zero since they are in phase, thus the weighting factor corresponds to the maximum. However, the out of focus contributions, including the grating lobes, are not always in phase with the ensemble signal. Thus such an effect rises the

---

6. Depending on the nature of medium the, incoherence might increase. This is the case for example at the presence large number of randomly distributed scattering objects.

standard deviation associated with decline in the PCF value :

$$\text{PCF}(t_k) = \max \left[ 0, 1 - \frac{\sigma_{\phi_{t_k}}}{\sigma_0} \right] ; \quad \text{PCF} \in [0, 1] \quad (5.17)$$

$$\sigma_{\phi} = \sqrt{\frac{1}{N} \sum_{i=1}^N \left( \phi_i - \frac{1}{N} \sum_{i=1}^N \phi_i \right)^2}$$

where  $\sigma_0$  is the nominal standard deviation for a uniformal phase distribution  $(-\pi, \pi]$ .

### Spatial impulse response

Another, yet important factor that affects the spatial resolution of the measurement system, is the effect of acquisition system (aperture) into the measurement. Due to the finite size of the element, the tangential ( $\simeq$  axial) resolution is degraded. This degradation is rooted in the deterioration of spatio-temporal frequency of the incoming pressure wave, while its being recorded. The spatial frequencies are degraded due to the finite size of the aperture while the temporal frequencies are weighted to lower components because of the averaging over the surface of elements. The former can be incorporated into the image reconstruction algorithm by employing the transducer spatial impulse response (SIR) as a weighting factor. When this spatio-temporal frequency parameter convolves with the transducer impulse response, it defines the behavior of the emitted wave as well as frequency dependent spatial sensitivity of the transducer, associated with the finite dimension of the aperture. this property has been investigated in chapter 4 section 4.2.2. By employing the inverse scaled SIR as an adapting weighting factor, the isotropic sensitivity is ensured. As for the US-SAFT, there is N-map calculation required for every transmit-receive response of the transducer in compare to only one-map calculation for the OA, which defines only the spatial dependent response of the aperture. The response of the OA source is not to be estimated and remains unknown.<sup>7</sup>

As this SIR based factor is the property of the array's elements and can be computed before hand, it is not affecting the processing time required for the reconstruction. Therefore the final reconstructed data is adaptively weighted by a factor which is the compilation of SIR, CF and PCF as the weighting factor. Then the weighted intensity (WI) values would be :

$$\text{WI} = \langle \text{CF}, \text{PCF}, \text{SIR}, \text{I} \rangle \quad (5.18)$$

where  $\langle \cdot, \cdot \rangle$  is the inner product notation.

While each of these factors independently addresses specific problem, the simultaneous improvement in contrast and side-lobe reduction, because of CF, enhancement of lateral resolution along with suppressing the side lobe and grating lobes levels, mainly because of PCF contribution and finally isotopic sensitivity as well as ameliorating the dynamic range, owing to SIR, is expected by compiling the aforementioned factors [78] rather than standalone.

### 5.3.2 Comparison of weighting factors and their effect in DSBP

A forward looking annular array of 128 elements ( $\lambda \times \lambda$ ) operating at 6 MHz center frequency with 80 % fractional bandwidth has been modeled for OA and PE synthetic aperture imaging. We performed numerical studies to evaluate the effect of weighting factors. Multiple point reflectors (for US) and point sources (for OA) are positioned in the medium as a measure of point spread function of the system, in order to investigate the quality of the reconstructed image using various weighting factor. The volume of imaging was 40 mm axially and 15 mm in lateral and elevation.

<sup>7</sup>. Indeed the optoacoustic impulse response is object dependent. If the prior information is know, then one can incorporate it to the reconstruction for a task based performance analysis, under the assumption of uniform heat deposition. In fact, for a short laser pulse induction, it has been found to be the 1<sup>st</sup> order derivative of the pulse temporal shape in three dimension [34].

After SAFT beamforming, the data are weighted with different adaptive weighting, including CF, PCF, CF plus PCF, CF plus PCF and SIR (WSA) respectively. The US result is presented in Figure 5.5 showcase that CF weighting is improving the image quality by removing the artifacts mainly due to the geometry of the transducer, but it is actually PCF that is successfully hampering the side-lobes and suppressing the grating lobes. Moreover PCF narrows width of the main-lobe due to its ability of exact estimation for the focal point. In fact, it is the combination of CF and PCF that improves the result to a great extent by adaptive weighting the unwanted features. Yet there is room for enhancing the image by incorporating the properties of transducer into the reconstructions algorithm. As the response of the aperture is spatially variant, the quality of the signal in terms of frequency and amplitude content is highly governed by the objects location with respect to the transducer. Consequently beamforming is not the ultimate solution in providing the best image. Thus an inverse-SIR mask is weighting the image additionally to increase the dynamic range and to counteract the effect of aperture, leading to isotropic sensitivity regardless of the position of objects.

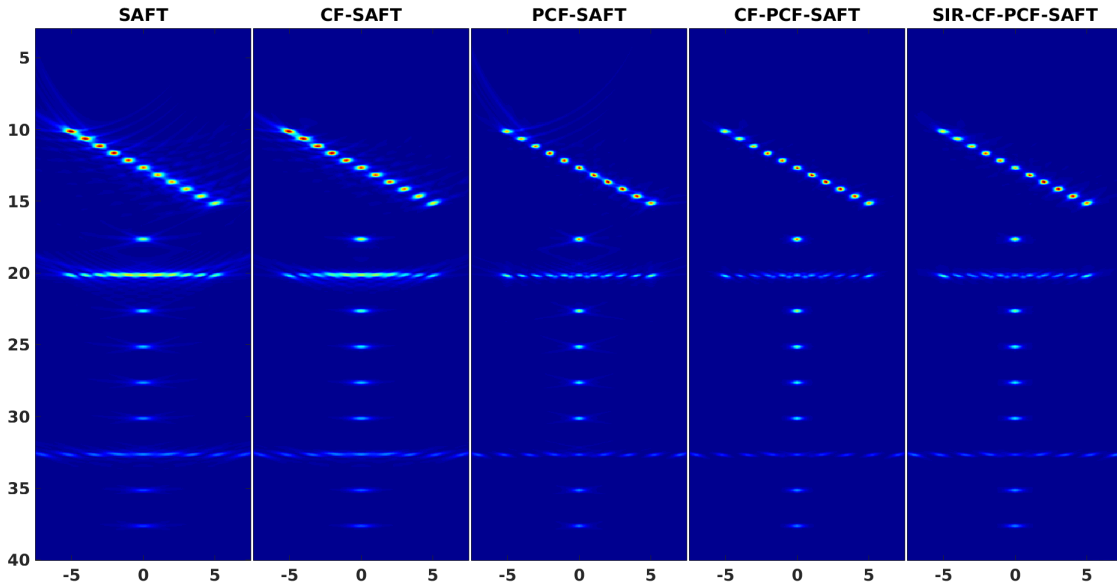


FIGURE 5.5: Ultrasonic B-mode images of point targets, reconstructed using SAFT algorithm. From left to right : no weighting, weighted with CF, PCF, CF+PCF, CF+PCF+SIR (WSA) mask.

On the grounds of quantitative analysis, Figure 5.6a provides the lateral logarithmic profile of the point spread function of single reflector situated at the depth of  $27mm$  away from the transducer. It shows the advantage of using adaptive weighting in shrinking the main-lobe width (-6dB) by factor of 2 and suppressing the side lobes by 25 dB. Figure 5.6b is the logarithmic profile of the point targets at the depth of  $32mm$  and demonstrates the ability of isotropic reconstruction after applying the SIR mask.

Although PSFs are an indication for imaging system resolution, their interpretation remains intuitive. The imaging performance of US system for soft tissues where the diffusive scattering are the dominant effect requires further evaluation. One of which, anechoic cysts are standard approach for assessing the US imaging performance. Figure 5.7 shows the effect of weighting factors by depicting the 60 dB dynamic range of three simulated  $3mm \circlearrowleft$  cyst, located at the depth of  $20mm$ . In order to quantify the enhancement, the contrast to noise ration (CNR) of each

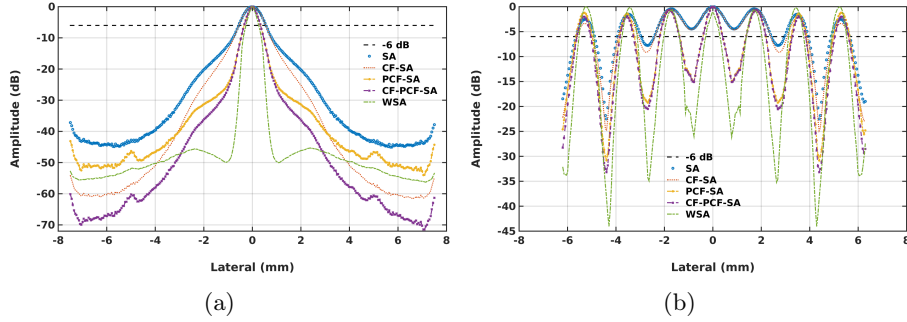


FIGURE 5.6: Logarithmic profile of the scatterers (a) at the depth of 27 mm and (b) at the depth 32 mm away from the transducer, weighted with different weighting factors.

image has been calculated, using the following formula :

$$\text{CNR} = \frac{\langle S_{\text{lesion}} \rangle - \langle S_{\text{BG}} \rangle}{\sqrt{\sigma_{\text{lesion}}^2 + \sigma_{\text{BG}}^2}} \quad (5.19)$$

where  $\langle S \rangle$  and  $\sigma$  are the mean and standard deviation of the logarithmic image. The received signals from the speckle region is dominated by the main-lobe signal while the value of the anechoic cyst is polluted by the side lobes and grating lobes, leaving more room for weighting factor for rectification. Qualitatively, the cysts are barely visible with SA beamforming, and CF weighted SA, while PCF showcases a much better amelioration in suppressing the parasitic signal in anechoic regions. What SIR does is escalating the energy for lower sensitive regions of the array with minimal effect on CNR yet isotropic. It is worthy to mention that the dark pits in the speckle regions are more due to the randomness of speckle rather than the incoherence in spatial compounding, and can be rectified by denoising technique by counting for speckle statistics within the wavelet thresholding paradigm [41]. Therefore the region is weighted much lesser than that purely anechoic regions.

On the other hand, comparing to the ultrasound PE, in reconstruction of optoacoustic images only  $N$  (number of receiving elements) detected signals are available, leading to a higher level of side lobe. Moreover, the spatial impulse response of the optoacoustic source is not measurable and the final image can only be compensated with the properties of the transducer in reception mode, depicted in Figure 5.8.

Even so, a dynamic range of 40 dB for a single OA point-source at the depth of 27 mm away from the transducer is manifested in Figure 5.9a using WSA, the main lobe width is narrowed by 1.8 fold, leading to a better lateral resolution. The importance of this approach is getting more noticeable where in optoacoustic imaging, point-sources are more detectable regardless of their spatial location, consequently a step closer toward the isotropic sensitivity is taken. This achievement though is coming with a minor drawback in which, reconstruction artifacts are visually more prominent since the energy compensation treats the image features equally. Specially, when it comes to the adjacent multiple point sources, the methodology might not be so successful in separating two neighboring points as illustrated by Figure 5.9a. This is partially due to the diffracting effect over the finite surface of the transducer. Nonetheless almost 20 dB dynamic range improvement in compare to CF-PCF, demonstrate the advantage of using WSA for optoacoustic imaging using annular geometry.

Figure 5.10 shows the result of weighting factors applies on the DSBP reconstructed of a  $3\text{mm} \odot$  cyst like active circular region<sup>8</sup>. For normalized images, qualitative evaluations are suggesting that the compiled adaptive waiting factor succeed to suppress the artifacts to half of their original values ( $\simeq 0.25$ ).

8. The illumination assumed to be uniform and effect of light propagation has been ignored.

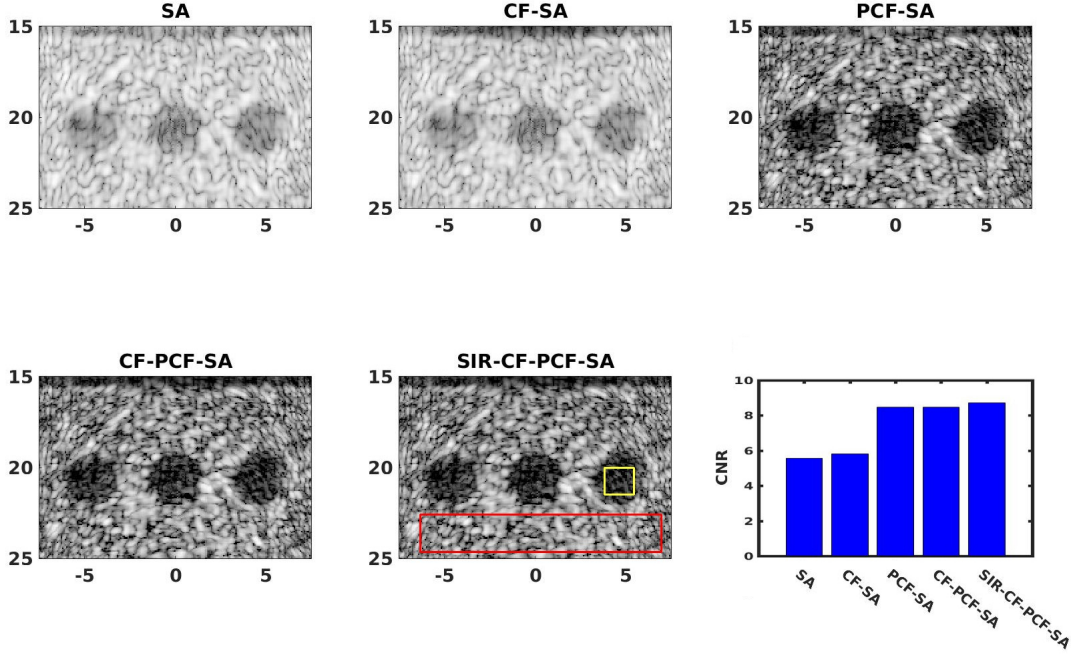


FIGURE 5.7: The effect of weighting factors in ameliorating the contrast of anechoic cyst of 3 mm  $\varnothing$  and plot of their CNR values. The B-mode images are simulated with FMC approach and reconstructed with SAFT technique. The yellow and red frames are indicating the areas have been used for calculation of the CNR.

### 5.3.3 Virtual element

Although the temporal averaging of the pressure waves over the surface of the elements might be in favor of SNR of the recorded signal, it applies higher weighting on the higher temporal frequency components as well. One possible way to deal with this situation is to employ the concept of virtual source.

For the array with negative focusing elements, either by the help of convex surface or negative lens, WSA can be employed in such a way that the time delay corresponds to the focal point behind the elements, where the virtual point source / detector is considered. This approach has better conformity with the traditional assumption of ideal point-like elements. The convex element might be a better option than negative lens in terms of avoiding attenuation of the lens material and reverberation effect. Yet there are limitation associated with the curved surface of a convex element in order to achieve  $60^\circ$  acceptance angle. Very recently, Drozdov *et al.* [36] challenged the previous assumption of uniform sensitivity over the active surface of convex transducer. Using stationary phase method concept, they showcased that sensing of the higher frequencies of the emanated wave is conditioned to tangential intersections between incoming wave. In another word the contribution of higher frequency in recorded signal is limited to the DC components of the spatial frequencies. In a way it is congruent to the directive vision of the elements for the higher frequencies. To abide the aforementioned constrict on geometrical design of the convex element, the following formula has been proposed [36] :

$$ROC_{tr} = \frac{\max |r_k - r_i|}{\max |r_k - r_i| / \Omega_R - 1} \quad (5.20)$$

where the  $\Omega_R$  is the active surface of the element and  $ROC_{tr}$  is the radius of the curvature, the distance between the actual and virtual element. Then the time-delay in the equation 5.13 can be simply compensated by adding  $ROC_{tr}/\nu$  to the time  $t$ . Therefore for a transducer with active surface of  $5\lambda$  corresponding to 5MHz central frequency expecting a signal from 30mm depth,  $ROC_{tr}$  of 3mm is expected. While in practice, the transducer with such a radius of curvature requires

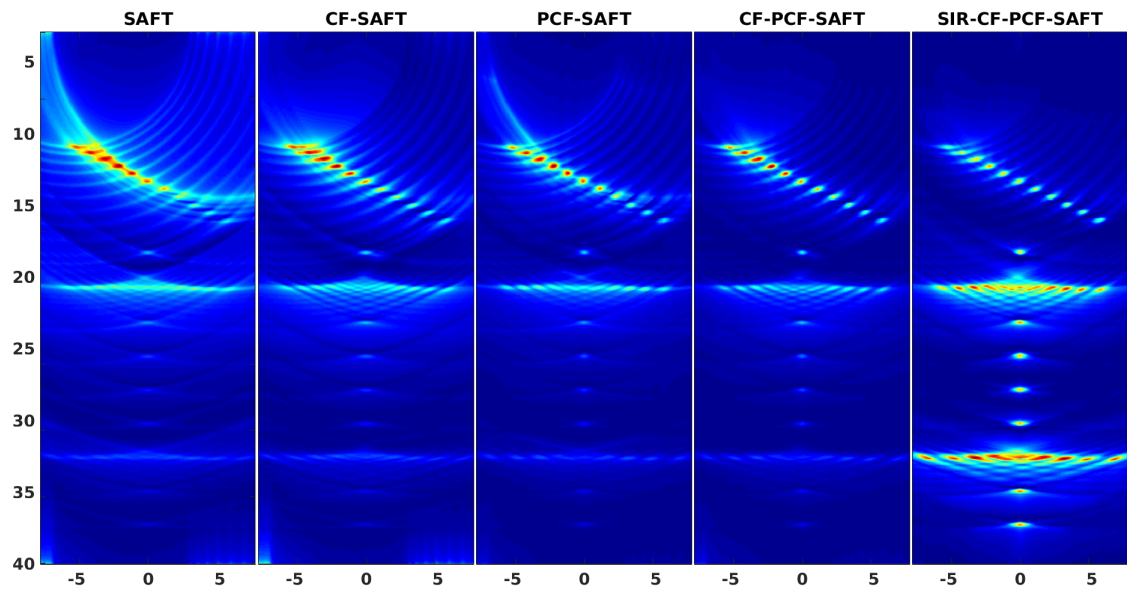


FIGURE 5.8: Optoacoustic SA images of the simulated phantom of the point targets. From left to right : with no weighting, weighted with CF, PCF, CF+PCF, CF+PCF+SIR (WSA) mask.

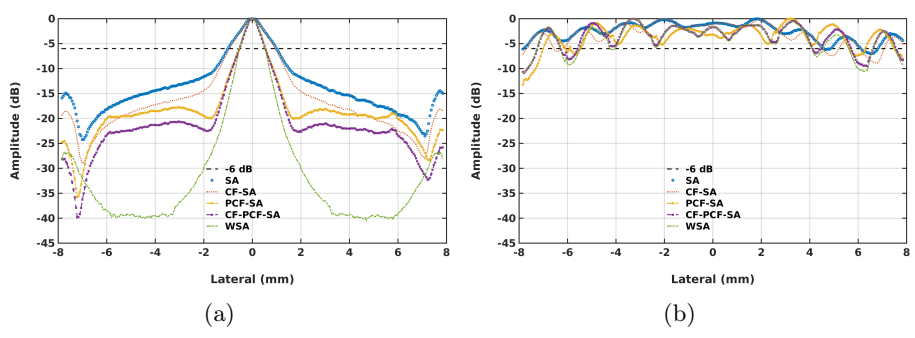


FIGURE 5.9: Logarithmic profile of the point sources (a) at the depth of 27 mm and (b) at the depth 32 mm away from the transducer, weighted with different weighting factors.

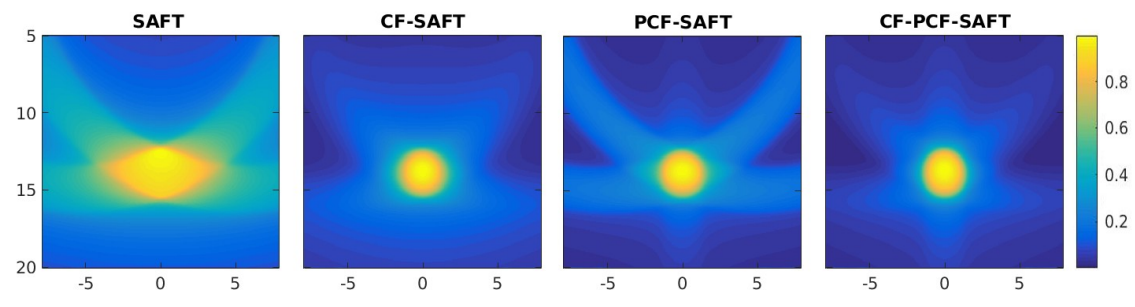


FIGURE 5.10: Optoacoustic 2D slices of SA images of the simulated active sphere at  $y = 0$ . From left to right : with no weighting, weighted with CF, PCF, CF+PCF, WSA mask.

complex micromachined technology with miniature subelements to avoid distortion and low pass filtering. For our simulation we ignored these side effects and for the experimental measurement, we adapted the concept of virtual element toward the condition negative lens is employed. The time delay must be adjusted in a way to compensate for the higher speed of sound in the lens and its spherical shape.

The time  $t$  in the equation 5.13 therefore is altered by the defocused lens with radius  $r_L$  and speed of sound of  $\nu_L$ , can be realized as :

$$t_L = t_d(\beta) \left[ \frac{|r_k - r_i| - r_L}{\nu} + \frac{r_L}{\nu_L} \right]; \quad (5.21)$$

where  $\nu_L > \nu$  is the speed of sound in the lens. For a wide angle of view, the  $R_L$  and material of the lens should be chosen carefully in order to meet the required  $60^\circ$  for  $\beta_{cut}$ . Finally to compensate for the time differences imposed by the negative lens, the equation 5.15 can be tailored to :

$$\frac{\cos(\beta)}{d_{neg}(\beta)|r_k - r_i|^2}$$

The  $t_d(\beta) = 10^{-\beta}$  and  $d_{neg}(\beta) = 1/(1+0.03\beta)$  are respectively the time delay and directive factors given by reference [90].

### 5.3.4 Matrix representation of DSBP

The time domain DSBP can be represented by matrix formalism. This feature allowed us to perform a direct comparison with the model based algorithm which is defined in the next section. Considering  $I$  as the estimation of the true voxel intensity of the investigating object, for  $K$  number of voxels. Then DSBP can be reformulated by concatenating the recorded raw signals into the vector  $S$  and defining the weighted index (based on time-delay) sparse block multi-diagonal matrix  $T$ , for  $\tau$  applied on the  $i^{th}$  received signal such that

$$I = \begin{bmatrix} \tau_{(1,k)} & & & & 0 \\ \vdots & \tau_{(1,k)} & & & \\ \tau_{(N,k)} & \vdots & \ddots & & \\ & \tau_{(N,k)} & & \tau_{(1,k)} & \\ & & \ddots & \vdots & \\ & 0 & & \tau_{(N,k)} & \end{bmatrix} \begin{bmatrix} s_1 \\ s_2 \\ \vdots \\ s_i \\ \vdots \\ s_N \end{bmatrix} = T^T S \quad (5.22)$$

where  $\tau_{(i,k)}$  is the delay corresponding to the voxel  $k$  in the VOI.  $I$  is a vectorized matrix of the length equal to the number of designated voxels and needs to be reshaped to form the image, bearing in mind that here  $T$  acts as a parallel dynamic focus beamformer for every voxel within the VOI.

### 5.3.5 Matched filter interpretation

The matched filter is hold for the case that the model matrix can be considered as the transfer matrix. This has been proven for the case of time reversal [149], where the reciprocity holds for the transfer matrix. By back propagating the recorded signals by matrix convolution in loss less, dispersion free medium optimally constructive interference at the desired time and space is achieved. The model designed for the DSBP, where the transfer matrix is replaced by the weighted time delay  $T$ , might possess this salient feature only if  $T \approx M$ , where the maximum intensity is given by  $M_i^T S^9$  is be equal to the  $T_i^T S$ , an indication for the robustness of the approach.

---

9.  $i^{th}$  column of the model matrix  $M$



As a matter of fact, the transposed matrix is equivalent to the time reversal operator [149]. Then the matched filter guarantees that for all focus points the maximum intensity is achieved by backprojection, in a concurrent manner. Where the known signal is polluted, matched filter promises to maximize the SNR by incorporating the error covariance matrix  $C_e$  such that ;

$$I = T^T(MO + e)$$

$$T \propto C_e^{-1}S$$

where  $O$  is the investigating object. Therefore SAFT-DSBP is optimized for SNR. The success of the adaptive weighting factor approach can be estimated by comparing the result with the matched filter.

## 5.4 Focusing as an inverse problem

The analytical reconstructions like DSBP manipulate (in amplitude and phase) the recorded data toward the straightforward mathematical assumptions that algorithm is based upon. Essentially DSBP neglects the aperture properties as its underpinning assumptions are far from the properties of the proposed arrays in chapter 4. As a result, the final image accuracy is compromised. In previous section, a methodology have been proposed to incorporate the aperture information as prior knowledge via adaptive weighting factor. However the degree of successful of the approach is left to be assessed by model matrix operator. As the model matrix itself contains the inherent properties of the aperture, theoretically it can provide the optimum estimation of each voxel contribution. Using the model that accommodates the detailed physical phenomena of the recording process, one can see the reconstruction as a canonical least square estimation to inverse problem "  $\|Ax - b\|$  ". However majority of inverse problems solutions are violating the last *Hadamard's* condition *w.r.t.* stability of the output data to the perturbations. Further improvement of the reconstruction accuracy is possible by incorporating the error statistic as prior knowledge of the data into the reconstruction :

$$Mo = y, \quad y = Mo^{exact} + e \quad (5.23)$$

where  $o^{exact}$  is the exact image to be reconstructed and  $y$  is the recorded data. Assuming that  $M$  is invertible, then the naive solution  $o^{naive}$  would be

$$o^{naive} = M^{-1}y = o^{exact} + M^{-1}e; \quad (5.24)$$

However, a heedful consideration reveals that the reconstructing process is far from exact recovery of the true object, for the acquisition system introducing thermal noise to the incomplete measured data (limited angle). Therefore the condition number in matrix  $M$  would be large (ill-posed) such that ;  $\|M^{-1}e\| \gg \|o^{exact}\|$ , so hiding the  $o^{exact}$  among the inverted errors. In order to mitigate such contamination, the regularization must be imposed in order to reduce the sensitivity of the solution to error to compute a stable solution. The importance of regularization has been already discussed. For example equation 5.5 necessarily introduce the Tikhonov regularization into the least square solution, by balancing the fitting term or penalty term and the smoothness parameter that is a measure of favorability for the solution.

Yet another way of regularization is the regularization by projection in a way that the solution to the least square is restricted to lie in a low dimensional subspace (sparsity)<sup>10</sup>. In another word, it means that a large components of exact solution  $o^{exact}$  is lying in the low dimension subspace. Theoretically the subspace  $\mathcal{W}_\kappa$  spanned by vectors that represent the desirable features for regularized solution. If known, the subspace can be constructed in a way to represent the prior knowledge. Among particular examples of this sort, is the truncated SVD, where the  $\kappa$  dimension subspace is the space spanned by the first  $\kappa$  right singular vectors  $v$ .

$$\text{TSVD} : \mathcal{W}_\kappa = \text{span} \{v_1, v_2, \dots, v_\kappa\};$$

---

10.  $\|Ax - b\|_2$  is subjected to  $x \in \mathcal{W}_\kappa$

Assuming that the matrix  $W_\kappa = (w_1, w_2, \dots, w_\kappa) \in \mathbb{R}^{n \times \kappa}$  is given such that  $\mathcal{W}_\kappa = \mathcal{R}(W_\kappa)$ <sup>11</sup>. Knowing that the solution exist in the aforementioned subspace with the requirement  $o = W_\kappa z$ , the regularized solution can be expressed as projected problem :

$$o^{(\kappa)} = W_\kappa z^{(\kappa)}, \quad z^{(\kappa)} = \arg \min_z \|(MW_\kappa)z - b\|_2. \quad (5.25)$$

For small  $\kappa$ ,  $MW_\kappa$  can be explicitly calculated to solve the projected least square problem in the desired subspace. The advantage of SVD basis is that it can adjust itself to the problem explicitly by accommodating to matrix  $M$ , but there are limitations associated with SVD, including the computational cost. Additionally, SVD doesn't incorporate the information about the right hand side  $y$ . Bear in mind that the goal is to incorporate as much as prior information as possible, for example the noise information.

In the pursuit of a more comprehensive subspace, yet computationally attractive *Krylov* subspace comes to our rescue, defined as :

$$\text{Krylov} : \mathcal{K}_\kappa = \text{span} \{M^T y, (M^T M)M^T y, (M^T M)^2 M^T y, \dots, (M^T M)^{\kappa-1} M^T y\},$$

Krylov subspace with maximum  $\kappa$  dimension is adapting itself fully to the case in hand by incorporating the information of both quantities  $M$  and  $y$ . In another word the solution is bounded to maximum  $\kappa$  iterations, starting with lowest frequency component toward the highest but stop right before the inverted noise contributes. In principle one need orthonormal basis for the sake of numerical implementation. The vectors  $(M^T M)^i M^T y$  in the above equation prone toward the main right singular vector of  $M$  which in practice are more and more linearly dependent.

$$p_i = \frac{(M^T M)^{i-1} M^T y}{\|(M^T M)^{i-1} M^T y\|_2}$$

$$p_i \rightarrow \nu_i \text{ as } i \rightarrow \infty$$

To cope with, modified Gram Schmidt orthonormalization<sup>12</sup> time or Lanczos bidiagonalization process can be applied on matrix  $M$  with starting vector  $y$  in order to produce orthonormal basis for vectors for subspace  $\mathcal{K}_\kappa$ . However, there are rooms for expediting this approach by bypassing the required steps for the explicit formation of subspace  $\mathcal{K}_\kappa$  and further orthonormalization. Let us acknowledge that the linear least square functions are associated with so called normal equations of the form  $M^T M o = M^T y$ ; with  $M^T M$  being a Hermitian positive semi definite matrix of  $M$ . This property allows us to employ conjugate gradient (CG) for solving the least square problem. By applying  $\kappa$  steps of CG of iteration on the normal function, the  $o^{(\kappa)}$  will be realized. The algorithm can be written in the form of as follows :

Let  $o^0 = 0$  be the staring vector,  
 $r^0 = y - M o^0$  the first residual,  
 $p^0 = M^T r^0$  the initial search vector

```

1: while  $\|o^{(\kappa+1)}\|_2 \geq \|o^{(\kappa)}\|_2$  do
2:   while  $\|r^{(\kappa)}\|_2 \leq \|r^{(\kappa-1)}\|_2$  do
3:     for  $\kappa = 0, 1, 2, \dots$  do
4:        $\xi^\kappa = \frac{r^{\kappa T} r^\kappa}{p^{\kappa T} M^T M p^\kappa}$ ,
5:        $x^{\kappa+1} = x^\kappa + \xi^\kappa p^\kappa$ ,
6:        $r^{\kappa+1} = r^\kappa - \xi^\kappa M^T M p^\kappa$ ,
7:        $\zeta^\kappa = \frac{r^{\kappa+1 T} r^{\kappa+1}}{r^{\kappa T} r^\kappa}$ ,
8:        $p^{\kappa+1} = r^{\kappa+1} - \zeta^\kappa p^\kappa$ 
9:     end for
10:   end while
11: end while

```

11.  $\mathcal{R}$  indicates the regularization via projection, damping low and reconstructing high frequencies

12. GMS is an expensive procedure as for each iteration, the reorthogonalization is practiced

The last condition is implying the stopping criteria.

Worthy of mention is that the search vectors are equivalent to *i.e.* the power iteration of  $M^T M$  which are basically the basis of Krylov subspace. The most stable variant of CG is known as conjugate gradient least square algorithm (CGLS) [55], in that the explicit formation of  $M^T M$  is avoidable. Recalling that  $M$  is ill-conditioned,  $M^T M$  will have the squared condition number of  $M$ , meaning that the CG convergence would be extremely slow to round off the errors. In CGLS algorithm we can introduce the updating functions such that in each iteration only two separate matrix-vector multiplications with  $M$  and  $M^T$  take place.

$$\xi^\kappa = \frac{r^{\kappa T} r^\kappa}{(Mp^\kappa)^T (Mp^\kappa)} \quad , \quad r^{\kappa+1} = r^\kappa - \xi^\kappa M^T (Mp^\kappa),$$

The use of CGLS in computing regularized solutions in the Krylov subspace  $\mathcal{K}_\kappa$  is referred to as regularizing iterations [56]. Intuitively, CGLS is constructing a polynomial approximation to the regularized pseudoinverse of  $M$ ; given by Moore-Penrose as  $M^\dagger = (M^T M)^{-1} M$ , such that :

$$\begin{aligned} o^{(\kappa)} &= \mathcal{P}_\kappa M^\dagger y \quad 13 \\ \mathcal{P}_\kappa &= \mathcal{K}_\kappa (M^T y, M^T M) \end{aligned} \quad (5.26)$$

given :

$$r^{(\kappa)} = y - M o^{(\kappa)} = (\mathcal{I} - M \mathcal{P}_\kappa M^\dagger) y$$

The aim is to minimize the residual norm,

$$\begin{aligned} \left\| r^{(\kappa)} \right\|_2^2 &= \left\| (\mathcal{I} - \Sigma \mathcal{P}_\kappa (\Sigma^2) \Sigma) U^T y \right\|_2^2 \\ &= \sum_{i=1}^n (1 - \sigma_i^2 \mathcal{P}_\kappa(\sigma_i^2))^2 (u_i^T y)^2 = \sum_{i=1}^n \mathcal{Q}_\kappa(\sigma_i^2) (u_i^T y)^2 \end{aligned}$$

The intrinsic polynomial of CGLS explains how it converges faster than SVD based regularization. When the SVD component  $(u_i^T y)$  is large, CGLS automatically construct a polynomial  $\mathcal{Q}_\kappa(\sigma_i^2)$  with eigenvalues of the  $M^T M$  projection on the  $\mathcal{K}_\kappa$  as shown in the equation 5.27. It acts as a filter factor by enforcing "near  $\sigma_i$  roots " for the  $\mathcal{Q}_\kappa(\sigma_i^2)$  to knock out large SVD components  $(u_i^T y)^2$  [56]. In another word, one can feed the CGLS by SVD components as preconditions, such as above, with the purpose of semi-convergence by excluding the SVD components representing the noise :

$$\begin{aligned} M^T y &= M^T M o^{exact} + M^T e = \sum_{i=1}^n \sigma_i^2 (\nu_i^T o^{exact}) \nu_i + \sum_{i=1}^n \sigma_i (u_i^T e) \nu_i, \\ \therefore o^{(\kappa)} &= \sum_{i=1}^n \mathcal{Q}_\kappa^{(i)} \frac{u_i^T y}{\sigma_i} \nu_i, \\ \mathcal{Q}_\kappa^{(i)} &= 1 - \prod_{j=1}^{\kappa} \frac{\mathcal{Q}_\kappa^{(j)} - \sigma_i^2}{\mathcal{Q}_\kappa^{(j)}}. \end{aligned} \quad (5.27)$$

In TSVD the solution contains all the SVD coefficients, thus include contaminated information as well. Intrinsically the attributed coefficients have no match in the right hand side  $y$  and CGLS doesn't count for them by the means of filter factors. Hence in the exact solution  $o^{exact}$ , those coefficient are replace with zero, expediting the calculation time.

It is noteworthy that equation 5.26 tells us that the regularization depends on the data. The down side is the fact that it accommodates to the error (*e.g.* noise) correlated with the recorded data  $y$  which at the end leads to desirable yet false information such as artifacts. For this particular reason, post processing evaluations in this chapter will take place on both DSBP and CGLS to avoid biased evaluation.

13.  $\mathcal{P}_\kappa$  is the associated polynomial with  $\mathcal{K}_\kappa$  s.t. it detemines how the solution also depends on the recorded signal properties. If  $y = y^{exact} + e \Rightarrow o^{(\kappa)} = o_{e^{exact}}^{(\kappa)} + o_e^{(\kappa)}$ .

## 5.5 Post-reconstruction evaluation

In the previous chapter a comparative analysis has been followed in order to find the optimum geometries for the volumetric OPUS array's elements. Four different geometries for array of transducers has been proposed namely, circular annular array, spiral annular array and hybrid annular array of  $5\lambda \times 5\lambda$  element size and segmented annular array of  $1\lambda \times 20\lambda$  element size. Using pre-reconstruction analysis, rather similar performances has been found with slight distinctions in the favor of segmented annular array. A natural question arises on the task based performance of these arrays and their ability in delivering the high quality final output images. The two introduced reconstruction algorithms, weighted DSBP using virtual elements and model based CGLS are being employed for this purpose. Here we look at various metrics such as range of full width at half maximum (FWHM) for each measured point spread function (PSF), PSNR and structure similarity (SSIM). Along with PSNR, SSIM is used as a quantity measure of reconstructed image and is defined as :

$$\text{SSIM} = \frac{(2\mu_{\text{ref}} \mu_{\text{rec}} + c_1) \cdot (2\sigma_{\text{ref,rec}} + c_2)}{(\mu_{\text{ref}}^2 + \mu_{\text{rec}}^2 + c_1) \cdot (\sigma_{\text{ref}}^2 + \sigma_{\text{rec}}^2 + c_2)} ; \quad \text{SSIM} \in [0, 1] \quad (5.28)$$

where  $_{ref}$  and  $_{rec}$  are indication to the reference and reconstructed images,  $\mu$  is the average intensity,  $\sigma$  is the standard deviation,  $\sigma_{ref,rec}$  the covariance intensity between the two images and  $c$  is infinitesimal variable to stabilize the division.

We used these point source/reflector images to compute a local PSF. When the acquisition system is shift variant, as is the case here, the localized PSF can be defined by the image of a point. As the interest is on the volumetric imaging, we studied the axial plane for OA and lateral for US. We performed numerical studies based on spatial impulse response method. Multiple point reflectors (for US) and point sources (for OA) are positioned in the medium as a measure of point spread function of the system, in order to investigate the quality of the reconstructed images for each array.

### 5.5.1 Optoacoustic

Figure 5.11 outlines the optoacoustic images of point sources (noise-free) situated in the depth of  $20\text{mm}$  simulated for each of four virtual arrays. The points are equidistantly distributed within an axial plane of  $16 \times 16\text{mm}^2$  parallel to the surface of the arrays volume in a grid structure with  $1.5\text{mm}$  spacing. The C-scan reconstruction took place by both methods, virtual element weighted DSBP (VE-WDSBP) and model based CGLS. In order to avoid any biased conclusion, no specific regularization matrix has been used and  $\mathcal{L}$  set to be identity matrix. As the results are suggesting, it is only the segmented annular array that is capable of retrieving all the points in the medium, and that is by using model based CGLS approach. The author believes that the peculiar geometry of segmented annular array allows for every voxel within VOI be visited by all the elements. Those voxels that are sharing almost the same sensitivity (as suggested by 4.12a) are predictable by the VE-WDSBP almost in a same way as CGLS, yet lower resolution. However for the voxels with limited projections, backprojection based approaches fail to provide a reliable estimation.

Except for the hybrid array, the other geometries may provide an estimation for all the points at the cost of artifacts. In facts, the estimated value of both reconstruction algorithm for many of those points are below the artifact level. This is more evident in Figure 5.11a where the dynamic range has been increased upto 20 dB for CGLS, while for the other 12 dB is the threshold level. Indeed there are possibilities to rectify those artifacts, for instance by choosing a more adaptive regularization matrix than identity matrix. However, it is important to remember that our aim is not to adopt the algorithm to address the limitations of imaging system but showcasing the potentials of these array by relatively fair comparison analysis.

Table 5.3 quantifies these words by a set of metrics describing the range of achievable resolution (minimum to maximum) and a measure of data fidelity using PSNR and SSIM of the normalized obtained images and the ground truth.

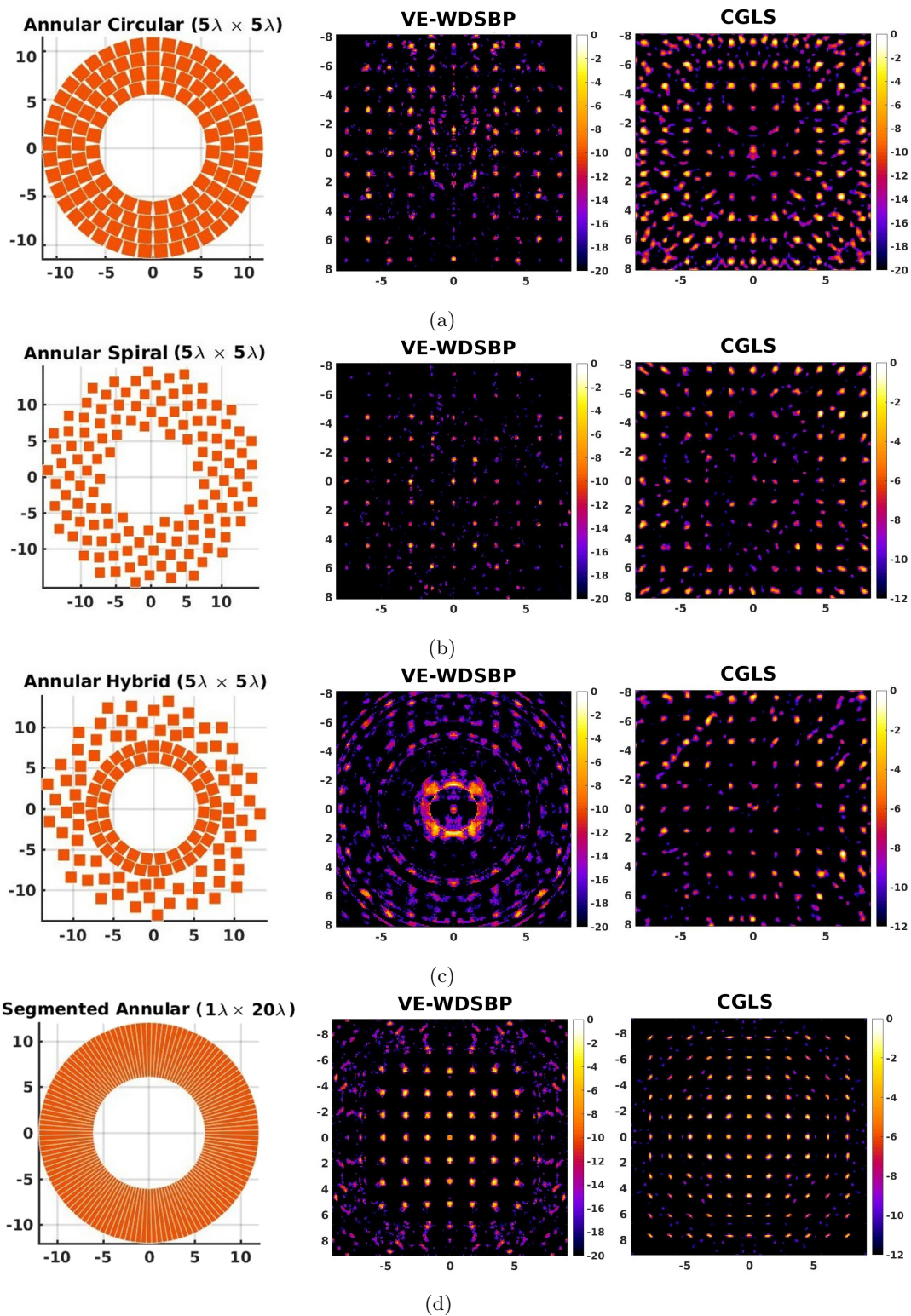


FIGURE 5.11: Imaging performance of four virtual arrays with different geometrical distributions (left column) and their imaging performance in retrieving the point sources (PSF) situated in axial plane at the depth of  $z = 20\text{mm}$  using virtual element weighted DSBP (middle column) and model based CGLS (right column) with only 10 repetition (10 basis). The reconstructed area is  $16 \times 16 \text{mm}^2$ .

FoM	Rec.	Circular ( $5\lambda \times 5\lambda$ )	Spiral ( $5\lambda \times 5\lambda$ )	Hybrid ( $5\lambda \times 5\lambda$ )	Annular ( $1\lambda \times 20\lambda$ )
PSNR	VE-WDSBP	20.27	22.15	—	19.82
	CGLS	15.83	15.68	15.84	16.49
SSIM	VE-WDSBP	0.0912	0.1324	—	0.086
	CGLS	0.2004	0.1022	0.1175	0.1340
FWHM( $\mu m$ )	VE-WDSBP	246-464	200-648	—	296-414
	CGLS	397-1112	289-551	304-530	180-372

TABLE 5.3: Quantitative evaluation on imaging performance of four virtual arrays.

Looking up the table 5.3, based on PSNR and SSIM the least distortion and best match *w.r.t.* the ground truth is offered by spiral and circular arrays, yet the values vary with the reconstruction algorithm. Additionally, the best resolution (and the least range) is achievable by using CGLS for annular array owing to the relative non periodic distribution of the elements. However, it is only the segmented annular array that offers uniform signal to background ratio over the ROI, due to its relative isotropic sensitivity. Therefore an intensity based thresholding on the log-scaled image allows to suppress the artifacts in order to visualize only the signals as suggested by Figure 5.11d.

## 5.5.2 Ultrasound

In this section, we provide the results obtained by applying the VE-WDSBP algorithm on the ultrasound signals simulated for FMC using Field II. We analyze the performance of arrays based on the provided lateral resolution and achievable dynamic range (ratio of the main lobe to side lobe) using simulated phantom containing a set of point reflectors with unity amplitude distributed in the same manner as Figure 5.5 over the volume of  $16mm$  by  $32mm$ , for  $y$ -plane = 0. The reconstructed images (B-mode) with 40 dB dynamic range are shown in Figure 5.12 to avoid artifacts such as side lobe blurring the image excessively. It is also emphasizing the effect of additional projection signals for US in compare with OA in resolution and dynamic range. Additional message of this Figure could be that the same array might shows different performance capabilities for difference modalities. The blurring artifact is clearly visible for the marginal points for all the images. Qualitatively, in terms of detectability of the sources, the segmented annular array showcases relative isotropic behavior *w.r.t.* the location of the reflectors, but it seems that spiral and circular array are capable of providing a more precise localization.

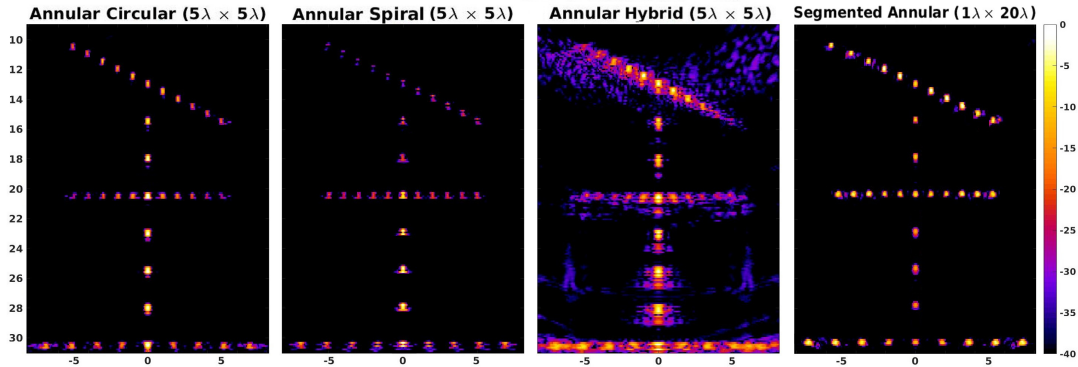


FIGURE 5.12: The VE-WDSBP reconstructed B-mode images of the point reflectors.

To better evaluate the performance in lateral resolution and dynamic range quantitatively,

Figure 5.13 depicts the lateral profile of the image for the sources at the range of  $20\text{mm}$  depth<sup>14</sup>. The estimation in the lateral dimension seems to be not exact for segmented annular. The lack of exactness is attributed to the height of elements (four times the other apertures) which causes more averaging and miss-localization. The model based reconstruction is actually taking care of this issue in OA images. It is evident the resolution is degraded as the points are approaching the margins of the FOV, for this particular geometry. While the model based reconstruction is possible for the US PE, yet the FMC model matrix is required to count for every transmit-receive event in which the size of it might be too large for inverse problem. The dynamic range however, remains competitive with slightly better (1-5 dB) for segmented annular array. This of course exclude the annular hybrid array which showcases the worst performance in terms of resolution, dynamic range, artifact level and contrast.

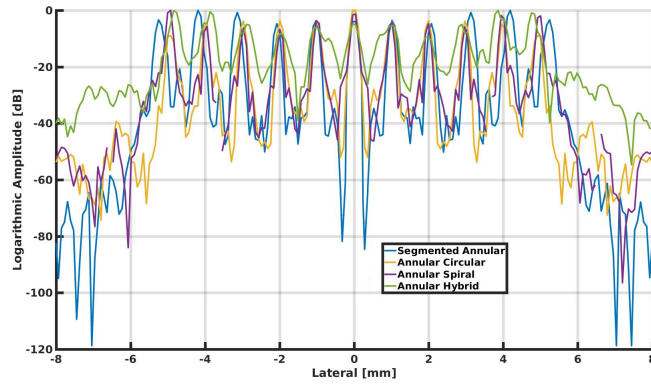


FIGURE 5.13: The lateral profile of the reconstructed images for each of the arrays at the range of  $20\text{mm}$ .

Following the same scenario as section 5.3.2, the performance of arrays has been examined over the numerical phantom containing three anechoic regions of  $3\text{mm}\varnothing$  along the lateral dimension.

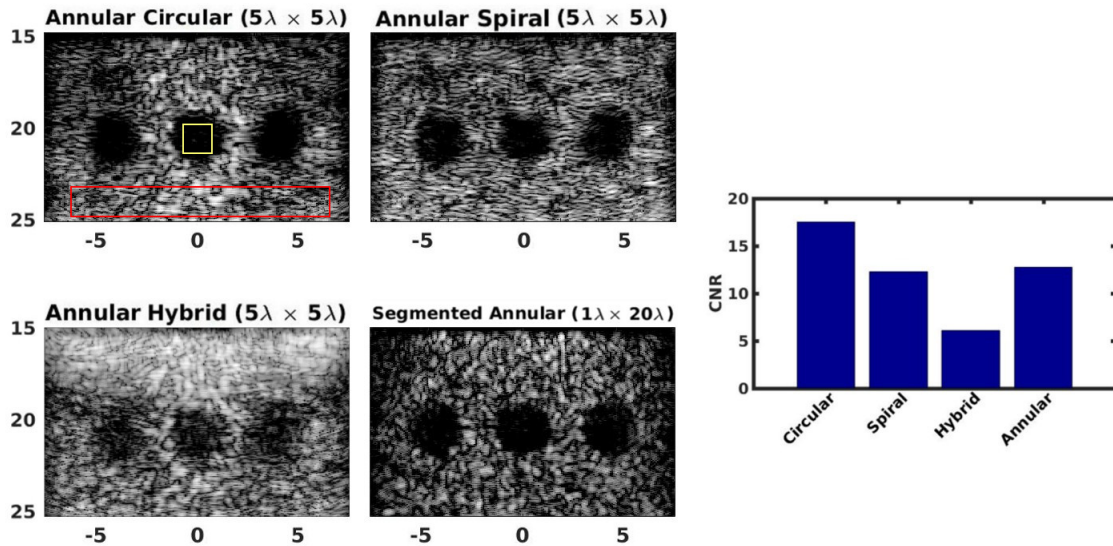


FIGURE 5.14: Evaluating the PE performance of the four virtual arrays based on the contrast and energy distribution. The yellow and red frames are indicating the lesion and background area used for calculating the CNR.

14. The minor relative axial shift in the images are imposed by the assumption of virtual element and is correctable simply by an additional term in the equation 5.20.

Figure 5.14 illustrates the result of 50 dB dynamic range of FMC pulse echo, reconstructed with VE-WDSBP for the four apertures. Again the CNR of each image has been calculated, considering the speckle background as the signal dependent noise. The values are indicating that the annular circular array is capable of offering better contrast in compare to the other three arrays (17.5), yet the energy distribution and speckles shape are changing across the lateral dimension. The bright central region is suggesting higher accumulation of energy in that area which is rather not uniformly distributed. The second best CNR belongs to the segmented annular array (12.7) followed by annular spiral (12.3). However, the nature of speckles are quite different, keeping in mind that the speckles are sometimes containing diagnostic information. The speckle structures are postulated to be granular, caused by the coherent interference between the backscattered ultrasonic waves emanated from object at the size of ultrasonic wavelength. As the resolution cells are relatively bigger than these structures, a non random formed speckle pattern is expected with probability distribution of Nakagami shape. Nonetheless, the shape this coherent interference artifact is highly associated with the phase of back-scattered echos, and their averaging over the surface of the aperture. Therefore, it leaves the question weather the structure offered by the annular spiral is better or worth in comparison with segmented annular array.



## 5.6 Conclusion

The presented chapter was dedicated to the data processing, image reconstruction and post reconstruction evaluation of the virtual arrays. It was demonstrated that the distorting effect of acoustic-electric impulse response on the image can be compensated. Four estimators have been employed, however MMSE GCV was more immune to the noise.

Additionally, two dedicated reconstruction algorithms have been developed and their performance have been compared. The quality of images have been quantified as a function of contrast and resolution. The VE-WDSBP showcased an estimation relevant to the matched filter evaluation, yet this estimation has its own limitations. In reconstruction of C-scan OA, the model based CGLS based on Krylov subspace clearly outperforms the VE-WDSBP. The model based CGLS is based on a more accurate modeling of the system that enables higher quality reconstructed images. It might be due to the fact the virtual elements formulation requires additional preciseness in the formula for isotropic detectability. Additionally, maximum intensity projection over certain number of axial voxels can be employed for further improving the VE-WDSBP. Comparing with Tikhonov or its equivalent formulation MMSE, the CGLS itself doesn't incorporate the penalty term. There are ways to augment CGLS to tackle the aforementioned challenge by means of incorporating a form of  $\mathcal{L}$  as precondition. The important feature is that the incorporation of particular errors can be minimized via regularization parameter. Yet the nature of error must be known to be precisely dealt with. Withal, VE-WDSBP has been used in US PE images for the sake of simplicity in calculation and avoiding the artifacts for the speckle regions. Indeed those regions are requiring a true estimation to be incorporated in the regularization term.

Based on the reconstructed images, a qualitative and quantitative comparisational analysis took place among the four proposed geometries. Overall tasked based performance of segmented annular array in imaging might outweigh the rest, considering the resolution, detectability and uniform response for both modalities. Yet, we believe that there are rooms for improving the performance of annular circular and annular spiral, for example by considering the suitable regularization term. This can be followed in the future researches.

Last but not least, it worth to mention that the simulation model presented in this chapter, as well as chapter 4, discount the effect of acoustic impedance mismatch between the transducers. Nonetheless this model has been shown to accurately describe the effect of individual transducer and hence the over all aperture on the detection characteristics of OPUS array imaging.



# CHAPITRE 6

---

## Experimental validation

---

The test of all knowledge is  
experiment. Experiment is the sole  
judge of scientific truth.


---

Richard P. Feynman

### Abstract

The concept of segmented annular array for OPUS imaging has been discussed in detail in chapter four. The performance of the proposed geometry has been investigated through simulation studies in chapter 5. In order to validate the simulation results and further proof of concept, an experimental study has been conducted. A linear array composed of 192 CMUT elements have been mounted on a motorized rotary stage. In order to mimic the segmented annular array, the central element of the array orbits the  $z$ -axis in 128 steps at destined positions. A defocused cylindrical concave acoustic lens has been placed in front of the array to compensate the directivity. The experiments were carried out by directing the laser light on a made phantom with printed patterns of dots in a grid structure. The images have been reconstructed using the two proposed reconstruction algorithm in the previous chapter namely, virtual element delay and sum back projection and model based image reconstruction algorithms. The results are promising with comparable fidelity and image quality.

## 6.1 Introduction

PERIMENTAL validation studies are necessary step to confirm the performance of the designed system. Yet, they constitute a formidable challenge due to the difficulties associated with the implementation of simulated parameters in an exact manner. Hypothetically, the measurement system containing array of ultrasonic transducers can be emulated via synthetic measurement system in which a single transducer scanned over an orbit in the geometrical locations destined for each element of the probe. This approach justifies the performance for optoacoustic imaging. At ultrasonic end, the measurement remains for a set up that allows for transmission events. Such a system demands for multiple active elements to provide sufficient insonification angle. In synthetic measurement, one active and one passive element might be enough under the condition that scanning system allows individual positioning.

The remainder of the chapter is structured as follow. In section 6.2, the employed measurement set up will be explained. It will be followed by section 6.3 in which the transducer acousto-electric impulse response measurement and angular sensitivity measurement of the probe in addition to the phantom preparation is presented. Section 6.4 illustrates the result of reconstruction algorithms of the phantom.

## 6.2 Experimental setup

The OA imaging system presented herein was developed to emulate the segmented annular array. The experimental set up is shown in Figure 6.1. It is mainly composed of three major components, the light delivery system, the acquisition (acoustic/electronic) system and the scanning system consist of motorized stage with a holder.

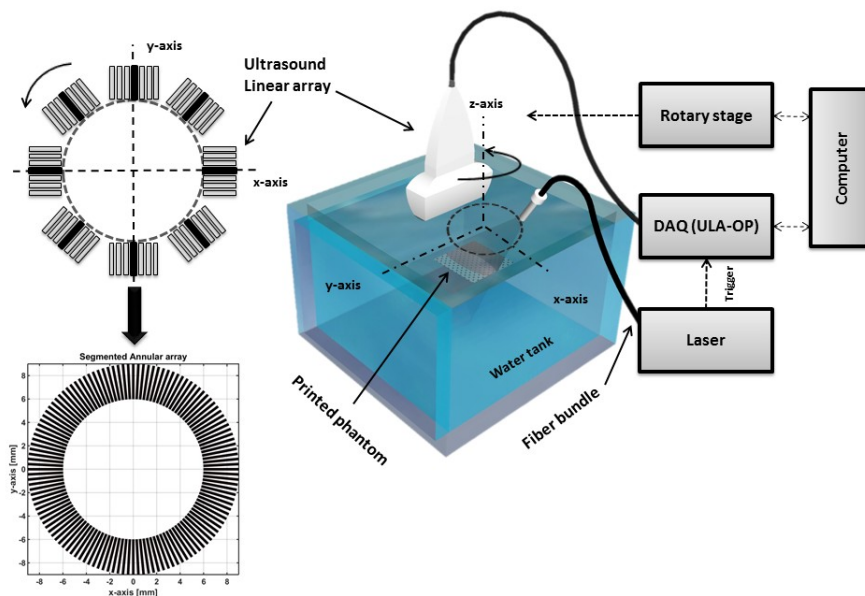


FIGURE 6.1: Annotated schematic of optoacoustic experimental setup. The ultrasonic probe is mounted on the rotary stage (not depicted). The scanning is taking place over the sample (printed phantom) located parallel to the plane of imaging under the array of sensors within the water tank. The water tank is aligned with the  $x$ - $y$  axes of Cartesian coordinate system. The  $z$ -axis is corresponding to the axis of rotation.

### 6.2.1 Illumination system

In the first part, excitation light is originated from a tunable Nd :YAG laser (Quanta-ray INDI, Spectra-Physics), delivering pulses with duration of  $\approx 5nsec$  and pulse repetition frequency (PRF) of 10Hz, set at wavelength of  $1064 nm$ . While the laser is running for the designated period, for every pulse a trigger signal is sent to the acquisition system for synchronization. A dedicated software allows for synchronization of receive system with laser trigger signal. The output of the laser is coupled to randomized fiber bundle (CeramOptec GmbH, Bonn, Germany) composed of 431 individual optical fibers, each with  $0.3 mm$  silica core diameter and 0.22 numerical aperture. At the other end of bundle, a radial shaped illumination pattern of  $10 mm$  diameter is delivered at the irradiation side. Practically we managed to achieve 60% efficiency for light coupling through the bundle. The losses are associated with the input coupling and the reflection at the bundle ends. Initially the bundle was considered to be placed on the axis of rotation, as it is suggested by the array geometry, however the bulk of probe holder doesn't leave space on the center. In order to deliver the light, the bundle is coupled to the measurement system by a rigid arm such that

the illumination was performed from one side of the sample. This ensures the epi-illumination for reflection mode OPUS array. The fiber bundle was kept fix for entire acquisition.

### 6.2.2 Acquisition system

The excited optoacoustic signal detection was performed by a linear array probe (ACULAB, Univeristá degli Studi Roma Tre, Rome, Italy) composed of 192 CMUT elements of 0.2 *mm* width and 3 *mm* height. The average center frequency of the array is about 10 MHz with  $-6$ dB bandwidth of 100%. A cylindrical concave acoustic lens was applied to the CMUT probe head, in order to compensate for the directivity of the array. The composite material has 1120 *m/s* speed of sound with 7 dB/mm attenuation for 10 MHz, designed for a  $60^\circ$  at  $-3$ dB angle in the elevation direction. The lens is expected to alter the spectral properties of the received signals by introducing extra spatial-temporal averaging. The probe head is connected to a probe handle, containing a 192-channel receive analog [139]. In order to increase the sensitivity of the array, the bias voltage was set close to the maximum safe level 210 *V* (80% of the collapse voltage) while the probe can be driven under  $\pm 60$ *V* (20% of the collapse voltage), but the elements are in passive recording mode. The probe contains frontend electronics including a low noise receive amplifier (LNA) with a capacitive feed back [139] and a multipolar cable for connection to the ultrasound imaging system. The US probe has been interfaced to the ULA-OP 64 scanner system [154] that allows for recording the time gated raw optoacoustic signals detected by the aperture. ULA-OP scanner is developed by the Microelectronics System Design Lab of the University of Florence, a portable and compact scanner with PC interface software. It contains transmission and reception sections of which the second one is of our interest (can be set for receive only mode). When the optoacoustic signal is arriving at the surface of the probe elements, the recorded signals are being further treated by LNAs and later time gain control amplifiers with modifiable gain in the range of 6-46 dB. These are provided by the analog board front-end electronics, providing access to 64 channels/elements. The recording process is further pursued by an analog to digital converter (12 bit resolution) for every amplified signal, sampling the signal at 50 MHz. The integrated digital logic board in the ULA-OP contains four field programmable gate arrays (FPGA) that may use for the dynamic receive beamforming to monitor the respective location of probe and sample. From there the signals are forwarded to the embedded digital signal processor (DSP), low pass filtered to avoid the additional high frequency noise. The system includes 1.5 GiB physical memory for momentary data storage that can be transferred to the PC for image reconstruction. The laser trigger is synchronized to the data-acquisition ULA-OP scanner to allow the multiple optoacoustic data recording and further averaging.

### 6.2.3 Scanning system

The linear array was mounted on the motorized rotary stage (OWIS GmbH, Staufen, Germany) by the help of a 3D printed custom made probe holder (UpBox 3D printer Pack, Machines-3D, Anzin, France). The active surface of the transducers were pointing downward to the bottom of the water tank. The housing makes sure that the ultrasound probe is parallel to *x-y* axes and hence, the plane of imaging. The computer controlled stage is equipped with stepper motor (Faulhaber GmbH, Germany) with the precision of ( $0.001^\circ$  precision), allows to rotate the array around the *z*-axis at the predesignated location for a complete  $360^\circ$ . The stage was fixed to the U-shape metallic frame (platform) on top of the water tank, holding and rotating the downward looking US probe. The probe holder positions the transducer such that the central element of the array is placed 6 *mm* away from the axis of rotation. While rotating, the element of choice is recording the OA signal at the position of every 128 elements of segmented annular array, in a synthetic manner.

## 6.3 Measurement

### 6.3.1 Transducer characterization

Before the experimental measurement, the frequency characteristics of the transducer must be calibrated. The main aim of this step is to realize the effect of concave lens and its impulse response on the recorded signals. Additionally, the recorded signal can be employed as the acousto-electric impulse response to be deconvolved from the recorded signals.

A thin black suture (ETHILON, 10-0 gauge, Polyamide 6 black monofilament) of  $20 - 29 \mu\text{m} \varnothing$  diameter is attached at each end to opposite walls of a U-shape dedicated wire holder, immersed in the water. The suture is positioned under the ultrasound linear array, perpendicular to its length axis (Figure 6.2a). To avoid diffraction, the size of the suture is chosen such that it can be considered as a point source ( $< \lambda_{\text{cut-off}}/2$ ) corresponding to the maximum cut off frequency (15 MHz) of the receiving elements. The suture was aligned with the central element of the array which later is utilized for imitating the segmented annular array in a synthetic manner. The alignment is estimated such that the peak of the parabola made by the raw received signals of the array is received by the central element (Figure 6.2b). The suture is uniformly irradiated by the laser pulse. The broadband omnidirectional optoacoustic response is considered as the optoacoustic point source. The induced wave is recorded by the transducer and the recorded signal is considered as the receive acousto-electric impulse response. The spectrum of AIR would indicate the frequency characteristics of the transducer, including the B.W. and the central frequency. Figure 6.2a illustrates the AIR and spectrum of the recorded signal, indicating the -6dB bandwidth and the central frequency of the array's central element. Noteworthy is that the N-shape OA bipolar profile is both elongated and followed by the tail. The first effect can be attributed to the averaging over the surface of the transducer and the imposed delay by defocused lens. The latter, can be explained by the interaction between the incoming wave and the marginal parts (1.45 mm at each side) of the lens which are not directly in front of the transducer and not necessarily converging the deflected beam on the center of the transducer (Figure 6.3a). The author believes that these effects are the main causes of the shift in the central frequency and shrinking the bandwidth.

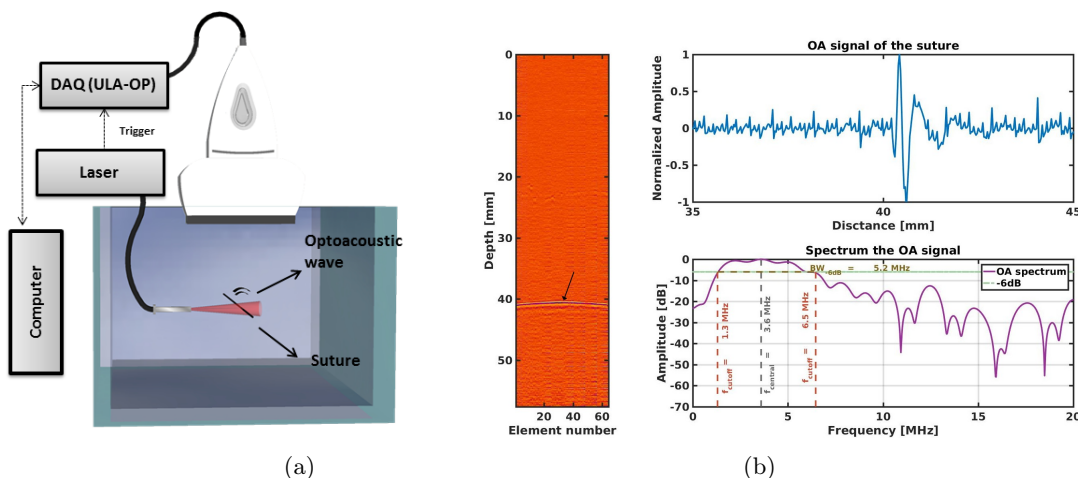


FIGURE 6.2: (a) Schematic of the set up performed to measure AIR and lens impulse response of the CMUT transducer. The broadband and cylindrical omnidirectional optoacoustic wave is generated by shedding the short pulse laser on the suture. (b) Left : the recorded signals by the 64 central elements of the ultrasonic array. The peak of parabola is recorded by 31<sup>th</sup> element which marked by the arrow. Right : The optoacoustic signal received by the 31<sup>th</sup> element and its spectrum, indicating the 3.6 MHz central frequency and -6dB bandwidth between 1.3-6.5 MHz.

Additionally, by mounting the transducer on translating  $x$ - $y$  motorized stage, the directivity of the transducer in elevation (defocused by lens) is measured and is compared to the theoretical one, calculated using k-wave simulation toolbox. Figure 6.3a depicts the schematic of the measured set up and the geometrical shape of the acoustic lens. The sensitivity of the transducer for the measured central frequency of 3.36 MHz over the scanning range of 20 mm is an indication for the directivity. Figure 6.3b illustrates the calculated and measured directivity. The suture is paralleled to the length axis of the array due to the fact that the generated wave is cylindrical. By scanning the array at 20 steps with 1 mm interval, on the axis perpendicular to the length axis of the array and recording the OA signals, the directivity has been measured. The measured amplitudes decays with increase in the angle, and that drops below -6 dB at  $\pm 12^\circ$ . Therefore, in order to obtain a field of view as close as possible to the simulated region, where the aperture is uniformly sensitive and overlapping between the elements at each position are insured, the depth of the plane from the array must be increased to the depth of at least 40 mm.

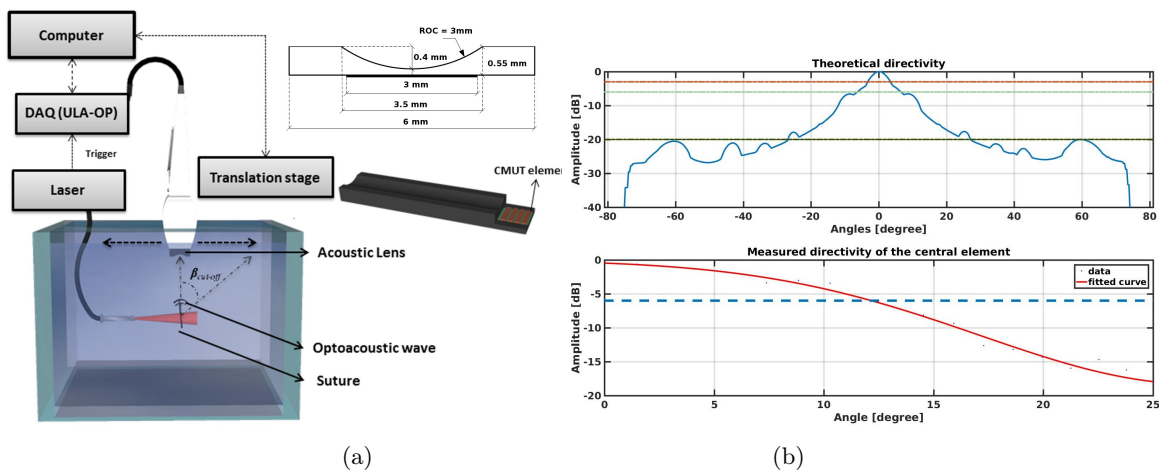


FIGURE 6.3: (a) Schematic of the set up performed to measure the directivity of the central element along the elevation direction with the concave lens. (b) The calculated (top) and measured (bottom) directivity of the central element.

### 6.3.2 Acquisition

The central window of the array (64 elements) is recording the induced optoacoustic waves generated by the phantom at 128 positions, completing 360°. At every step, the signals of 20 laser pulses are being recorded and averaged before reconstruction, in order to improve signal to noise ratio. Since the delivered light from the bundle is minimally diverged, the intralipid 20% has been used in 1% amount *w.r.t* to the water, in order to diffuse the light and maximize the illumination area.

### 6.3.3 Phantom

The calibration phantoms were produced by printing a digital pattern on an A4 overhead projector transparent film (0.35 mm thickness) using a standard black and white Xerox printing machine (Workcenter 5665) with resolution of 600 × 600 dpi. Figure 6.4 shows the printed phantom of dots places in grid structure [159]. The dots pattern is composed of 11 × 11 dots, each with 0.25 mm  $\varnothing$  distributed in the area of 15 × 15 mm<sup>2</sup> size with 1.3 mm inter dot spacing. The phantom is immersed in the water at the depth of 40 mm away from the surface of the ultrasonic transducer and positioned over a cylinder shape structure with uniform height.

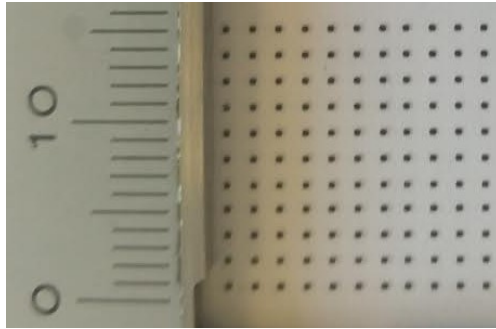


FIGURE 6.4: The printed phantom of 121 dots pattern of 0.25 mm size

## 6.4 Results

Prior to reconstruction, a band-pass filter is applied on the signals with cut-off frequency of 0.2-11 MHz. The choice of the bandwidth is a heuristic compromise between the most fiddle components, the thermal noise (high frequencies) and lumpy background artifacts (low frequencies). The signals are further deconvolved with the measured impulse response. In previous chapter, we have shown the VE-DSBP and CGLS algorithms successfully applied for the reconstruction of similar *in situ* phantom in simulation. The proposed algorithms are also applied for the experimental measurements in order to build the image. For the reconstruction of the c-scan slice  $16 \times 16 \text{ mm}^2$ , the acoustic speed of sound has been taken as  $1484 \text{ m/s}$ . The model has been used for the model based CGLS algorithm is calculated rather than measured, explained in chapter 3. The divergence of the transducer has been estimated based on the geometrical properties of the lens and measured directivity. The results are shown in Figure 6.5.

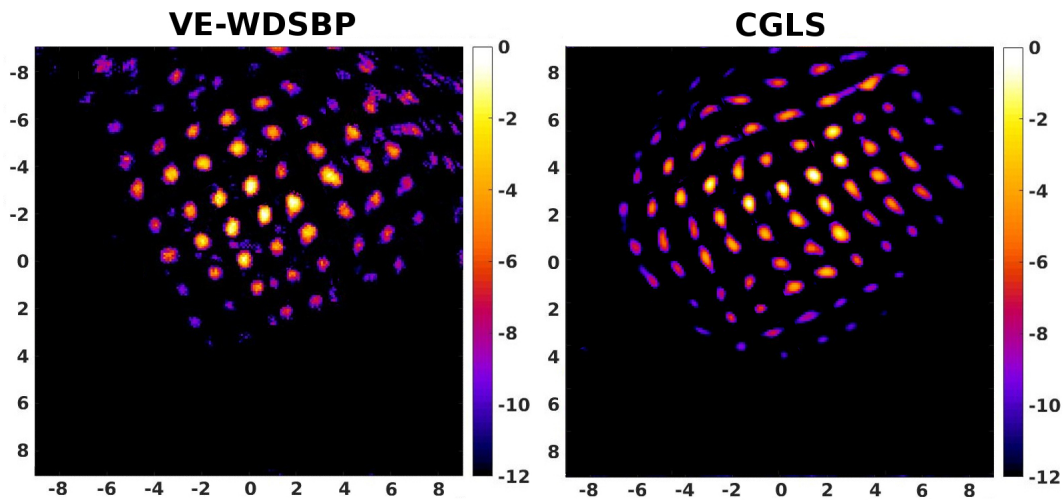


FIGURE 6.5: Reconstructed OA image of the dot phantom formed by the VE-DSBP algorithm in the left, and model based CGLS in the right.

Clearly there is a misalignment in the measurement setup between the aperture FOV, location of the sample and the illumination side. Whats more, the plane of imaging and the object plane are not completely parallel, leading to out-of plane focusing. To cope with, the presented images are the result of maximum intensity projection over the aligned stack of 2D images of the range of 1 mm. Nonetheless both algorithm are demonstrating an acceptable performance, even though the property of the array is not entirely known.



## 6.5 Conclusion

In this chapter, I have investigated the performance of novel strategy, rotating a linear array in order to mimic the segmented annular array for the OA imaging. Both proposed algorithms in chapter 5 have been practically evaluated and their performance have been validated with experimental data. The emphasis was put on operating with defocused ultrasonic linear array equipped with a negative lens. Even though the exact parameters of the array weren't completely known and considering the level of uncertainties, the study demonstrated the proposed implementation as a proof of concept for the proposed geometry.

The simulation study proposed, the performance of model based algorithm deemed to be provided superior with most desirable fidelity and image quality. However accurate model based reconstruction algorithm requires exact model either calculated based on true prior knowledge of system a measured via scanning a point source like object over the volume of interest. The latter is more popular due to the fact that all the information including noise level is incorporated in the model beforehand. This could be done in future studies by the help of robotic arm or an  $x-y-z$  motorized translating stage.

Lack of dedicated measurement system for the indented purpose of volumetric bimodal imaging can be addressed by developing a forward imaging system such that the alignment between the aperture field of view, sample and trans-the illumination light delivery system. Further, employing a light diffuser in front of the optical probe can optimize the uniform excitation of the OA signal.

Last but not least, the ultrasonic validation can be pursued by optically exciting an acoustically transparent sheet. This way, ultrasound imaging of the system in flash mode of acquisition can be evaluated.

As an optoacoustic/ultrasound imaging, the segmented annular array has demonstrated an acceptable performance and is expected to have an impact on bimodal portable measurement systems. The experimental results of this chapter, are not flawless but provide a validation on the claims have been made in chapter four and five.



# CHAPITRE 7

---

## Conclusion and Perspective

---

If we knew what it was we were doing,  
it would not be called research, would  
it ?

---

Albert Einstein

### Abstract

Given the need for a portable, non-invasive and non-ionizing *in vivo* diagnostic modality, optoacoustic ultrasound (OPUS) is a promising hybridized technique that offers a new perspective in the medical imaging fields. The benefit of this bimodality rests in simultaneous data acquisition, precise co-registration and correspondingly, the correlation between the detail anatomical data of ultrasonic image and physiological information of optoacoustic image. There are various technical challenges associated with this integration, rising from the inherent physical differences of these two modalities. Through out this work, the evolution of a novel sparse annular geometry and its dynamics for volumetric imaging has been detailed. This final chapter is devoted to an overview of the findings and accomplishments with respect to design, characterization and development of a universal hand-held OPUS. The challenges ahead and future perspectives in terms of instrument development and post-processing are further discussed.

**P**RACTICAL implementation of 3D optoacoustic-ultrasound (OPUS) requires the development of a dedicated handheld probe that is accommodating the perspectives of both modalities. In this work, an effort took place to design and develop a portable bimodal imaging system for OPUS volumetric imaging. The impetus of the work has come from the diverse need for a portable multistage and multiscale measurement system that is capable of assaying the morphology and pathology of the tissue in a concurrent manner. Optoacoustic (OA) is probing the molecular constituent of the tissue based on their spectrum signature, up to several centimeters depth. Offering such information on top of the classical ultrasonic pulse echo (US-PE) images not only provide the physiologist with additional diagnostic values but pave the way for OA imaging to be deployed as a clinically viable technology. In pursuit of transferring this methodology to clinic, the evolution of a novel sparse annular geometry and its dynamics has been investigated and a proof of concept was demonstrated via experimental measurement with the intention of benchmarking progress.

## 7.1 Summary and concluding remarks

The necessary background centered on the physical phenomena involved in both modalities and fundamentals of imaging have been discussed in chapter 2. In order to provide the context for our application, tandem employment and crosscommunication between OA and US, the conditions for optimal image formation have been discussed. It was concluded that for a high throughput bimodal system the designed array must meet the optimum compromise rather than individual optimization.

A fruitful assessment of the designed system that correlates the imaging performance with the behavior of the aperture is both imperative and crucial. This dissertation has detailed the theory of a framework as *de facto* analysis tool and demonstrated the efficiency of such an evaluator for characterization and optimization of both passive and active reflection mode ultrasonic imaging systems. Several substantial steps have been taken toward the development of a high compelling imaging probe.

An underpinning step of this work was deriving a discrete linear model that explains the behavior of designed imaging system. According to the idea of impulse response, the correlation between the wave field and recorded signal can be established via medium-transducer transfer function. Similarly, the scattered/absorption wavefields and sought after image can be linked by medium-aperture propagation matrix. It follows that a well constructed model based on a set of governing equations of wave propagation approximates the total system response for any given arrangement of the transducers. Since the properties of the transducers are already incorporated in the model, the model is explaining the spatio-temporal filters imposed by the acousto-electric response (AIR) and finite size of the transducer and limited view of the aperture (Chapter 3).

The purpose of developing the accurate model is two fold : 1) to characterize and further optimize the imaging aptitude of the array as a spatial variant limited view tomographic system ; and 2) to be employed in conjunction with image reconstruction as an accurate imaging operator.

Once the initial parameters of the array is given, a set of analysis must be conduct to evaluate the performance of the array based on the developed numeric-discrete-model. In particular the effect of size, number and geometrical location of the elements and their optimum configurations have been investigating. In order to assess and optimize the performance characteristics of the array, a generic assessment of the imaging system that provides an insight to the imaging quality of the designed system is practiced. As a mean of design evaluation, the voxel crosstalk matrix and eigenanalysis provide metrics for comparison appraisal and optimization. Having founded on spatial impulse response as the voxel basis function, the voxel crosstalk matrix acts on the individual basis functions such that individual spatial aliasing between pair of voxels is determined. Additionally, the information with respect to the overall spatial response of the aperture is contained in the diagonal elements of voxel crosstalk matrix. It was shown that the diagonality of the voxel crosstalk matrix is highly proportional to the accuracy of source estimation.

Considering OPUS as a spatial variant imaging system, it was shown that the eigenanalysis manifests the retrievable angular frequencies associated with aperture limited view, but also the degree of which these components are resolvable. Employing the two approaches in the format of pre-reconstruction evaluation enabled :

- Estimating the degree of spatial blurring and spatial sensitivity inherent in the aperture.
- Estimating the sensitivity of the aperture relative to the spatial orientation of the object-source structure.
- Revealing information about the spatial sensitivity of the array and beam propagation.
- Estimating the steerability of the aperture.
- Quantitative and qualitative appraisal analysis.
- The optimum compromise between number, size and geometrical distributions of the transceiving elements for a volumetric OPUS imaging system (the effect of element size on directivity is remedied by negative focusing lens).
- Optimizing a 2D array *w.r.t.* the aforementioned parameters for a volumetric handheld probe.

Throughout the analysis, it was found that the annular geometry provides a unique layout for moderately large aperture containing limited number of elements. Owing to its circular symmetry and inherent lumen, uniform excitation/insonification within the FOV is insured which is suitable for volumetric imaging. These studies confirmed that the superior performance is accompanied by increasing the number and size of the elements. The simulation results in chapter 4 have suggested three annular geometries, the performance of each was evaluated via post-reconstruction analysis in chapter 5.

Within the context of post reconstruction evaluation, major emphasis was put on modifying and developing image reconstruction algorithms in order to elevate the fidelity of object estimation, hence the accuracy of reconstruction. Chapter 5 offered the tenets for two befitting reconstruction algorithms adopting to the properties geometries. For one part, the significance of AIR deconvolution has been discussed. The merits of four standard techniques have been compared on retrieving the true signal and on final image quality. Both qualitative and quantitative assessments were indicating the superior performance of MMSE GCV approach in the presence of the noise, with the least artifacts in the reconstructed image. Noteworthy is that as long as the level of the noise is controlled, the Wiener filter shows conceiving behavior. As it was found later in chapter 6, denoising has a major impact on the outcome of deconvolution.

The next step was the estimation and that has been initially performed by means of modifying the classical delay and sum back projection (DSBP) to address the distortions arose from spatial sub-sampling of the sparse arrays and the unconventional geometry of the elements. Along side the virtual element concept an adaptive weighting factor, on the account of coherency, has been developed to for VE-WDSBP. It was shown that under certain condition, the VE-WDSBP estimator approaches the matched filter. The weighting factor has honed the accuracy of estimation, particularly over the DSBP, yet and despite the improvement by VE, the shortcomings occur in C-scan reconstructions. The diffraction imposed by the finite size of the transducer is demanding for an alternate approach in which the effect of spatio-temporal filter nullifies. By employing the developed model in chapter 3 as the imaging operator in the conjugate gradient least square estimator (CGLS) offers more accurate analytical solution. The performance of both proposed methods have been assessed on simulated and later in chapter 6, on experimental data. The results confirmed the findings stated earlier and they were in favor of CGLS.

These images have been utilized in a set of qualitative and quantitative tasked performance assessment, with the purpose of comparison analysis of the proposed arrays in chapter 4. Evaluation was performed in the terms of resolution, contrast and fidelity of the final estimation. We found that the segmented annular array in combination with CGLS estimates the most reliable data.

In order to validate the results by experimental data, a synthetic imaging system was developed (chapter 6). A linear array equipped with diverging acoustic lens has been employed in a rotation fashion, such that for an arbitrary element a segmented annular array is emulated. A calibration phantom has been utilized with similar properties to the simulation described in chapter 5. Little was known about the employed array characteristics and that, the cost the accuracy of estimators. Despite the imperfections associated with the set up, a correspondence was shown to exist between the experimental and simulated results. For those structures that were excited within the FOV of the synthetic array, reasonable estimation has been demonstrated.

In conclusion, this work presents the development of a bimodal system and adopted algorithms for volumetric optoacoustic ultrasound handheld probe. The theory behind this development has been established and proof of concept was showcased the potentials of this bimodality. Further optimization is deferred to the future time.

## 7.2 Future work

We have barely scratched the surface in instrumenting a potent multi-scale volumetric clinical imaging system. The design and development of such an imaging system is an intricate procedure that demands for systematic interplay involving various disciplines and that pursued by complementary practices that bestows the gradual procurement of skills. The perspective of this work could concern the following :

- **Model matrix** : Of the theoretical interest, the size of the developed model matrix is inherently large which is problematic *w.r.t.* inversion and pre-reconstruction analysis. In the pursuit of sparser matrix, one approach that can be followed is multi-resolution. Among many, the wavelet packet and multigrid are reliable candid to begin with. The author expect that the multi-resolution approach conduct to a more robust approach in selective task based performance analysis and optimization of the array parameters. Additional advantages could be the possibilities of incorporating the optical propagation and acoustic properties of the medium within the matrix.
- **Validation studies** : The early results of the experimental measurements provide consistent result with simulation that left a positive feedback with respect to the design. Yet, there is an obvious need for optimizing the experimental setup and characterizing the measurement system. The logical extension of this work should be the conduction of further experimental studies for detection tasks, including a volumetric samples with different structural features.
- **Parallel implementations** : Using the model based algorithm which involves with large sets of linear equation has a computation cost. In order to ascertain the advantages of 3D OPUS, what we consider real-time dynamic imaging requires fast rendering. Parallel GPU based computation addresses the problem which would be pursued in the future.
- **Multi-band frequency array** :  
The strong momentum of optoacoustic imaging development is fueled by the frequency rich nature of optoacoustic signal. A multi-bandwidth detection system device has the potentials of advancing the technique and result interpretation. This would be an interesting line of research.
- **Instrumentation** :  
These general viewpoints related to the systemic development and instrumentation of the device. Instrumentation requires further validation study, both in ultrasound and optoacoustic imaging. However our research results motivate us to consider the fabrication for the future.

Developing new tools which not only answer but pose questions is pivotal for researchers to refine the problem. The questions arose from the answers as Nietzsche described is crucial for finding alternative roads for investigation. I would pen the final words of this thesis by a quote of Richard Feynman : "We absolutely must leave room for doubt or there is no progress and no learning and a question requires doubt."

---

## List of Publications

---

### Journal paper

**Kalkhoran M.A.**, Vray D., "*Design and characterization of optoacoustic ultrasound hand-held probe for volumetric imaging*". (manuscript in preparation)

**Kalkhoran M.A.**, et. al., "*On Experimental validation of a handheld annular array probe for volumetric OPUS imaging*". (manuscript in preparation)

### Proceeding

**Kalkhoran M.A.**, Varray F., Vallet M., Vray D. "*Volumetric pulse echo and optoacoustic imaging by elaborating a weighted SAFT*". 2015 IEEE International Ultrasonics Symposium

**Kalkhoran M.A.**, Varray F., Vray D. "*Dual frequency band annular probe for volumetric pulse-echo optoacoustic imaging*". Proceedings of the 2015 ICU International Congress on Ultrasonics

Varray F., **Kalkhoran M.A.**, Vray D. "*Adaptive minimum variance coupled with Sign and phase coherence factors in IQ domain for plane wave beamforming*". 2016 IEEE International Ultrasonics Symposium

Boulos P., Varray F., Poizat A., **Kalkhoran M.A.**, Gilles B., Bera J.C., Cachard C. "*Passive cavitation imaging using different advanced beamforming methods*". 2016 IEEE International Ultrasonics Symposium

Vallet M., Varray F., **Kalkhoran, M.A.**, Vray D. "*Enhancement of photoacoustic imaging quality by using CMUT technology : Experimental study*". 2014 IEEE International Ultrasonics Symposium





- [1] Z136.1 american national standard for the safe use of lasers. american national standards institute," author=Standard, ANSI, year=2007,.
- [2] Functional ultrasound imaging of the brain. *Nat Meth*, 8(8) :662 – 664, 2011.
- [3] Andres Aguirre, Puyun Guo, John Gamelin, Shikui Yan, Mary M. Sanders, Molly Brewer, and Qing Zhu. Coregistered three-dimensional ultrasound and photoacoustic imaging system for ovarian tissue characterization. *Journal of Biomedical Optics*, 14(5) :054014–054014–9, 2009.
- [4] M Akhnaq, O Martinez, F Montero de Espinosa, and LG Ullate. Development of a segmented annular array transducer for acoustic imaging. *Ndt & E International*, 35(7) :427–431, 2002.
- [5] TJ Allen and PC Beard. Optimising the detection parameters for deep-tissue photoacoustic imaging. In *SPIE BiOS*, pages 82230P–82230P. International Society for Optics and Photonics, 2012.
- [6] Mark A Anastasio, Jin Zhang, Dimple Modgil, and Patrick J La Rivière. Application of inverse source concepts to photoacoustic tomography. *Inverse Problems*, 23(6) :S21, 2007.
- [7] RS Anderssen and PM Prenter. A formal comparison of methods proposed for the numerical solution of first kind integral equations. *The Journal of the Australian Mathematical Society. Series B. Applied Mathematics*, 22(04) :488–500, 1981.
- [8] Valeriy G Andreev, Alexander A Karabutov, and Alexander A Oraevsky. Detection of ultrawide-band ultrasound pulses in optoacoustic tomography. *IEEE transactions on ultrasonics, ferroelectrics, and frequency control*, 50(10) :1383–1390, 2003.
- [9] Bastien Arnal, Chen-Wei Wei, Camilo Perez, Thu-Mai Nguyen, Michael Lombardo, Ivan Pelivanov, Lilo D. Pozzo, and Matthew O’Donnell. Sono-photoacoustic imaging of gold nanoemulsions : Part ii. real time imaging. *Photoacoustics*, 3(1) :11 – 19, 2015. Special Issue : Contrast Agents for optoacoustic imaging and sensing : Design and biomedical applications.
- [10] Shai Ashkenazi, Yang Hou, Takashi Buma, and Matthew O’Donnell. Optoacoustic imaging using thin polymer etalon. *Applied Physics Letters*, 86(13) :134102, 2005.
- [11] A. Austeng and S. Holm. Sparse 2-d arrays for 3-d phased array imaging - design methods. *IEEE Transactions on Ultrasonics, Ferroelectrics, and Frequency Control*, 49(8) :1073–1086, Aug 2002.
- [12] JC Bamber. Attenuation and absorption. In *Physical principles of medical ultrasonics*, pages 118–186. Ellis Horwood Limited Chichester, 1986.
- [13] Harrison H Barrett, JL Denny, Robert F Wagner, and Kyle J Myers. Objective assessment of image quality. ii. fisher information, fourier crosstalk, and figures of merit for task performance. *JOSA A*, 12(5) :834–852, 1995.
- [14] Paul Beard. Biomedical photoacoustic imaging. *Interface focus*, 1(4) :602–631, 2011.

- [15] Muyinatu A Lediju Bell, Xiaoyu Guo, Danny Y Song, and Emad M Boctor. Transurethral light delivery for prostate photoacoustic imaging. *Journal of biomedical optics*, 20(3) :036002–036002, 2015.
- [16] DA Boas, MA O’leary, B Chance, and AG Yodh. Scattering of diffuse photon density waves by spherical inhomogeneities within turbid media : analytic solution and applications. *Proceedings of the National Academy of Sciences*, 91(11) :4887–4891, 1994.
- [17] David J Brady. *Optical imaging and spectroscopy*. John Wiley & Sons, 2009.
- [18] Andreas Buehler, Amir Rosenthal, Thomas Jetzfellner, Alexander Dima, Daniel Razansky, and Vasilis Ntziachristos. Model-based optoacoustic inversions with incomplete projection data. *Medical physics*, 38(3) :1694–1704, 2011.
- [19] T Buma, M Spisar, and M O’donnell. High-frequency ultrasound array element using thermoelastic expansion in an elastomeric film. *Applied Physics Letters*, 79(4) :548–550, 2001.
- [20] D Calvetti, S Morigi, L Reichel, and F Sgallari. Tikhonov regularization and the l-curve for large discrete ill-posed problems. *Journal of computational and applied mathematics*, 123(1) :423–446, 2000.
- [21] Jorge Camacho, Montserrat Parrilla, and Carlos Fritsch. Phase coherence imaging. *IEEE transactions on ultrasonics, ferroelectrics, and frequency control*, 56(5) :958–974, 2009.
- [22] Emmanuel J Candes, Carlos A Sing-Long, and Joshua D Trzasko. Unbiased risk estimates for singular value thresholding and spectral estimators. *IEEE transactions on signal processing*, 61(19) :4643–4657, 2013.
- [23] Lisa Carroll and Tatyana R. Humphreys. Laser-tissue interactions. *Clinics in Dermatology*, 24(1) :2 – 7, 2006.
- [24] David H Chambers and AK Gautesen. Time reversal for a single spherical scatterer. *The Journal of the Acoustical Society of America*, 109(6) :2616–2624, 2001.
- [25] Jiqi Cheng, Jian yu Lu, Wei Lin, and Yi-Xian Qin. A new algorithm for spatial impulse response of rectangular planar transducers. *Ultrasonics*, 51(2) :229 – 237, 2011.
- [26] Jung Woo Choe, Ömer Oralkan, Amin Nikoozadeh, Anshuman Bhuyan, Byung Chul Lee, Mustafa Gence, and Butrus T Khuri-Yakub. Real-time volumetric imaging system for cmut arrays. In *2011 IEEE International Ultrasonics Symposium*, pages 1064–1067. IEEE, 2011.
- [27] Donald B Conkey, Antonio M Caravaca Aguirre, Jake D Dove, Hengyi Ju, Todd W Murray, and Rafael Piestun. Super resolution photoacoustic imaging through a scattering wall. *Nature Communications*, 6, 2015.
- [28] Verya Daeichin, Chao Chen, Qing Ding, Min Wu, Robert Beurskens, Geert Springeling, Emile Noothout, Martin D Verweij, Koen WA van Dongen, Johan G Bosch, et al. A broadband polyvinylidene difluoride-based hydrophone with integrated readout circuit for intravascular photoacoustic imaging. *Ultrasound in medicine & biology*, 42(5) :1239–1243, 2016.
- [29] X. Luís Deán-Ben and Daniel Razansky. Portable spherical array probe for volumetric real-time optoacoustic imaging at centimeter-scale depths. *Opt. Express*, 21(23) :28062–28071, Nov 2013.
- [30] Xosé Luís Deán-Ben and Daniel Razansky. On the link between the speckle free nature of optoacoustics and visibility of structures in limited-view tomography. *Photoacoustics*, 4(4) :133–140, 2016.

- [31] B. Delannoy, H. Lasota, C. Bruneel, R. Torguet, and E. Bridoux. The infinite planar baffles problem in acoustic radiation and its experimental verification. *Journal of Applied Physics*, 50(8), 1979.
- [32] Charlie Demené, Elodie Tiran, Lim-Anna Sieu, Antoine Bergel, Jean Luc Gennisson, Mathieu Pernot, Thomas Deffieux, Ivan Cohen, and Mickael Tanter. 4d microvascular imaging based on ultrafast doppler tomography. *NeuroImage*, 127 :472–483, 2016.
- [33] Jing Deng and Charles H Rodeck. New fetal cardiac imaging techniques. *Prenatal diagnosis*, 24(13) :1092–1103, 2004.
- [34] GJ Diebold and T Sun. Properties of photoacoustic waves in one, two, and three dimensions. *Acta Acustica united with Acustica*, 80(4) :339–351, 1994.
- [35] Christian Dorme and Mathias Fink. Focusing in transmit–receive mode through inhomogeneous media : The time reversal matched filter approach. *The Journal of the Acoustical Society of America*, 98(2) :1155–1162, 1995.
- [36] Gilad Drozdov and Amir Rosenthal. Analysis of negatively focused ultrasound detectors in optoacoustic tomography. *IEEE Transactions on Medical Imaging*, 2016.
- [37] Francis A Duck. *Physical properties of tissues : a comprehensive reference book*. Academic press, 2013.
- [38] Sherif Hamdy El-Gohary, Mohamed Kilany Metwally, Seyoung Eom, Seung Hyun Jeon, Kyung Min Byun, and Tae-Seong Kim. Design study on photoacoustic probe to detect prostate cancer using 3d monte carlo simulation and finite element method. *Biomedical Engineering Letters*, 4(3) :250–257, 2014.
- [39] Arif S Ergun, Goksen G Yaralioglu, and Butrus T Khuri-Yakub. Capacitive micromachined ultrasonic transducers : Theory and technology. *Journal of Aerospace Engineering*, 16(2) :76–84, 2003.
- [40] Sergey A Ermilov, Tuenchit Khamapirad, Andre Conjusteau, Morton H Leonard, Ron Laceywell, Ketan Mehta, Tom Miller, and Alexander A Oraevsky. Laser optoacoustic imaging system for detection of breast cancer. *Journal of biomedical optics*, 14(2) :024007–024007, 2009.
- [41] Younes Farouj, Jean-Marc Freyermuth, Laurent Navarro, Marianne Clausel, and Philippe Delachartre. Hyperbolic wavelet-fisz denoising for a model arising in ultrasound imaging. 2016.
- [42] P. Faure, D. Cathignol, J. Y. Chapelon, and V. L. Newhouse. On the pressure field of a transducer in the form of a curved strip. *The Journal of the Acoustical Society of America*, 95(2), 1994.
- [43] Thomas Felix Fehm, Xosé Luís Deán-Ben, and Daniel Razansky. Four dimensional hybrid ultrasound and optoacoustic imaging via passive element optical excitation in a hand-held probe. *Applied Physics Letters*, 105(17), 2014.
- [44] R.P. Feynman, R.B. Leighton, and M.L. Sands. *The Feynman Lectures on Physics*. Number v. 1 in The Feynman Lectures on Physics. Addison-Wesley, 1963.
- [45] Floyd A Firestone. The supersonic reflectoscope, an instrument for inspecting the interior of solid parts by means of sound waves. *The Journal of the Acoustical Society of America*, 17(3) :287–299, 1946.
- [46] C. H. Frazier and W. D. O’Brien. Synthetic aperture techniques with a virtual source element. *IEEE Transactions on Ultrasonics, Ferroelectrics, and Frequency Control*, 45(1) :196–207, Jan 1998.

- [47] Matthew P. Fronheiser, Sergey A. Ermilov, Hans-Peter Brecht, Andre Conjusteau, Richard Su, Ketan Mehta, and Alexander A. Oraevsky. Real-time optoacoustic monitoring and three-dimensional mapping of a human arm vasculature. *Journal of Biomedical Optics*, 15(2) :021305–021305–7, 2010.
- [48] Amir H Gandjbakhche, Robert F Bonner, Ralph Nossal, and George H Weiss. Effects of multiple-passage probabilities on fluorescent signals from biological media. *Applied optics*, 36(19) :4613–4619, 1997.
- [49] Gene H Golub and Urs Von Matt. Generalized cross-validation for large-scale problems. *Journal of Computational and Graphical Statistics*, 6(1) :1–34, 1997.
- [50] J.W. Goodman. *Introduction to Fourier Optics*. McGraw-Hill, 2nd edition, 1996.
- [51] Zijian Guo, Li Li, and Lihong V Wang. On the speckle-free nature of photoacoustic tomography. *Medical physics*, 36(9) :4084–4088, 2009.
- [52] Vitalii E Gusev and Aleksandr A Karabutov. Laser optoacoustics. *NASA STI/Recon Technical Report A*, 93, 1991.
- [53] Arman Hajati, Dimitre Latev, Deane Gardner, Azadeh Hajati, Darren Imai, Marc Torrey, and Martin Schoeppler. Three-dimensional micro electromechanical system piezoelectric ultrasound transducer. *Applied Physics Letters*, 101(25) :253101, 2012.
- [54] Matthew I Haller and Butrus T Khuri-Yakub. A surface micromachined electrostatic ultrasonic air transducer. *IEEE transactions on ultrasonics, ferroelectrics, and frequency control*, 43(1) :1–6, 1996.
- [55] Martin Hanke and Per Christian Hansen. Regularization methods for large-scale problems. *Surv. Math. Ind*, 3(4) :253–315, 1993.
- [56] Per Christian Hansen. *Rank-deficient and discrete ill-posed problems : numerical aspects of linear inversion*, volume 4. Siam, 1998.
- [57] Per Christian Hansen. Regularization tools version 4.0 for matlab 7.3. *Numerical algorithms*, 46(2) :189–194, 2007.
- [58] Gerald R. Harris. Transient field of a baffled planar piston having an arbitrary vibration amplitude distribution. *The Journal of the Acoustical Society of America*, 70(1), 1981.
- [59] Richard C Haskell, Lars O Svaasand, Tsong-Tseh Tsay, Ti-Chen Feng, Bruce J Tromberg, and Matthew S McAdams. Boundary conditions for the diffusion equation in radiative transfer. *JOSA A*, 11(10) :2727–2741, 1994.
- [60] E. Hecht. *Optics*. Addison-Wesley, 2002.
- [61] Gerrit Held, Stefan Preisser, H. Günhan Akarçay, Sara Peeters, Martin Frenz, and Michael Jaeger. Effect of irradiation distance on image contrast in epi-optoacoustic imaging of human volunteers. *Biomed. Opt. Express*, 5(11) :3765–3780, Nov 2014.
- [62] Christoph GA Hoelen and Frits FM de Mul. Image reconstruction for photoacoustic scanning of tissue structures. *Applied Optics*, 39(31) :5872–5883, 2000.
- [63] KW Hollman, KW Rigby, and M O’Donnell. Coherence factor of speckle from a multi-row probe. In *Ultrasonics Symposium, 1999. Proceedings. 1999 IEEE*, volume 2, pages 1257–1260. IEEE, 1999.
- [64] Sverre Holm, Andreas Austeng, Kamran Iranpour, and J-F Hopperstad. Sparse sampling in array processing. In *Nonuniform Sampling*, pages 787–833. Springer, 2001.

- [65] Eunki Hong, SV Krishnaswamy, CB Freidhoff, and S Trolier-McKinstry. Micromachined piezoelectric diaphragms actuated by ring shaped interdigitated transducer electrodes. *Sensors and Actuators A : Physical*, 119(2) :521–527, 2005.
- [66] John A Hossack and Bertram A Auld. Improving the characteristics of a transducer using multiple piezoelectric layers. *IEEE Transactions on Ultrasonics, Ferroelectrics, and Frequency Control*, 40(2) :131–139, 1993.
- [67] Dehong Hu, Jingnan Zhang, Guanhui Gao, Zonghai Sheng, Haodong Cui, and Lintao Cai. Indocyanine green loaded polydopamine reduced graphene oxide nanocomposites with amplifying photoacoustic and photothermal effects for cancer theranostics. *Theranostics*, 6 :1043–1052, 2016.
- [68] F Hunt. *Electroacoustics : the analysis of transduction, and its historical background*. 1982. New York : Acoustical Society of America.
- [69] Frederick V Hunt. *Electroacoustics : the analysis of transduction, and its historical background*. Number 5. Acoustical Society of America, 1954.
- [70] Steven .L Jacques, Ting Li, and Scott Prahl. Monte carlo simulations of light transport in 3d heterogenous tissues (mcxyz.c). <http://omlc.org/software/mc/mcxyz/index.html>. [accessed 05.12.15].
- [71] Michael Jaeger, Jeffrey C. Bamber, and Martin Frenz. Clutter elimination for deep clinical optoacoustic imaging using localised vibration tagging (lovit). *Photoacoustics*, 1(2) :19 – 29, 2013.
- [72] Krista Jansen, Antonius FW van der Steen, Min Wu, Heleen MM van Beusekom, Geert Springeling, Xiang Li, Qifa Zhou, K. Kirk Shung, Dominique PV de Kleijn, and Gijs van Soest. Spectroscopic intravascular photoacoustic imaging of lipids in atherosclerosis. *Journal of Biomedical Optics*, 19(2) :026006, 2014.
- [73] J. A. Jensen, M. F. Holten-Lund, R. T. Nilsson, M. Hansen, U. D. Larsen, R. P. Domsten, B. G. Tomov, M. B. Stuart, S. I. Nikolov, M. J. Pihl, Y. Du, J. H. Rasmussen, and M. F. Rasmussen. Sarus : A synthetic aperture real-time ultrasound system. *IEEE Transactions on Ultrasonics, Ferroelectrics, and Frequency Control*, 60(9) :1838–1852, Sep 2013.
- [74] Jørgen Arendt Jensen. Field : A program for simulating ultrasound systems. In *10TH NORDIC-BALTIC CONFERENCE ON BIOMEDICAL IMAGING, VOL. 4, SUPPLEMENT 1, PART 1 : 351–353*. Citeseer, 1996.
- [75] Jørgen Arendt Jensen. A new calculation procedure for spatial impulse responses in ultrasound. *The Journal of the Acoustical Society of America*, 105(6), 1999.
- [76] Don H Johnson and Dan E Dudgeon. *Array signal processing : concepts and techniques*. Simon & Schuster, 1992.
- [77] Joontaek Jung, Sangwon Kim, Wonjun Lee, and Hongsoo Choi. Fabrication of a two-dimensional piezoelectric micromachined ultrasonic transducer array using a top-crossover-to-bottom structure and metal bridge connections. *Journal of Micromechanics and Microengineering*, 23(12) :125037, 2013.
- [78] M. A. Kalkhoran, F. Varray, M. Vallet, and D. Vray. Volumetric pulse echo and optoacoustic imaging by elaborating a weighted synthetic aperture technique. In *Ultrasonics Symposium (IUS), 2015 IEEE International*, pages 1–4, Oct 2015.
- [79] M. Karaman, I. O. Wygant, Ö Oralkan, and B. T. Khuri-Yakub. Minimally redundant 2-d array designs for 3-d medical ultrasound imaging. *IEEE Transactions on Medical Imaging*, 28(7) :1051–1061, July 2009.

- [80] Haixin Ke, Todd N Erpelding, Ladislav Jankovic, Changjun Liu, and Lihong V Wang. Performance characterization of an integrated ultrasound, photoacoustic, and thermoacoustic imaging system. *Journal of biomedical optics*, 17(5) :0560101–0560106, 2012.
- [81] Marleen Keijzer, Steven L Jacques, Scott A Prahl, and Ashley J Welch. Light distributions in artery tissue : Monte carlo simulations for finite-diameter laser beams. *Lasers in surgery and medicine*, 9(2) :148–154, 1989.
- [82] L.E. Kinsler. *Fundamentals of acoustics*. Wiley, 2000.
- [83] Roy G. M. Kolkman, Peter J. Brands, Wiendelt Steenbergen, and Ton G. van Leeuwen. Real-time in vivo photoacoustic and ultrasound imaging. *Journal of Biomedical Optics*, 13(5) :050510–050510–3, 2008.
- [84] Sridhar Krishnaswamy. Theory and applications of laser-ultrasonic techniques. *Ultrasonic nondestructive evaluation : Engineering and biological material characterization*, pages 435–494, 2003.
- [85] Robert A Kruger, Cherie M Kuzmiak, Richard B Lam, Daniel R Reinecke, Stephen P Del Rio, and Doreen Steed. Dedicated 3d photoacoustic breast imaging. *Medical physics*, 40(11) :113301, 2013.
- [86] Pieter Kruizinga, Antonius F. W. van der Steen, Nico de Jong, Geert Springeling, Jan Lukas Robertus, Aad van der Lugt, and Gijs van Soest. Photoacoustic imaging of carotid artery atherosclerosis. *Journal of Biomedical Optics*, 19(11) :110504, 2014.
- [87] Patrick D Kumavor, Umar Alqasemi, Behnoosh Tavakoli, Hai Li, Yi Yang, Xiaoguang Sun, Edward Warych, and Quing Zhu. Co-registered pulse-echo/photoacoustic transvaginal probe for real time imaging of ovarian tissue. *Journal of biophotonics*, 6(6-7) :475–484, 2013.
- [88] Minalini Lakshman and Andrew Needles. Screening and quantification of the tumor microenvironment with micro-ultrasound and photoacoustic imaging. *Nat Meth*, 12(4), 2015.
- [89] Alain Lhémery. Impulse response method to predict echo responses from targets of complex geometry. part i : Theory. *The Journal of the Acoustical Society of America*, 90(5) :2799–2807, 1991.
- [90] Changhui Li, Geng Ku, and Lihong V Wang. Negative lens concept for photoacoustic tomography. *Physical Review E*, 78(2) :021901, 2008.
- [91] Meng-Lin Li, Hao F. Zhang, Konstantin Maslov, George Stoica, and Lihong V. Wang. Improved in vivo photoacoustic microscopy based on a virtual-detector concept. *Opt. Lett.*, 31(4) :474–476, Feb 2006.
- [92] Pai-Chi Li and Meng-Lin Li. Adaptive imaging using the generalized coherence factor. *IEEE transactions on ultrasonics, ferroelectrics, and frequency control*, 50(2) :128–141, 2003.
- [93] Shengfu Li, Bruno Montcel, Wanyu Liu, and Didier Vray. Analytical model of optical fluence inside multiple cylindrical inhomogeneities embedded in an otherwise homogeneous turbid medium for quantitative photoacoustic imaging. *Optics express*, 22(17) :20500–20514, 2014.
- [94] Shengfu Li, Bruno Montcel, Zhen Yuan, Wanyu Liu, and Didier Vray. Multigrid-based reconstruction algorithm for quantitative photoacoustic tomography. *Biomedical optics express*, 6(7) :2424–2434, 2015.
- [95] Der-Song Lin, Xuefeng Zhuang, Serena H Wong, Mario Kupnik, and Butrus Thomas Khuri-Yakub. Encapsulation of capacitive micromachined ultrasonic transducers using viscoelastic polymer. *Journal of Microelectromechanical Systems*, 19(6) :1341–1351, 2010.

- [96] Fredrik Lingvall and Tomas Olofsson. On time-domain model-based ultrasonic array imaging. *IEEE transactions on ultrasonics, ferroelectrics, and frequency control*, 54(8) :1623–1633, 2007.
- [97] Fredrik Lingvall, Tomas Olofsson, and Tadeusz Stepinski. Synthetic aperture imaging using sources with finite aperture : Deconvolution of the spatial impulse response. *The Journal of the Acoustical Society of America*, 114(1) :225–234, 2003.
- [98] G. R. Lockwood, Pai-Chi Li, M. O’Donnell, and F. S. Foster. Optimizing the radiation pattern of sparse periodic linear arrays. *IEEE Transactions on Ultrasonics, Ferroelectrics, and Frequency Control*, 43(1) :7–14, Jan 1996.
- [99] J. C. Lockwood and J. G. Willette. High speed method for computing the exact solution for the pressure variations in the nearfield of a baffled piston. *The Journal of the Acoustical Society of America*, 53(3), 1973.
- [100] J.D. Logan. *Applied Mathematics*. Wiley, 2013.
- [101] Raoul Mallart and Mathias Fink. The van cittert–zernike theorem in pulse echo measurements. *The Journal of the Acoustical Society of America*, 90(5) :2718–2727, 1991.
- [102] Oscar Martínez-Graullera, Carlos J Martín, Gregorio Godoy, and Luis G Ullate. 2d array design based on fermat spiral for ultrasound imaging. *Ultrasonics*, 50(2) :280–289, 2010.
- [103] Robert J. McGough. Rapid calculations of time-harmonic nearfield pressures produced by rectangular pistons. *The Journal of the Acoustical Society of America*, 115(5), 2004.
- [104] Robert J. McGough, Thaddeus V. Samulski, and James F. Kelly. An efficient grid sectoring method for calculations of the near-field pressure generated by a circular piston. *The Journal of the Acoustical Society of America*, 115(5), 2004.
- [105] P. Mohajerani, S. Tzoumas, A. Rosenthal, and V. Ntziachristos. Optical and optoacoustic model-based tomography : Theory and current challenges for deep tissue imaging of optical contrast. *IEEE Signal Processing Magazine*, 32(1) :88–100, Jan 2015.
- [106] J-P Monchalin. Optical detection of ultrasound. *IEEE Transactions on Ultrasonics Ferroelectrics and Frequency Control*, 33 :485–499, 1986.
- [107] G. Montaldo, M. Tanter, J. Bercoff, N. Benech, and M. Fink. Coherent plane-wave compounding for very high frame rate ultrasonography and transient elastography. *IEEE Transactions on Ultrasonics, Ferroelectrics, and Frequency Control*, 56(3) :489–506, March 2009.
- [108] P.M.C. Morse and H. Feshbach. *Methods of theoretical physics*. Number vol. 2 in International series in pure and applied physics. McGraw-Hill, 1953.
- [109] P.M.C. Morse and K.U. Ingard. *Theoretical Acoustics*. International series in pure and applied physics. Princeton University Press, 1968.
- [110] SY Nam, LM Ricles, LJ Suggs, and SY Emelianov. In vivo ultrasound and photoacoustic monitoring of mesenchymal stem cells labeled with gold nanotracers. *PLoS ONE*, 7(5), 2012.
- [111] J. J. Niederhauser, M. Jaeger, R. Lemor, P. Weber, and M. Frenz. Combined ultrasound and optoacoustic system for real-time high-contrast vascular imaging in vivo. *IEEE Transactions on Medical Imaging*, 24(4) :436–440, April 2005.
- [112] Carl-Inge Colombo Nilsen and Sverre Holm. Wiener beamforming and the coherence factor in ultrasound imaging. *IEEE transactions on ultrasonics, ferroelectrics, and frequency control*, 57(6) :1329–1346, 2010.

- [113] Stephen J Norton. Synthetic aperture imaging with arrays of arbitrary shape. ii. the annular array. *IEEE transactions on ultrasonics, ferroelectrics, and frequency control*, 49(4) :404–408, 2002.
- [114] Vasilis Ntziachristos. Going deeper than microscopy : the optical imaging frontier in biology. *Nature methods*, 7(8) :603–614, 2010.
- [115] Matthew O’Donnell, ET Jaynes, and JG Miller. Kramers–kronig relationship between ultrasonic attenuation and phase velocity. *The Journal of the Acoustical Society of America*, 69(3) :696–701, 1981.
- [116] Alexander A Oraevsky, Steven L Jacques, and Frank K Tittel. Measurement of tissue optical properties by time-resolved detection of laser-induced transient stress. *Applied Optics*, 36(1) :402–415, 1997.
- [117] G Paltauf, R Nuster, and P Burgholzer. Weight factors for limited angle photoacoustic tomography. *Physics in Medicine and Biology*, 54(11) :3303, 2009.
- [118] Guenther Paltauf, Robert Nuster, Markus Haltmeier, and Peter Burgholzer. Photoacoustic tomography using a mach-zehnder interferometer as an acoustic line detector. *Applied optics*, 46(16) :3352–3358, 2007.
- [119] Guenther Paltauf, JA Viator, SA Prahl, and SL Jacques. Iterative reconstruction algorithm for optoacoustic imaging. *The Journal of the Acoustical Society of America*, 112(4) :1536–1544, 2002.
- [120] Athanasios Papoulis and S Unnikrishna Pillai. *Probability, random variables, and stochastic processes*. Tata McGraw-Hill Education, 2002.
- [121] Michael S Patterson, Britton Chance, and Brian C Wilson. Time resolved reflectance and transmittance for the noninvasive measurement of tissue optical properties. *Applied optics*, 28(12) :2331–2336, 1989.
- [122] Keith S Peat and Ray Kirby. Acoustic wave motion along a narrow cylindrical duct in the presence of an axial mean flow and temperature gradient. *The Journal of the Acoustical Society of America*, 107(4) :1859–1867, 2000.
- [123] B. Piwakowski and B. Delannoy. Method for computing spatial pulse response : Time domain approach. *The Journal of the Acoustical Society of America*, 86(6) :2422–2432, 1989.
- [124] B. Piwakowski and K. Sbai. A new approach to calculate the field radiated from arbitrarily structured transducer arrays. *IEEE Transactions on Ultrasonics, Ferroelectrics, and Frequency Control*, 46(2) :422–440, March 1999.
- [125] Claire Prada, Sébastien Manneville, Dimitri Spoliansky, and Mathias Fink. Decomposition of the time reversal operator : Detection and selective focusing on two scatterers. *The Journal of the Acoustical Society of America*, 99(4), 1996.
- [126] Manojit Pramanik, Geng Ku, and Lihong V Wang. Tangential resolution improvement in thermoacoustic and photoacoustic tomography using a negative acoustic lens. *Journal of biomedical optics*, 14(2) :024028–024028, 2009.
- [127] Stefan Preisser, Nigel L. Bush, Andreas G. Gertsch-Grover, Sara Peeters, Arthur E. Bailey, Jeffrey C. Bamber, Martin Frenz, and Michael Jaeger. Vessel orientation-dependent sensitivity of optoacoustic imaging using a linear array transducer. *Journal of Biomedical Optics*, 18(2) :026011–026011, 2013.
- [128] Stefan Preisser, Gerrit Held, Hidayet G Akarçay, Michael Jaeger, and Martin Frenz. Study of clutter origin in in-vivo epi-optoacoustic imaging of human forearms. *Journal of Optics*, 18(9) :094003, 2016.



- [129] Jean Provost and Frédéric Lesage. The application of compressed sensing for photo-acoustic tomography. *IEEE transactions on medical imaging*, 28(4) :585–594, 2009.
- [130] Jinyi Qi and R. H. Huesman. Wavelet crosstalk matrix and its application to assessment of shift-variant imaging systems. *IEEE Transactions on Nuclear Science*, 51(1) :123–129, Feb 2004.
- [131] Alessandro Ramalli, Enrico Boni, Alessandro Stuart Savoia, and Piero Tortoli. Density-tapered spiral arrays for ultrasound 3-d imaging. *IEEE transactions on ultrasonics, ferroelectrics, and frequency control*, 62(8) :1580–1588, 2015.
- [132] J.W.S.B. Rayleigh and R.B. Lindsay. *The Theory of Sound*. Number vol. 2 in Dover Books on Physics. Dover, 1945.
- [133] Brandon Redding and Hui Cao. Using a multimode fiber as a high-resolution, low-loss spectrometer. *Optics letters*, 37(16) :3384–3386, 2012.
- [134] Aarnoud Laurens Roest, Klaus Reimann, Mareike Klee, Jozef Thomas Martinus Van Beek, and John Douglas Fraser. Cmut with a high-k dielectric, June 19 2012. US Patent 8,203,912.
- [135] Thomas M Rossi and Isiah M Warner. Rank estimation of emission excitation matrixes using frequency analysis of eigenvectors. *Analytical chemistry*, 58(4) :810–815, 1986.
- [136] Michael Roumeliotis, Robert Z Stodilka, Mark A Anastasio, Govind Chaudhary, Hazem Al-Aabed, Eldon Ng, Andrea Immucci, and Jeffrey JL Carson. Analysis of a photoacoustic imaging system by the crosstalk matrix and singular value decomposition. *Optics express*, 18(11) :11406–11417, 2010.
- [137] Emmanuel Roux, Alessandro Ramalli, Piero Tortoli, Christian Cachard, Marc C Robini, and Hervé Liebgott. 2-d ultrasound sparse arrays multidepth radiation optimization using simulated annealing and spiral-array inspired energy functions. *IEEE Transactions on Ultrasonics, Ferroelectrics, and Frequency Control*, 63(12) :2138–2149, 2016.
- [138] Jose Luis San Emeterio and Luis G. Ullate. Diffraction impulse response of rectangular transducers. *The Journal of the Acoustical Society of America*, 92(2), 1992.
- [139] M Sautto, D Leone, Alessandro Savoia, D Ghisu, Fabio Quaglia, Giosuè Caliano, and Andrea Mazzanti. A cmut transceiver front-end with 100-v tx driver and 1-mw low-noise capacitive feedback rx amplifier in bcd-soi technology. In *European Solid State Circuits Conference (ESSCIRC), ESSCIRC 2014-40th*, pages 407–410. IEEE, 2014.
- [140] Mark E. Schafer and Peter A. Lewin. Transducer characterization using the angular spectrum method. *The Journal of the Acoustical Society of America*, 85(5), 1989.
- [141] Hans-Martin Schwab, Martin F. Beckmann, and Georg Schmitz. Photoacoustic clutter reduction by inversion of a linear scatter model using plane wave ultrasound measurements. *Biomed. Opt. Express*, 7(4) :1468–1478, Apr 2016.
- [142] K Kirk Shung and Gary A Thieme. *Ultrasonic scattering in biological tissues*. CRC Press, 1992.
- [143] Eugen Skudrzyk. *The foundations of acoustics : basic mathematics and basic acoustics*. Springer Science & Business Media, 2012.
- [144] Stephen W Smith, Henry G Pavy, and Olaf T von Ramm. High-speed ultrasound volumetric imaging system. i. transducer design and beam steering. *IEEE transactions on ultrasonics, ferroelectrics, and frequency control*, 38(2) :100–108, 1991.

- [145] P. Stepanishen, M. Forbes, and S. Letcher. The relationship between the impulse response and angular spectrum methods to evaluate acoustic transient fields. *The Journal of the Acoustical Society of America*, 90(5), 1991.
- [146] Peter R. Stepanishen. Transient radiation from pistons in an infinite planar baffle. *The Journal of the Acoustical Society of America*, 49(5B), 1971.
- [147] Peter R. Stepanishen and Kim C. Benjamin. Forward and backward projection of acoustic fields using fft methods. *The Journal of the Acoustical Society of America*, 71(4), 1982.
- [148] Yao Sun, Eric Sobel, and Huabei Jiang. Quantitative three-dimensional photoacoustic tomography of the finger joints : an in vivo study. *Journal of biomedical optics*, 14(6) :064002–064002, 2009.
- [149] Michael Tanter, J-F Aubry, J Gerber, J-L Thomas, and M Fink. Optimal focusing by spatio-temporal inverse filter. i. basic principles. *The Journal of the Acoustical Society of America*, 110(1) :37–47, 2001.
- [150] Sergey Telenkov, Andreas Mandelis, Bahman Lashkari, and Michael Forcht. Frequency-domain photothermoacoustics : Alternative imaging modality of biological tissues. *Journal of Applied Physics*, 105(10) :102029, 2009.
- [151] JF. Theumann, M. Arditi, JJ. Meister, and E. Jaques. Acoustic fields of concave cylindrical transducers. *The Journal of the Acoustical Society of America*, 88(2), 1990.
- [152] Johan M Thijssen. Ultrasonic speckle formation, analysis and processing applied to tissue characterization. *Pattern Recognition Letters*, 24(4) :659–675, 2003.
- [153] C Thomsen, Holger T Grahn, Humphrey J Maris, and Jan Tauc. Surface generation and detection of phonons by picosecond light pulses. *Physical Review B*, 34(6) :4129, 1986.
- [154] Piero Tortoli, Luca Bassi, Enrico Boni, Alessandro Dallai, Francesco Guidi, and Stefano Ricci. Ula-op : An advanced open platform for ultrasound research. *IEEE transactions on ultrasonics, ferroelectrics, and frequency control*, 56(10) :2207–2216, 2009.
- [155] Bradley E. Treeby and B. T. Cox. k-wave : Matlab toolbox for the simulation and reconstruction of photoacoustic wave fields. *Journal of Biomedical Optics*, 15(2) :021314–021314–12, 2010.
- [156] G. E. Tupholme. Generation of acoustic pulses by baffled plane pistons. *Mathematika*, 16 :209–224, 12 1969.
- [157] Jake Turner, Héctor Estrada, Moritz Kneipp, and Daniel Razansky. Improved optoacoustic microscopy through three-dimensional spatial impulse response synthetic aperture focusing technique. *Opt. Lett.*, 39(12) :3390–3393, Jun 2014.
- [158] L. G. Ullate and J. L. San Emeterio. A new algorithm to calculate the transient near-field of ultrasonic phased arrays. *IEEE Transactions on Ultrasonics, Ferroelectrics, and Frequency Control*, 39(6) :745–753, Nov 1992.
- [159] Dominique Van de Sompel, Laura S Sasportas, Jesse V Jokerst, and Sanjiv S Gambhir. Comparison of deconvolution filters for photoacoustic tomography. *PloS one*, 11(3) :e0152597, 2016.
- [160] M. Vogt, J. Opretzka, and H. Ermert. Synthetic aperture focusing technique for high-resolution imaging of surface structures with high-frequency ultrasound. In *2009 IEEE International Ultrasonics Symposium*, pages 1514–1517, Sept 2009.

- [161] Kun Wang, Sergey A Ermilov, Richard Su, Hans-Peter Brecht, Alexander A Oraevsky, and Mark A Anastasio. An imaging model incorporating ultrasonic transducer properties for three-dimensional optoacoustic tomography. *IEEE transactions on medical imaging*, 30(2) :203–214, 2011.
- [162] LH Wang and Steven L Jacques. Monte carlo modeling of light transport in multi-layered tissues in standard c. *The University of Texas, MD Anderson Cancer Center, Houston*, 1992.
- [163] Lihong V Wang. Tutorial on photoacoustic microscopy and computed tomography. *IEEE Journal of Selected Topics in Quantum Electronics*, 14(1) :171–179, 2008.
- [164] Lihong V Wang. Multiscale photoacoustic microscopy and computed tomography. *Nature photonics*, 3(9) :503–509, 2009.
- [165] Lihong V Wang and Hsin-i Wu. *Biomedical optics : principles and imaging*. John Wiley & Sons, 2012.
- [166] L.V. Wang. *Photoacoustic Imaging and Spectroscopy*. Optical Science and Engineering. CRC Press, 2009.
- [167] Yu Wang, Todd N. Erpelding, Ladislav Jankovic, Zijian Guo, Jean-Luc Robert, Guillaume David, and Lihong V. Wang. In vivo three-dimensional photoacoustic imaging based on a clinical matrix array ultrasound probe. *Journal of Biomedical Optics*, 17(6) :061208–1–061208–5, 2012.
- [168] Peter NT Wells. Ultrasonic imaging of the human body. *Reports on progress in physics*, 62(5) :671, 1999.
- [169] Hermann Weyl. Ausbreitung elektromagnetischer wellen über einem ebenen leiter. *Annalen der Physik*, 365(21) :481–500, 1919.
- [170] Cort J Willmott and Kenji Matsuura. Advantages of the mean absolute error (mae) over the root mean square error (rmse) in assessing average model performance. *Climate research*, 30(1) :79–82, 2005.
- [171] Philip Wong, Ivan Kosik, Avery Raess, and Jeffrey JL Carson. Objective assessment and design improvement of a staring, sparse transducer array by the spatial crosstalk matrix for 3d photoacoustic tomography. *PloS one*, 10(4) :e0124759, 2015.
- [172] Robert Williams Wood and Alfred L Loomis. Xxxviii. the physical and biological effects of high-frequency sound-waves of great intensity. *The London, Edinburgh, and Dublin philosophical magazine and journal of science*, 4(22) :417–436, 1927.
- [173] B Woodward, SK Hole, and W Forsythe. Transducer design for a correlation log. *Ultrasonics*, 31(1) :21–34, 1993.
- [174] Zhixing Xiea, Won-Mean Leea, Fong Ming Hooia, J Brian Fowlkesa, Renee W Pinskya, Dean Muellerb, Xueding Wanga, and Paul L Carson. Combined photoacoustic and ultrasound imaging of human breast in vivo in the mammographic geometry. In *Proc. of SPIE Vol*, volume 8581, pages 85813D–1, 2013.
- [175] Minghua Xu and Lihong V Wang. Universal back-projection algorithm for photoacoustic computed tomography. *Physical Review E*, 71(1) :016706, 2005.
- [176] Minghua Xu and Lihong V. Wang. Photoacoustic imaging in biomedicine. *Review of Scientific Instruments*, 77(4), 2006.
- [177] Yuan Xu, Lihong V Wang, Gaik Ambartsoumian, and Peter Kuchment. Reconstructions in limited-view thermoacoustic tomography. *Medical physics*, 31(4) :724–733, 2004.

- [178] Junjie Yao and Lihong V Wang. Sensitivity of photoacoustic microscopy. *Photoacoustics*, 2(2) :87–101, 2014.
- [179] J. T. Yen, J. P. Steinberg, and S. W. Smith. Sparse 2-d array design for real time rectilinear volumetric imaging. *IEEE Transactions on Ultrasonics, Ferroelectrics, and Frequency Control*, 47(1) :93–110, Jan 2000.
- [180] C. I. Zanelli, C. W. Hennige, and N. T. Sanghvi. Design and characterization of a 10 cm annular array transducer for high intensity focused ultrasound (hifu) applications. In *Ultrasonics Symposium, 1994. Proceedings., 1994 IEEE*, volume 3, pages 1887–1890 vol.3, Oct 1994.
- [181] R. J. Zemp, C. K. Abbey, and M. F. Insana. Linear system models for ultrasonic imaging : application to signal statistics. *IEEE Transactions on Ultrasonics, Ferroelectrics, and Frequency Control*, 50(6) :642–654, June 2003.
- [182] Roger J. Zemp, Liang Song, Rachel Bitton, K. Kirk Shung, and Lihong V. Wang. Realtime photoacoustic microscopy in vivo with a 30-mhz ultrasound array transducer. *Opt. Express*, 16(11) :7915–7928, May 2008.
- [183] Min Zhou, Geng Ku, Laura Pagon, and Chun Li. Theranostic probe for simultaneous in vivo photoacoustic imaging and confined photothermolysis by pulsed laser at 1064 nm in 4t1 breast cancer model. *Nanoscale*, 6 :15228–15235, 2014.





FOLIO ADMINISTRATIF

THÈSE DE L'UNIVERSITE DE LYON OPEREE AU SEIN DE L'INSA LYON

NOM : M. Azizian Kalkhoran

DATE de SOUTENANCE : 05/04/2017

Prénoms : Mohammad

TITRE : Conception et développement d'une sonde portable universelle pour l'imagerie 3D optoacoustique-ultrasonique

NATURE : Doctorat

Numéro d'ordre : 2017LYSEi027

Spécialité : Acoustique

RESUME : La présente dissertation est principalement consacrée à la conception et à la caractérisation d'une sonde universelle pour l'imagerie volumétrique ultrasons-optoacoustique et le développement d'un algorithme de reconstruction adapté aux exigences physiques pour la conception du système. Les traits distinctifs de cette dissertation sont l'introduction d'une nouvelle géométrie pour les sondes manuelles ultrasons-optoacoustique et des évaluations systématiques basées sur des méthodes de pré-reconstruction et post-reconstruction. Pour éviter l'interprétation biaisée, une évaluation capable d'évaluer le potentiel de la sonde doit être faite. Les caractéristiques mentionnées établissent un cadre pour l'évaluation des performances du système d'imagerie d'une manière précise. En outre, elle permet d'optimiser les performances suivant l'objectif fixé. Ainsi, deux algorithmes de reconstruction anticipée ont été élaborés pour la conception du système OPUS (optoacoustique ultrasons) capables de produire des images avec un contraste et une résolution homogènes sur tout le volume d'intérêt. L'intérêt d'avoir de tels algorithmes est principalement dû au fait que l'analyse des données médicales est souvent faite dans des conditions difficiles, car on est face au bruit, au faible contraste, aux projections limités et à des transformations indésirables opérées par les systèmes d'acquisition. Cette thèse montre, aussi, comment les artefacts de reconstruction peuvent être réduits en compensant les propriétés d'ouverture et en atténuant les artefacts dus à l'échantillonnage angulaire parcimonieux. Afin de transférer cette méthodologie à la clinique et de valider les résultats théoriques, une plate-forme d'imagerie expérimentale a été développée. En utilisant le système de mesure développé, l'évolution d'une nouvelle géométrie annulaire parcimonieuse et sa dynamique ont été étudiées et une preuve de concept a été démontrée à travers des mesures expérimentales dans le but d'évaluer les progrès réalisés.

Mots clés : Imagerie optoacoustique, échographie, capteurs 2D parcimonieux, synthèse d'ouverture focalisée, imagerie volumétrique, bimodalité, reconstruction 3D.

Laboratoire (s) de recherche : Centre de Recherche en Acquisition et Traitement de l'Image pour la Santé

Directeur de thèse : Didier Vray

Président de jury :

Composition du jury :

Anabela Da Silva, **Rapporteur**

Georg Schmitz, **Rapporteur**

Sylvain Gigan, **Examineur**

Alessandro Stuart Savoia, **Examineur**

François Varray, **Examineur**

Didier Vray, **Directeur de thèse**